SPUTTERING BY MULTIPLY-CHARGED IONS, AND PREFERENTIAL SPUTTERING OF ISOTOPIC MIXTURES

Thesis by

Duncan Lee Weathers

In Partial Fulfillment of the Requirements

for the Degree of

Doctor of Philosophy

California Institute of Technology

Pasadena, California

1989

(Submitted March 20, 1989)

Acknowledgments

Many people have contributed both directly and indirectly to the work discussed in this dissertation. I thank my advisor, Professor T. A. Tombrello, for his support, encouragement, and guidance, without which none of this would have been possible. Bob Stokstad, Mike Prior, Bob Tribble, and the staff at Lawrence Berkeley Laboratory's 88-Inch Cyclotron facility are to be recognized for their important roles in the multiply-charged-ion investigation. Hubert Gnaser and Ian Hutcheon played crucial parts in the isotope experiments. Thanks are also due to Steve Spicklemire for his considerable assistance with the same, and to Professor G. J. Wasserburg for making the PANURGE ion probe available for the isotope analysis. Mari and Bob Weller and their students at Yale did much of the work on the sticking probability measurements that are discussed in Appendix A.

Others to whom I am indebted for all that they have taught me in the course of preparing for and carrying out these experiments include Alan Rice, whose advice and friendship I value very highly; Richard Borup and Steve Stryker, for their tutelage in the art and craft of making things; Dr. C. R. Shi, for his assistance with modifications to the keV accelerator used in the isotope experiments; and Marcus Mendenhall.

I thank Michelle Vine for her assistance with secretarial tasks and travel arrangements. The National Science Foundation and IBM are to be recognized for providing financial support for this work.

All of the members of and visitors to the Basic Applied Physics Group, including many whom I have not named, have in some way contributed to my experience here at Caltech, and I acknowledge their influence in shaping me both as a scientist and as a person.

I thank my family for providing the environment that allowed me to follow this path, and for encouraging me along the way. I wish that my father were here to share in this moment; he would no doubt have been pleased by the course I have

chosen. *Finally, I dedicate* this thesis to my wife, Susan, whose love, support, and companionship have made the burden of graduate study infinitely easier to bear.

Abstract

Collector-type experiments have been conducted to investigate two different aspects of sputtering induced by keV ions. The first study looked for possible ejection mechanisms related to the primary charge state of the projectile. Targets of CsI and $LiNbO_3$ were bombarded with 48 keV Ar^{q+}, and a Au target was bombarded with 60 keV Ar^{q+}, for $q = 4$, 8, and 11. The collectors were analyzed using heavy-ion Rutherford backscattering spectroscopy to determine the differential angular sputtering yields; these and the corresponding total yields were examined for variations as a function of projectile charge state. For the Au target, no significant changes were seen, but for the insulating targets slight ($\sim$10%) enhancements were observed in the total yields as the projectile charge state was increased from 4+ to 11+.

In the second investigation, artificial $^{92}Mo/^{100}Mo$ targets were bombarded with 5 and 10 keV beams of Ar^+ and Xe^+ to study the isotopic fractionation of sputtered neutrals as a function of emission angle and projectile fluence. Using secondary ion mass spectroscopy to measure the isotope ratio on the collectors, material ejected into normal directions at low bombarding fluences ($\sim 10^{15}$ ions cm^{-2}) was found to be enriched in the light isotope by as much as $\sim$70‰ compared to steady state. Similar results were found for secondary Mo ions sputtered by 14.5 keV O^-. For low-fluence 5 keV Xe^+ bombardment, the light-isotope enrichment at oblique angles was $\sim$20‰ less than the corresponding enrichment in the normal direction. No angular dependence could be resolved for 5 keV Ar^+ projectiles at the lowest fluence. The above fractionation decreased to steady-state values after bombarding fluences of a few times 10^{16} ions cm^{-2}, with the angular dependence becoming more pronounced. The fractionation and total sputtering yield were found to be strongly correlated, indicating that the above effects may have been related to the presence of a modified target surface layer. The observed effects are consistent with other secondary ion measurements and multiple-interaction computer simulations, and are considerably larger than predicted by existing analytic theory.

Table of Contents

List of Figures

List of Tables

Acronyms

ECR	electron cyclotron resonance
HIRBS	heavy-ion Rutherford backscattering spectroscopy
MCI	multiply-charged ion
RF	radio-frequency
SIMS	secondary ion mass spectroscopy
SNMS	secondary neutral mass spectroscopy
UHV	ultra-high vacuum

Chapter 1

Introduction

1.1 Sputtering by Ion Bombardment

When an energetic particle collides with the surface of a solid, some atoms of the solid may subsequently acquire sufficient energy and momentum to leave the surface; these ejected particles, which may be neutral atoms, ions, molecules, or clusters of atoms, are said to have been sputtered. The particle that induces the sputtering may itself be a neutral or ionized atom or molecule, a neutron, or, in special cases, an electron or photon. In most instances, however, the sputtering projectile is an ion. This is true for the experiments described in this dissertation, and will be assumed in what follows.

First observed more than a century ago [1], sputtering was long considered to be little more than a nuisance in the laboratory because of its association with detrimental effects such as plasma contamination and the erosion of cathodes and apertures in vacuum devices. There are still many situations in which the occurrence of this phenomenon is undesirable, but in recent years sputtering has also been utilized constructively in a growing number of scientific and technological applications. Sputtering is employed in processes such as thin-film deposition in the fabrication of electronic devices [2], and in the milling of submicron-sized features in surfaces [See, *e.g.*, Ref. 3]. The phenomenon is intrinsic to the operation of such devices as sputter ion vacuum pumps [4], and sputter ion sources for particle accelerators [5]. In many ultra-high vacuum (UHV) surface studies, sputter-cleaning is the principal method used to produce atomically clean surfaces. Furthermore, sputtering provides the basis for several analytic spectroscopic techniques, among them secondary ion mass spectroscopy (SIMS), secondary neutral mass spectroscopy (SNMS), and depth profiling with Auger electron spectroscopy (AES) [6].

Sputtering is not restricted exclusively to the confines of the laboratory, of course; this phenomenon also occurs in nature wherever surfaces are exposed to fluxes of energetic ions. In our solar system, sputtering induced by magnetospheric ions and the solar wind has compositionally altered the outermost surface layers of the planetary satellites, as well as the atmospheres of several of the planets [7]. The same process is responsible for introducing much of the mass into planetary magnetospheres [8]. There is also a growing awareness that relatively low-energy physiochemical processes such as sputtering may have contributed to the isotopic anomalies observed in various meteoritic samples [9]; these anomalies have hitherto been ascribed entirely to nucleosynthetic processes [10].

To help characterize the sputtering process, it is useful to define a sputtering yield, Y, as the average number of atoms ejected per incident ion. In general, Y will depend upon many factors, including the magnitude of the projectile's kinetic energy, its mass, direction of incidence, and degree of ionization; and characteristics of the solid such as composition, electronic properties, and structure. Different components of the sputtered flux may be represented by partial sputtering yields Y_i such that $\sum_i Y_i = Y$. The distribution of sputtered particles with respect to emitted energy, E, and direction of emission, $\mathbf{\Omega}$, are described by the differential sputtering yields

$$\frac{\partial Y}{\partial E} \quad \text{and} \quad \frac{\partial Y}{\partial \Omega},$$

respectively. All of these quantities can in principle be measured directly.

Because it is a directly observable phenomenon, sputtering is a useful tool for studying other physical processes. While specifically a surface phenomenon, sputtering is a manifestation of processes occurring in the bulk of a solid during ion bombardment. Hence, sputtering can serve as a probe into aspects of the broader field of collisional phenomena in solids, for which direct experimental observation is often not possible. Measurements of sputtering yields may reveal information about scattering cross sections, stopping powers, and radiation damage processes such as defect production or track formation [11,12].

In view of the nearly ubiquitous occurrence of sputtering wherever energetic ions encounter solid surfaces, whether it be on the lunar surface, in the target chamber of a particle accelerator, or at the wall of a plasma confinement vessel, knowledge of the sputtering process is clearly desirable, in order to be able to understand fully its consequences in nature, and suitably to optimize, minimize, or interpret its effects in the laboratory as the situation demands. For these reasons and because of the connection to collisional processes in general, sputtering has been and continues to be an intensively studied phenomenon.

1.2 Physical Mechanisms Underlying Sputtering

In order to understand how sputtering usually occurs, it is necessary to understand how an energetic ion loses energy as it travels through matter. When such a projectile penetrates into a solid, it will undergo collisions with nuclei and electrons along its path, thus transferring energy to constituents of the solid. Both the strength and frequency of these interactions will be determined largely by the ion's velocity: at velocities from a few eV/amu to a few tens of keV/amu, the projectile's primary means of energy loss will be through screened-Coulomb collisions with nuclei, especially for a heavy projectile. At higher velocities—particularly in the range of a few hundred keV/amu to a few MeV/amu—the predominant interactions will be between the ion and electrons in the solid.

In the context of these two types of collisions and their distinct ranges of dominance, one speaks of a nuclear stopping regime and an electronic stopping regime, as illustrated in Figure 1.1. In the nuclear stopping regime, the direct transfer of kinetic energy from the projectile to target nuclei results in considerable atomic motion and displacement. In effect, a 'collision cascade' is generated, in which target atoms recoiling energetically from the incident ion set other target atoms in motion, until recoiling atoms at the end of the cascade no longer have sufficient energy to cause further displacement. This process is governed mainly by the scattering cross sections of the projectile and participating target atoms. It depends only weakly on collective properties of the solid, and hence occurs to some extent in all materials.

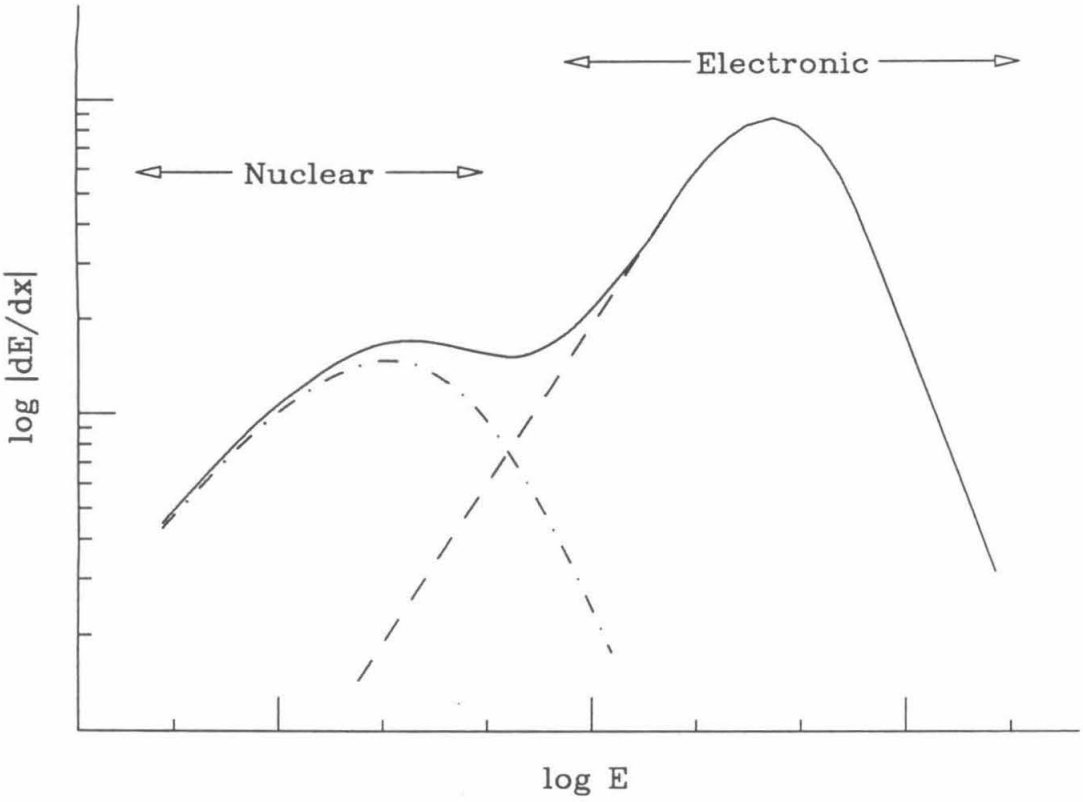

Figure 1.1 Schematic plot of stopping power (rate of energy loss per unit path length) versus energy for a nonrelativistic ion in a solid. The components of the stopping power due to nuclear collisions (– · –) [13] and electronic collisions (– –) [14,15] are indicated, as well as their respective ranges of dominance. The maximum in the electronic stopping power occurs at a velocity $v \sim Z_1^{2/3} e^2/\hbar$, where Z_1 is the atomic number of the ion and e is the magnitude of the electronic charge.

In the electronic stopping regime, however, very little of the projectile's kinetic energy is transferred directly to target nuclei; instead, it is dissipated primarily in the production of ionized and excited electronic states in the solid. The relaxation of these ionized and excited states can result in atomic displacement, but only if other, faster deexcitation mechanisms are unavailable, a condition that is critically dependent upon collective—especially electronic—properties of the solid. Because of this, ion collisions in the electronic stopping regime will produce significant atomic motion only in certain materials; whereas collisions in the nuclear stopping regime

universally produce atomic motion.

For sputtering to occur, atoms near the surface of a solid must be set into motion by an impinging projectile. Thus, an ion initially in the nuclear stopping regime when it collides with a surface will generally induce sputtering. Such sputtering has been termed *collisional*, and usually exhibits yields proportional to the nuclear component of the projectile's specific energy loss, $(dE/dx)|_n$. Typical maximum yields for all but the lightest ions are in the range of one to ten atoms per ion [16]. In contrast with this, an ion in the electronic stopping regime when traversing the near-surface region of a solid can induce significant sputtering only if the displacement-producing electronic relaxation mechanisms alluded to above are operating. Such electronically-mediated sputtering has been observed in a variety of dielectric materials, with yields that tend to depend upon the electronic component of the projectile's energy loss, $(dE/dx)|_e$ [17,18]. These yields may be comparable in magnitude to, and in some cases are much larger than, the collisional yields observed at lower energies. Any sputtering process that involves the transfer of electronic excitational energy to nuclei is referred to as *electronic* sputtering. In the context of sputtering induced by ion bombardment, almost all such processes have been observed in the electronic stopping regime.

Collisional sputtering processes are conventionally grouped into three subcategories. Very light ions and ions with energies close the sputtering threshold (the energy below which no sputtering will occur, typically between a few and a few tens of eV) will not set many atoms into motion when they strike a surface. Such sputtering events with poorly developed collision cascades fall into the single-knockon regime. At the other extreme, very massive, energetic projectiles will cause a great deal of atomic motion upon colliding with a solid. The density of moving atoms can be so high that the majority of atoms in the volume surrounding the ion's track will be in motion. A very dense collision cascade such as this is referred to as a spike, and the resulting sputtering is sometimes treated in the context of a thermal model [19] in which the effective local temperature of the spike determines the yield of ejected particles. In between this spike regime and the single-knockon regime

is the linear cascade regime, in which a large number of atoms participate in each collision cascade; but not so many that an atom, once set in motion, is likely to encounter anything but stationary atoms in subsequent collisions.

Part of this work examines an aspect of collisional sputtering in the linear cascade regime, for which theoretical treatments have been fairly successful. The most sophisticated analytic approach to modeling the sputtering process in this regime [20] assumes that interactions between atoms participating in the collision cascade are binary and uncorrelated, so that a classical Boltzmann transport equation can be used to describe the cascade's development. Furthermore, the low density of moving atoms in the cascade volume allows this Boltzmann equation to be linearized (hence the name 'linear cascade regime'). The velocity distribution of atoms participating in the cascade will be dominated by the large number of low-energy atoms set in motion towards the end of the cascade; an important consequence of this and the assumption of uncorrelated collisions is that the projectile's initial direction of motion becomes unimportant and the velocity distribution may be treated as isotropic, allowing further simplification of the transport equation. The first-order asymptotic solution to this equation has been very successful at predicting the sputtering behavior of amorphous and polycrystalline elemental materials, particularly metals.

Another approach to understanding collisional sputtering processes that has proven fruitful is computer simulation. Simulation codes generally fall into one of two classes, each with its own strengths and weaknesses. In one category are codes based on the binary collision approximation; these are best suited to simulating relatively energetic sputtering processes, and, because of less stringent computing requirements and superior speed, are useful for determining statistical quantities describing sputtering behavior [21]. In the other category are multiple-interaction codes, which simultaneously keep track of all the atoms in the simulated target during each sputtering event. Because they are not subject to the limitations of the binary collision approximation, which fails at very low energies, simulations of this type are better suited to studying the details of mechanisms operating at the

atomic level [22]. The principal disadvantages of multiple-interaction simulations are the necessarily small target size and the large amounts of computing time and memory required.

Unlike collisional sputtering, many aspects of electronic sputtering are not yet very well understood. A simple kinematic mechanism cannot account for the energy transfer that must necessarily take place between electrons and nuclei for sputtering to occur—such a direct transfer is very inefficient because of the large mass differences involved. A number of mechanisms have been suggested to explain the coupling between electronic excitation and atomic motion, but these theories are not sufficiently developed to be able to predict with confidence the electronic sputtering behavior of any particular material. Also, compared to collisional sputtering, relatively few experimental data are available for electronic sputtering.

Several of the theoretical models for electronic sputtering are pertinent to part of the work described here. In the ion-explosion model [23], an energetic ion traveling through a solid is presumed to leave a region of net positive charge in its wake by removing electrons (usually by ejection) from the vicinity of its path. Given suitable conditions, the positive ions remaining in this region will move apart from each other under mutual Coulombic repulsion, converting their electrostatic potential energy into kinetic energy; if they are close to the surface, they may leave the solid altogether. The conditions necessary for this to occur are that the electrostatic stresses in the charged region exceed the bond strengths for the ions, and that the electrical conductivity of the solid be low enough to allow the ions time to move apart before the charged region is reneutralized.

Whereas this mechanism is usually associated with a high density of excitation, electronic sputtering may also result from relatively isolated electronic transitions [24]. An impinging projectile may promote a single atom on the surface from its bound state to an unbound or anti-bonding electronic state. If bonding is lost, the atom will leave the surface with thermal energy; in the other case it will be expelled more energetically. Such mechanisms are often associated with the stimulated desorption of atomic species different from those in the underlying bulk.

One other mechanism of relevance is specific to alkali halides. In these materials, the electronic excitation produced by particle bombardment results in the formation of several types of relatively stable defects. These defects, which form all along the projectile's path, are able to diffuse through the material; those that reach the surface undergo a process that culminates in the release of a neutral halogen atom [25]. Because thermal transport plays a role, this type of electronically mediated sputtering is strongly temperature dependent, in contrast with most other sputtering processes.

1.3 Two Specific Aspects of Sputtering—An Overview

The experimental investigations described in this dissertation were designed to examine two specific aspects of the sputtering process. Although both sets of experiments involved sputtering measurements in the nuclear stopping regime where collisional processes usually predominate, the purpose of the first of the investigations was to look for possible electronic sputtering mechanisms operating in this regime. More precisely, the dependence of the sputtering yield on the charge state of incident keV ions was measured for several different target materials.

As previously mentioned, electronic sputtering is usually associated with ion bombardment in the electronic stopping regime, where the production of the electronic excitations that mediate the sputtering process is due to the transfer of the projectile's kinetic energy to target electrons. The question addressed here was whether or not the *potential* energy carried by a relatively slow, multiply-ionized projectile could give rise to the same sorts of excitations and cause an enhancement in the sputtering yield over that expected from collisional mechanisms alone. Aside from offering further insight into electronic sputtering processes in general, the existence of any particularly efficient sputtering mechanism of this nature would have implications in understanding the sputtering of some solar system materials, and possibly in the design of plasma devices. Such were the motivations underlying this investigation, which is the subject of Chapter 3. Note that these experiments could be realized because of equipment that has become available within this decade,

namely, ion sources capable of producing keV beams of very highly ionized atoms.

The second aspect of sputtering that has been investigated is associated with collisional processes in a complex target—*i.e.*, one that consists of atoms of two or more different masses. At issue is the extent to which the different species will interact kinematically in a collision cascade to alter their respective sputtering yields. In the absence of chemical effects, the lighter species will tend to be sputtered preferentially; such behavior has been observed in elemental materials containing more than one isotope, for example. Linear cascade theory has been extended to include this mass effect for small mass differences in the target, and makes specific predictions about the nature and size of the preferential effects one might expect to observe in a given situation [26]. There are indications, however, that these predictions are not altogether correct. In particular, recent multiple-interaction computer simulations of the sputtering of two-mass targets have produced qualitatively different results [27,28], leading to the suspicion that in this instance some critical information has been lost with the simplifying assumptions made in developing the linear cascade theory. In the experiments described in Chapter 4, targets consisting of two isotopes of a single element, molybdenum, were sputtered with keV ions, and the yields were examined to help resolve this discrepancy. The results from these experiments have several implications, the two most prominent of which have to do with understanding the origin of some isotopic anomalies observed in meteoritic samples, and interpreting measurements made with sputter ion probes.

The general experimental methods employed in both investigations were very similar, and are discussed in Chapter 2. Additionally, some details of the data analysis and one of the analysis techniques, heavy-ion Rutherford backscattering spectroscopy (HIRBS), are elaborated upon in the appendices.

Chapter 2

General Experimental Methods

2.1 Experimental Approach

All of the experiments described in this thesis were based on the same underlying approach: various selected targets were bombarded under carefully controlled conditions with well-characterized beams of ions, and the material sputtered during bombardment was captured on collector foils surrounding each target. The collector foils were subsequently analyzed *ex situ* using either HIRBS or SIMS to determine the density (or densities of different components) of the collected material as a function of position on the foils, and hence as a function of emission direction in the sputtering geometry. Thus, differential angular sputtering yields could be determined from these density distributions. The differential yields, as well as the total sputtering yields calculated by integrating these differential yields, were studied to gain insight into the questions outlined in §1.3.

In the following sections of this chapter, the general experimental considerations and methods relevant to these investigations are discussed. Details concerning procedure, apparatus, and foil analysis that are specific to either the multiply-charged ion (MCI) experiments or the isotope experiments are reserved for the appropriate chapter following this.

2.2 Sputtering Apparatus

The hardware used for holding the targets and collector foils was very similar for both sets of experiments, with only minor differences among the various configurations. The apparatus was mounted on a 20.3 cm diameter stainless steel flange equipped with two linear manipulators and an eight-pin electrical feedthrough. To install the apparatus in the sputtering vacuum chamber, the flange was simply

bolted onto a port of the chamber fitted with a matching flange. The principal components of the apparatus are illustrated in Figure 2.1.

Targets were mounted on a copper block attached to the end of a linear manipulator with 4.3 cm of travel. The target block was fastened to the manipulator in such a manner as to be both electrically and thermally isolated from the manipulator and flange. Up to three targets could be mounted simultaneously on the block, which also held a quartz disk. When this disk was positioned in front of the ion beam, the resulting fluorescence could be viewed from the back side of the apparatus through a window in the vacuum chamber, thus offering a means of visually inspecting the beam spot; the face of the disk was coated with a thin carbon film to prevent the accumulation of electrical charge from the beam.

A resistive wire heater clamped to the back face of the target block could be used to hold the targets at an elevated temperature. The heater was electrically isolated from the block by a thin sapphire plate that at the same time provided excellent thermal contact between the two. The temperature of the block was monitored with a thermocouple.

The collector foil holder was mounted on the second linear manipulator, which had 15 cm of travel; the foil holder was also electrically isolated from the manipulator. Rather than actually using hemispherical collectors that would have subtended the full 2π steradians of solid angle in front of a target, a simpler approach was taken. Foils were fastened to the outside of a cylindrical tube that had semicircular slots cut perpendicular to its axis at regularly spaced intervals along its length (*cf.* Fig. 2.1), thus exposing the inner surface of the foil at each slot. The cylinder was held so that its axis coincided with the center of the target block face, with the slots in view of this face. Thus, when centered in front of a target, an exposed section of foil subtended a portion of the hemispherical region into which material was sputtered that included the full range of polar angles from 0° to 90° at two opposing azimuthal angles. Actually, the range of polar angles did not quite go to 0° because of the small opening in the foil in the normal direction to admit the incident ion beam.

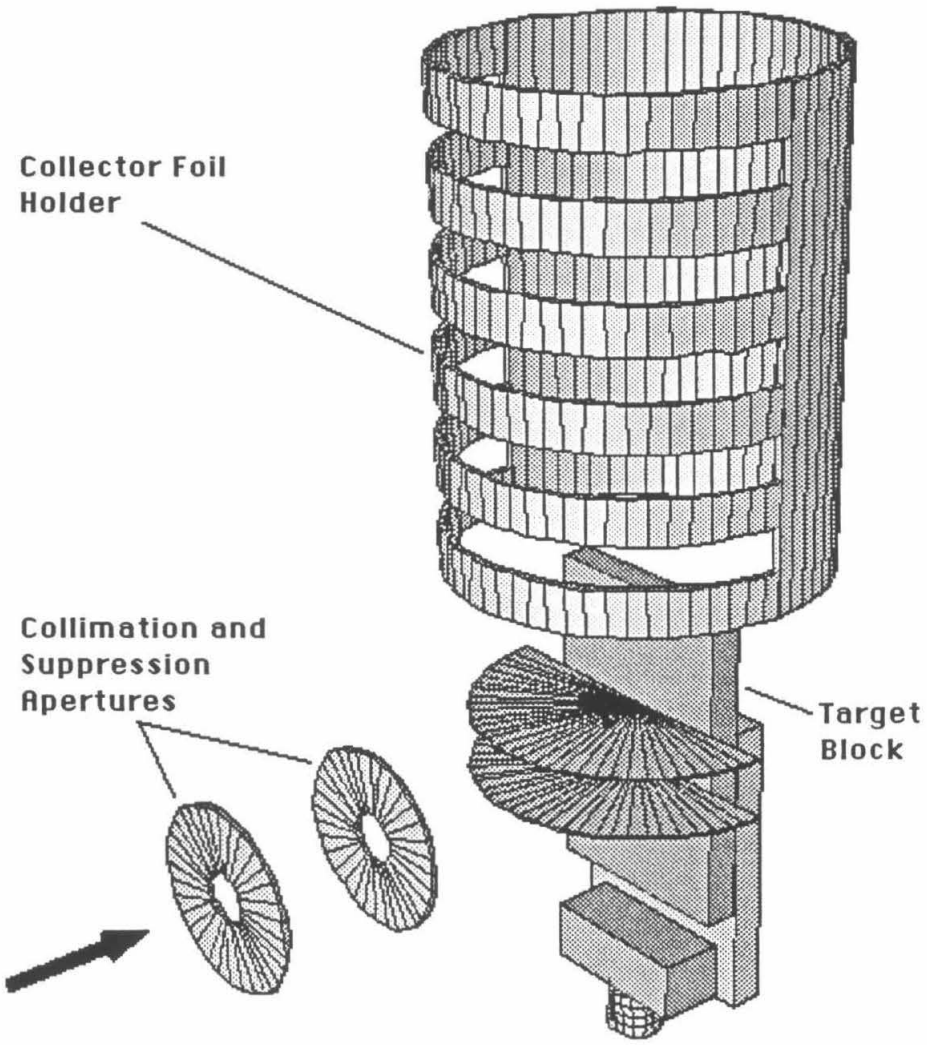

Figure 2.1 Illustration of the major components of the sputtering apparatus. The collector foil holder is shown pulled out of the way, with no foils mounted. (Were foils in place, they would cover the slots in the cylinder, except for openings to admit the incident ion beam.) The target block is shown on its mount, along with the two semicircular vanes that allowed isolation of one collection region at a time during sputtering. The heavy arrow indicates the path of the ion beam.

Two semicircular vanes were mounted perpendicular to the target block face and the axis of the foil holder. Located immediately in front of the target block on either side of the beam path, these collimating vanes made it possible to sputter onto only one exposed region of the collector foil at a time. This feature in conjunction with the ability to translate the foil holder made it possible to carry out multiple bombardments without opening the vacuum chamber containing the sputtering apparatus.

Two diaphragms were mounted in front of the foil holder to collimate the ion beam before it passed through the opening in the collector foil on the way to the target. Electrical leads from these collimators, as well as from the foil holder, the target block, the heater and thermocouple, were brought out of the vacuum chamber via the electrical feedthrough in the flange.

2.3 Considerations for Maintaining a Clean Target Surface

The condition of the surface of a solid being sputtered can significantly influence the resulting sputtering behavior. A very large fraction of the sputtered atoms originate from the first two monolayers of the surface [29,30]; furthermore, the ejection energy of sputtered particles tends to increase with their depth of origin [31]. If the surface is contaminated with hydrocarbons or adsorbed gases, for example, the resulting sputtering yield from the bulk can be strongly affected because the surface monolayer is of a different composition than the bulk, and possibly because the binding forces at the surface are altered. If the surface remains contaminated under steady-state sputtering conditions, the total sputtering yield from the bulk will probably be reduced, the differential yield with respect to emitted energy will be altered, and the differential angular yield for the bulk material will change shape [32]. This last is because atoms originating from deeper within a solid tend to be emitted in directions closer to the target normal than those arising from closer to the surface [29,30]. Although energy distributions were not an immediate concern in these experiments, the other two quantities were, so that it was desirable to maintain atomically clean target surfaces during sputtering to avoid any of the

above complications and interferences. The measures taken to meet this criterion are described below. Unfortunately, no means was available during the experiments to check explicitly that the targets remained clean. Thus, parts of the following discussion are necessarily somewhat general.

Under steady-state sputtering conditions, two competing processes are occurring at a target's surface. Molecules in the residual gas above the surface are impinging on the surface with thermal energies, and some of these molecules are adsorbed. At the same time, atoms are being removed from the surface by the sputtering process. Thus, the condition for maintaining a clean surface during sputtering is given by

$$r \cdot f < Y \cdot I, \tag{2.1}$$

where r is the rate at which residual gas molecules are incident on the surface in units of molecules $\mathrm{cm}^{-2}\ \mathrm{s}^{-1}$, f is the 'sticking' probability, or probability that such molecules are adsorbed, Y is the sputtering yield, and I is the particle current density of the sputtering beam. If this condition is satisfied, the adsorption of residual gases striking the sputtered surface cannot keep pace with the rate at which material is dislodged from the surface, so that the surface will become atomically clean and remain that way.

In general, the best way to satisfy Relation (2.1) is to reduce the quantities on the left-hand side, which is equivalent to reducing the monolayer formation time at the target's surface. For an ideal Maxwell-Boltzmann gas of molecules of mass m at temperature T and pressure P, the number of molecules striking a unit area of surface per unit time is given by

$$r = \frac{P}{\sqrt{2\pi m k T}}, \tag{2.2}$$

where k is Boltzmann's constant. For N_2 or CO gas at room temperature, for example, a monolayer of adsorbed gas will cover any freshly exposed surface after a time

$$t \sim \frac{2.6 \times 10^{-6}}{fP}\ \mathrm{s}, \tag{2.3}$$

where f is again the sticking probability, P is in units of Torr, and a monolayer is assumed to contain $\sim 10^{15}$ molecules cm^{-2}. Equation (2.3) shows that one can increase the monolayer formation time by reducing either the pressure above the surface in question, or the sticking probability for impinging molecules, or both.

The primary measure taken to achieve a clean target surface in these experiments was to reduce P by conducting the sputtering bombardments under UHV conditions. To this end, materials with very low vapor pressures were employed in the fabrication of the sputtering apparatus described in the preceding section. The principle materials used were 304 stainless steel, oxygen-free high-conductivity (OFHC) copper, machinable ceramic, and alumina tubing. The components were cleaned prior to assembly using standard procedures [33], which at the very minimum included vapor degreasing in trichloroethylene and concluded with a series of ultrasonic baths in deionized water and reagent grade isopropyl alcohol, and drying in a warm-air stream. The metal parts were also acid-etched in intermediate steps to remove surface layers containing large quantities of gases that would otherwise outgas; the stainless-steel parts were put through a second etch to 'passivate' the surface layer to inhibit subsequent diffusion and escape of gases dissolved in the bulk. Cleaned parts were handled only with plastic gloves and clean tools.

The vacuum chambers used to hold the sputtering apparatus for the different experiments were all constructed of 304 stainless steel, and (with a couple of exceptions in the chambers used for MCI experiments) employed metal gaskets and metal-seal valves throughout so that they were bakeable to several hundred degrees Celsius. The chambers were equipped with either an ion pump or a cryopump for normal operation, and sorption pumps to provide for initial evacuation without the risk of hydrocarbon contamination.

After a chamber was loaded with the sputtering apparatus and evacuated, it was baked with externally-wrapped heating tapes for a period ranging from a few hours to a few days, depending on the circumstances. Baking temperatures were typically between 250° C and 300° C. This primarily hastened the removal of adsorbed water vapor from the system, and allowed adequately low base pressures

to be attained much more rapidly than would have otherwise been possible. Base pressures during the experiments were in all but one case at or below a few times 10^{-9} Torr. At these pressures, the principal residual gases in the system were probably H_2 and CO [Ref. 34,p. 419], and the time for monolayer formation would have been several hundred seconds, assuming unity sticking probability.

During the actual sputtering bombardments chamber pressure invariably rose slightly, particularly in the ion-pumped chamber, because of the introduction of noble gas (Ar or Xe) from the sputtering beam; neither ion pumps nor cryopumps are capable of pumping these gases very rapidly. In the worst cases, pressure rose to a few times 10^{-8} Torr. Fortunately, the sticking probabilities for noble gases are considerably less than unity, so that these gases should not have contributed substantially to adsorbed layers covering exposed surfaces. To ensure that this was true for the targets, the following precaution was taken.

From thermodynamic treatments of adsorption, one finds in general that surface coverage by a gas has a strong temperature dependence. Following Langmuir's treatment, for instance, this coverage is approximately proportional to $P \cdot \exp(-U_B/kT)$ at very low pressures, where U_B (which is negative) is the binding energy for a gas molecule on a surface [35]. Hence, if the binding energy of the gas in question is not too large compared to the thermal energy kT of atoms at the surface, one can effectively reduce surface coverage by increasing the thermal energy, *i.e.*, by heating the target. The condition that the binding energy not be too large is usually satisfied by relatively inert species such as the noble gases that are said to be 'physisorbed;' this approach will not work well for 'chemisorbed' species (such as H_2, CO, and O_2, particularly on metal surfaces) for which binding energies are much larger. So, to minimize possible surface coverage by noble gases and other weakly bound species, the targets were maintained at an elevated temperature—at least 150° C—throughout the experiments by means of the target block heater. Because of this, the base pressure (without beam) should have been adequate for calculating monolayer formation times and evaluating Relation (2.1).

The above arguments primarily address the maintenance of a clean surface

under steady-state sputtering conditions. At the outset of sputtering in these experiments, however, some gas molecules were certainly adsorbed on the target surfaces. To remove this adsorbed layer, which probably did not exceed a single monolayer in most instances, the targets in the MCI experiments were all sputtered for an initial period without a collector in position. Furthermore, the sputtering doses used in the MCI experiment were large enough that even without the sputter-cleaning, surface contaminants would have been removed in a time small compared to the total bombardment time.

This initial sputter-cleaning was not possible in the isotope experiments because the transient behavior in the early stages of sputtering was of primary interest here. A further complication is that the Mo targets used would have been prone to oxidation; in fact, it is likely that oxygen would have displaced other surface contaminants [Ref. 34,p. 87]. Such a surface oxide layer would not necessarily have been confined to a single monolayer thickness. This aspect of the isotope experiments will be discussed further in Chapter 4.

2.4 Characterization of Bombardment

Two other important elements in the execution of these sputtering measurements were careful selection of the characteristics of the projectiles inducing the sputtering, and determination of the number of such projectiles incident during each bombardment. Relevant characteristics of the projectiles included atomic species, kinetic energy, charge state, and direction of incidence with respect to the target surface. By fixing all of these variables at known values, the complexity of the physical process was reduced as much as possible. The second element, measurement of the sputtering dose, was necessary to quantify sputtering yields and to be able to compare the results from different bombardments. In addition to the absolute number of bombarding particles, the number incident per unit area was of importance, particularly for the isotope experiments.

The choices for the projectile atomic species were restricted to the noble gases. This was necessary because of the importance of avoiding any potential chemical

interaction between projectile and target. Compounds formed from such interactions will often have binding energies different from that of the original material, and may consequently have different sputtering yields. In extreme cases, a newly formed compound may be so weakly bound that it can escape from the target's surface with thermal energy. Hence, because of their chemical inertness, noble gas atoms are ideal choices when seeking to avoid such potential interferences.

Standard methods were used to select the mass, energy, and charge state of the projectiles. A beam of ions accelerated through a known potential was passed through a sector magnet that acted as a momentum filter; except for accidental coincidences that were easily avoided, the transmitted beam was uniquely determined. As for the choice of the ion beam's direction of incidence at the target, the direction along the target normal was selected because of its high symmetry and corresponding simplicity. This direction was fixed in the design of the sputtering apparatus.

Because the projectile charge state was known, the bombarding dose could be determined by measuring the electrical charge carried to the target by the ion beam. This was complicated by the probable presence of electrons traveling with the ion beam that had been ejected from collimators and walls upstream from the target, and by the ejection of secondary charged particles from the target itself during bombardment.

To prevent the loss of the secondary charged particles from the target, the collector foil assembly and collimating vanes (*cf.* §2.2) were connected electrically to the target holder to form a 'Faraday enclosure' that minimized the open solid angle through which such secondaries could escape. The electrical current from this Faraday enclosure was sent to a current digitizer and scaler to measure the actual incident charge. (Note that special measures had to be taken when bombarding the insulating targets in the MCI experiments; these measures are discussed in the next chapter.) The digitizer's input represented a virtual ground, so that the collector and target assemblies were at essentially the same electrical potential as the flange and chamber walls. This scheme was chosen after experimenting with various

electrical biases on the different components; in almost all cases, bias voltages degraded current integration because of leakage currents to ground or attraction of charged particles from outside the assembly.

The diaphragms mounted in front of the foil holder also played an important role in the beam current integration. The purpose of the first of these apertures was to collimate the ion beam so that none of the incident ions could strike the outside of the collector foil instead of the target. (Such a stray current would have caused the sputtering yield to be underestimated.) This collimator also served to define the beam envelope at the target surface so that the area of the bombarded region could be determined. The second diaphragm, which had a slightly larger aperture than the first, was designed to transmit the ion beam but at the same time stop the majority of the ions scattered or ejected from the rim of the first collimator. Additionally, this diaphragm was biased negative with respect to the first to prevent secondary electrons traveling with the the beam from reaching the target. The magnitude of the bias voltage was generally chosen to be several hundred volts. This is considerably larger than one might estimate to be necessary from kinetic considerations alone: the maximum energy that an ion can transfer to a free electron in a collision is

$$E_e = E_i \cdot \frac{4M_1 m_e}{(M_1 + m_e)^2} \cong E_i \cdot \frac{4m_e}{M_1}, \tag{2.4}$$

where m_e and M_1 are the electron and ion masses, respectively, and E_i is the ion's initial energy. For 50 keV Ar, for example, this is less than 3 eV. The bias voltage needed to be much larger than this to suppress adequately the less predominant but much more energetic electrons produced in Auger processes.

2.5 Limitations of the Collector Technique

There are several limitations associated with the collector technique used in these experiments. One of the limitations is inherent to all collector-type sputtering experiments; the others are related to the design of the equipment used here and the methods used to analyze the collectors after sputtering.

The limitation that is inherent to all collector-type sputtering experiments has to do with the efficiency with which sputtered material is captured on the collectors; this sticking probability is not necessarily unity, as would be ideal. If the sticking probability is very much smaller than unity or changes significantly as a function of the amount of material already collected, the technique ceases to be very useful. If the probability is at least close to unity and is relatively constant as a function of coverage, it will enter into the absolute calibration of sputtering yield measurements, but will not pose a significant problem when making relative measurements under similar conditions.

The reasons for sputtered particles not sticking with unit probability to surfaces they encounter are not very well understood, particularly for heavy particles incident on light substrates. The sticking coefficient will in general depend on the atom-collector combination, and even on the condition of the collector surface. In the absence of any accurate theory for calculating the sticking probability for a given situation, one must often resort to experimental measurement of this quantity. For almost all of the materials sputtered in these experiments, relevant values for the sticking probabilities either were found in the literature or were measured, at least to an extent necessary to indicate whether the corresponding sputtering measurements might be seriously compromised. One of these sticking measurements is discussed in detail in Appendix A.

The design of the collector apparatus used in these experiments imposed another limitation on the collector technique as implemented here. Because the collection regions exposed to the targets subtended only a portion of the 2π steradians into which material was sputtered, the measured differential angular sputtering yields and the corresponding calculated total sputtering yields may not be particularly meaningful unless the angular distributions of sputtered material had azimuthal symmetry, a condition that is not generally true for monocrystalline targets. Thus, the apparatus used here was best suited for measuring the sputtering yields from amorphous or polycrystalline materials. The metal targets sputtered in these experiments fulfill this criterion. Two monocrystalline materials were sputtered in the

MCI experiments, but the results for these targets are considered reliable because of mitigating circumstances discussed in the next chapter.

Two constraints were imposed on these experiments by the techniques chosen to measure the densities of sputtered material on the collector surfaces. The first concerned the possible choices for target and collector foil materials. HIRBS offers a fast, convenient, and fairly sensitive means of measuring small concentrations of atoms on surfaces, provided the substrate is lighter than the atoms of interest and contains no impurities with masses comparable to or heavier than the atoms of interest. (See Appendix B for a detailed discussion.) Thus, the technique is ideal for analyzing sputtering collectors, as long as the target material is heavier than the collector material. This means that the most versatile collectors will be made of very light, very pure materials. In these experiments, collector foils of both aluminum and carbon were used; this restricted the choice of target materials (or components of materials) that could be studied to those more massive than aluminum.

The second constraint imposed by the analysis techniques concerned the densities of collected sputtered material required for the foil analysis to be completed on a realistic time. The lower limit on acceptable densities was a few times 10^{13} atoms cm^{-2} for both the HIRBS and SIMS analyses. This imposed a restriction on the minimum sputtering dose for which yields could be effectively measured, a significant factor in the isotope experiments because of the transient effects being investigated.

Chapter 3

Sputtering by Multiply-Charged Ions

3.1 Introduction

As mentioned in §1.2, electronic sputtering is usually associated with fast ions having energies of MeV/amu, and has been observed to predominate in a number of dielectric materials including alkali halides, frozen gases, organic compounds, and some oxides [17,18,36-38]. This type of sputtering arises from the formation of regions of intense ionization along the projectile track near the target surface [39], or from the production of weakly bound defects or anti-bonding states of atoms at the target surface. In alkali halides, the generation of bulk defects that subsequently diffuse to the surface and release halogen atoms remains the dominant sputtering mechanism even down into the keV regime [36].

The production of ionized or excited electronic states underlying electronic sputtering usually derives from the electronic stopping of the projectile in the target—*i.e.*, from the transfer of the ion's kinetic energy to target electrons through direct collisions. Consequently, because of associated changes in the scattering cross section, changes in the projectile's charge state have been observed to have a pronounced effect on the sputtering yield at high energies [37]. It seems quite plausible that the projectile's charge state may play a significant role in the sputtering process at lower energies as well—either through this sort of mechanism, or via the neutralization process itself. The ionization potential energy (possibly augmented by excitational energy) carried by a slow, multiply-charged ion can approach or even exceed its kinetic energy; the transfer of this potential energy to the target during the ion's neutralization may produce the same sorts of excitations in the target that give rise to electronic sputtering at higher projectile energies. The importance (or even the existence) of such a role is not yet established; should it prove to be of

consequence, then such potential-energy effects would have to be taken into consideration when describing some low-energy sputtering processes where hitherto only kinetic energy and collisional effects have been included.

Several investigators have examined this question recently [40-46] by looking for anomalous changes in the yields of both neutrals and ions sputtered from various targets by keV particle beams ranging from neutral to highly ionized. The number of materials studied thus far is limited, however, and the data are not all in agreement. Conductors, as anticipated because of their short electronic relaxation times, have been observed to exhibit no change in sputtering yield as a function of projectile charge state [41,44], but the results for semiconductors and insulators are not so decisive.

Si has received considerable attention, first from Arifov *et al.* [40], who sputtered samples with 1–10 keV Al^{q+} ($1 \leq q \leq 7$) and observed the secondary ion yield to increase (by an overall factor of ~ 1.7 at 10 keV) with increasing projectile charge state. Bitenskii *et al.* [47] proposed that this enhancement was due to a Coulomb-explosion mechanism that should contribute to the neutral sputtering yield as well. In apparent support of this, Eccles *et al.* [44] found the total Si sputtering yield produced by 10 keV Ar^+ to be 2.4 times larger than that for neutral Ar projectiles of the same energy. However, de Zwart *et al.* [45] saw only the increase in secondary ion yield with projectile charge state when they bombarded Si with 20 keV Ar^{q+} ($1 \leq q \leq 9$)—they measured no change in the predominant neutral sputtering yield.

The data for insulators show some indications of a charge-state related sputtering component, but again there are inconsistencies. Eccles *et al.* saw the total sputtering yield of glass increase by a factor of 2.6 in going from neutral Ar to Ar^+; on the other hand, Della-Negra *et al.* [46] measured no change in the Si^+ yield when they bombarded SiO_2 with 18 keV Ar^{q+} ($1 \leq q \leq 11$). Alkali halides have also been studied by several workers. Arifov *et al.* found an essentially linear relationship between the secondary ion yield from LiF and the projectile's ionization potential energy for a variety of slow, multiply-charged ions. Radzhabov *et al.* [43] sputtered KCl with 0.1–10 keV Ar^{q+} ($1 \leq q \leq 5$), reporting increases in the yields of both

neutrals and positive secondary ions (by overall factors of $\sim$ 1.4 and $\sim$ 1.2 at 10 keV, respectively) with increasing projectile charge state. In contrast with these results, Della-Negra *et al.* observed no change in the Cs^+ yield when they bombarded CsI with various charge states of Ar.

In spite of the obvious discrepancies, which may be attributed in large part to the variety of experimental conditions, most of these results indicate that the charge carried by a slow projectile can at least influence the electronic state of the ejected material. The extent to which this charge can influence the magnitude of the overall sputtering yield is less clear, however. Very few of the materials which are known to exhibit enhanced sputtering in the electronic regime (and which consequently are among the best candidates for charge-enhanced sputtering in the keV regime) have been studied, probably because of experimental difficulties associated with the accumulation of charge on these targets during bombardment. In the work described in this chapter, targets of two such materials, the alkali halide cesium iodide (CsI) and the important opto-electronic material lithium niobate ($LiNbO_3$), have been sputtered under well-defined conditions with different charge states of 48 keV Ar ions. A target of the conductor Au has also been sputtered with 60 keV beams of the same species. The collector method described in Chapter 2 was used to measure the total (neutral plus ionic) differential angular sputtering yields and total integrated yields, and the results have been examined for variations as a function of the projectile charge state. Whereas the yield from the Au target was found not to change, slight enhancements were observed in the yields from the insulating targets as the projectile charge state increased, indicating that a charge-related sputtering mechanism may be operating in these materials. This contribution was relatively small, however, contributing at most 10-15% of the total sputtering yield in these measurements.

3.2 Experimental Methods

The sputtering experiments were carried out in two different cryopumped UHV chambers on beam lines adjoining Lawrence Berkeley Laboratory's electron cyclotron

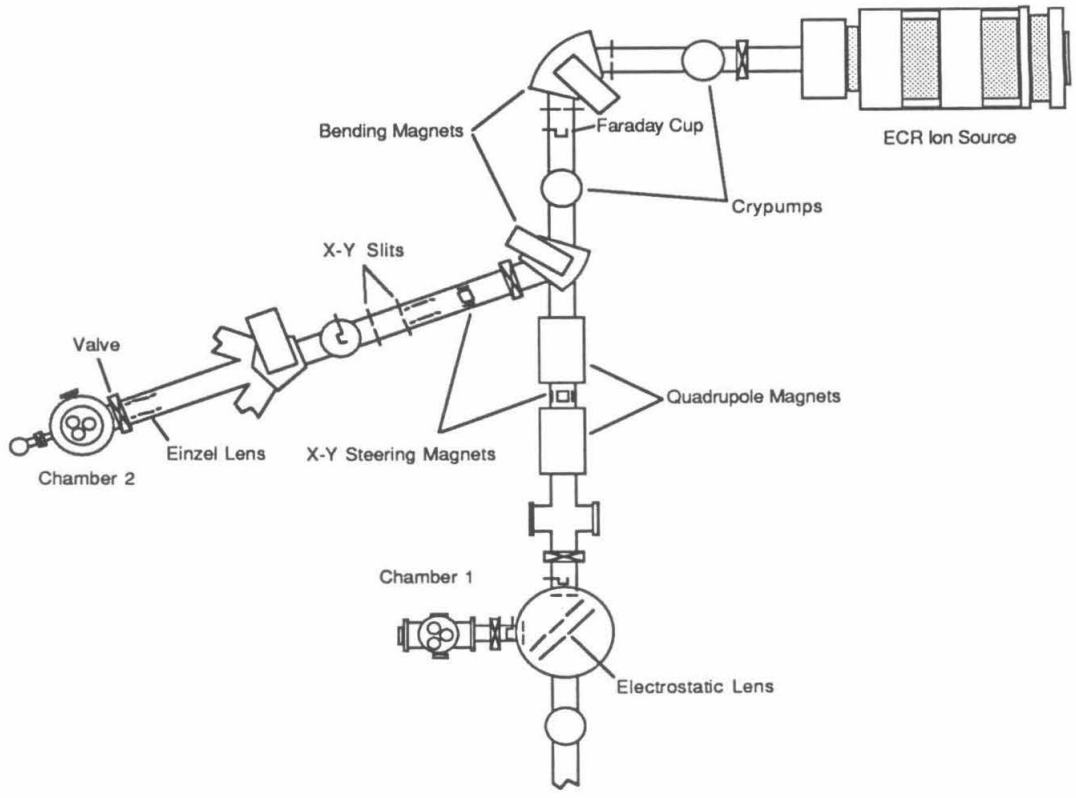

Figure 3.1 Schematic layout of the ECR ion source, beam line and target chambers. This equipment was situated on the roof of Lawrence Berkeley Laboratory's 88-Inch Cyclotron.

resonance (ECR) ion source. The layout of the accelerator, beam lines, and chambers is shown schematically in Figure 3.1. Beams produced by the ion source were directed through a 90° analyzing magnet before being deflected along the beam path to the appropriate chamber. Chamber 1 in Figure 3.1 was used for the initial experiment with the Au target; here an electrostatic mirror was used to deflect the ion beam from the main beam line into the chamber. Chamber 2, which was added later, was used for the experiments with the insulating targets; a second sector magnet directed the ion beam into this chamber, and an einzel lens was installed just upstream from the chamber to facilitate focusing the beam on the target.

Ar was selected as the projectile to avoid interference from chemical interaction

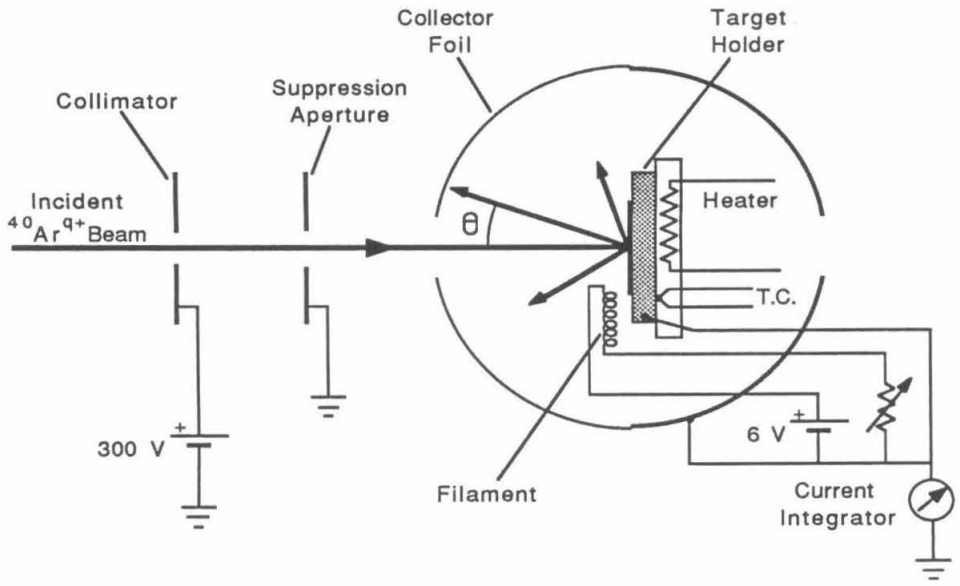

Figure 3.2 Schematic of the sputtering apparatus, showing the target and collector foils, and the configuration for current integration including secondary electron suppression. Note that the collimating vanes (not shown) were also connected to the current integrator to complete the Faraday enclosure.

with the targets, and because its atomic number is large enough to allow for the production of ions with very large ionization potential energies. The choices for beam charge states and kinetic energy were constrained by the capabilities of the ion source and bending magnets; the range 4+ to 11+ at 48 keV (and 60 keV for the initial experiment with Au) was selected because it offered the greatest variation in ionization potential energy. The ground-state ionization potential energies for the ions used are 144 eV, 578 eV, and 2018 eV for Ar^{4+}, Ar^{8+}, and Ar^{11+}, respectively.

The sputtering geometry is depicted schematically in Figure 3.2. The apparatus used to hold the targets and collector foils was as described in §2.2, and for these measurements the collector cylinder had a radius of 3.8 cm. The collector foils themselves were of 25μm-thick 99.997%-pure Al, and subtended polar angles (measured from the target normal) from 7° to 90°, with a gap in the normal direction to admit

the beam. The semicircular collimating vanes in front of the target were mounted directly on the flange holding the apparatus, so that they stood independent of both the target block and collector cylinder in this configuration.

The aperture farthest upstream from the target block collimated the incident ion beam onto a spot $\sim$ 8.5 mm in diameter at the target. This collimator was biased at +300 V and and the second, downstream aperture was placed at ground potential to suppress secondary electrons ejected from the rim of the first. To prevent the accumulation of charge on the insulating targets during bombardment, two tungsten filaments in a battery-driven current loop were suspended just in front of the target block to serve as sources of neutralizing electrons. These filaments were incorporated into the collimating-vane assembly, as shown in Figure 3.3. Currents from the target, collimating vanes, filament loop, and collection foils were monitored during sputtering, and their leads were connected to form a Faraday enclosure for purposes of current integration. (The current from the filament loop was of particular interest because it served as an indication of whether the CsI and $LiNbO_3$ targets remained insulating throughout the bombardments.) The uncertainty in dose measurement, based on the solid angle not subtended by the Faraday enclosure and worst case assumptions for secondary electron production, was $\sim$3%.

The targets sputtered were a polished (112) CsI crystal doped with 5-10 ppm Tl, a polished y-cut $LiNbO_3$ crystal, and a 99.95%-pure rolled polycrystalline Au foil 23.6 mg cm^{-2} thick. Target selection was intended to complement the HIRBS analysis of the foils after sputtering; to this end materials with relatively massive components were chosen. CsI is also less hygroscopic than other commonly available alkali halides with heavy constituents, which simplifies target handling.

The CsI and $LiNbO_3$ targets were given an ultrasonic isopropanol bath and dried in warm air before being loaded into the UHV chamber; the Au foil was rinsed for $\sim$ 1 min in diluted *aqua regia* beforehand. As discussed in §2.3, the chambers were baked for several hours at $\sim$ 300°C after the sputtering flange was mounted, and the targets were held at elevated temperatures throughout the experiments. The $LiNbO_3$ target was maintained at $\sim$ 340°C, the CsI target at $\sim$ 320°C,

and the Au foil at $\sim 210°C$ during the respective experiments. The targets were sputter-cleaned initially; this also reduced the possibility of error due to transient nonstoichiometric sputtering effects in the CsI and $LiNbO_3$ samples, and crystalline effects (by randomizing the surface layers) in the latter [48]. The pressure in Chamber 2 during the experiments with the CsI and $LiNbO_3$ targets was $\sim 7 \times 10^{-9}$ Torr with beam; projectile fluxes during these experiments ranged from $2 \times 10^{12}\,cm^{-2}\,s^{-1}$ for the Ar^{11+} beam to $\sim 2 \times 10^{13}\,cm^{-2}\,s^{-1}$ for both the Ar^{4+} and Ar^{8+} beams.

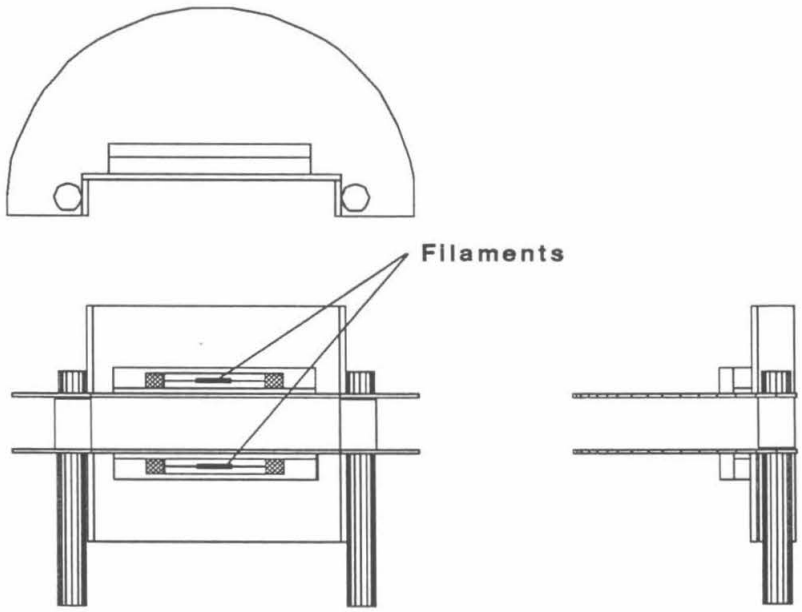

Figure 3.3 Illustration of the collimating-vane assembly used for these measurements, viewed from three different angles. The large surfaces perpendicular to the vanes were ~ 3 mm from the target block. The tungsten filaments used as electron sources during the bombardment of the insulating targets are indicated.

Under these conditions, Relation (2.1) should have been satisfied even without heating the targets. (It was necessary to rely somewhat on the elevated target temperature to maintain a clean surface during the initial experiment with the Au foil, where the pressure in Chamber 1 was $\sim 3 \times 10^{-8}$ Torr and beam fluxes ranged from $8 \times 10^{10}\,cm^{-2}\,s^{-1}$ to $6 \times 10^{11}\,cm^{-2}\,s^{-1}$.) Particle doses for each charge state were

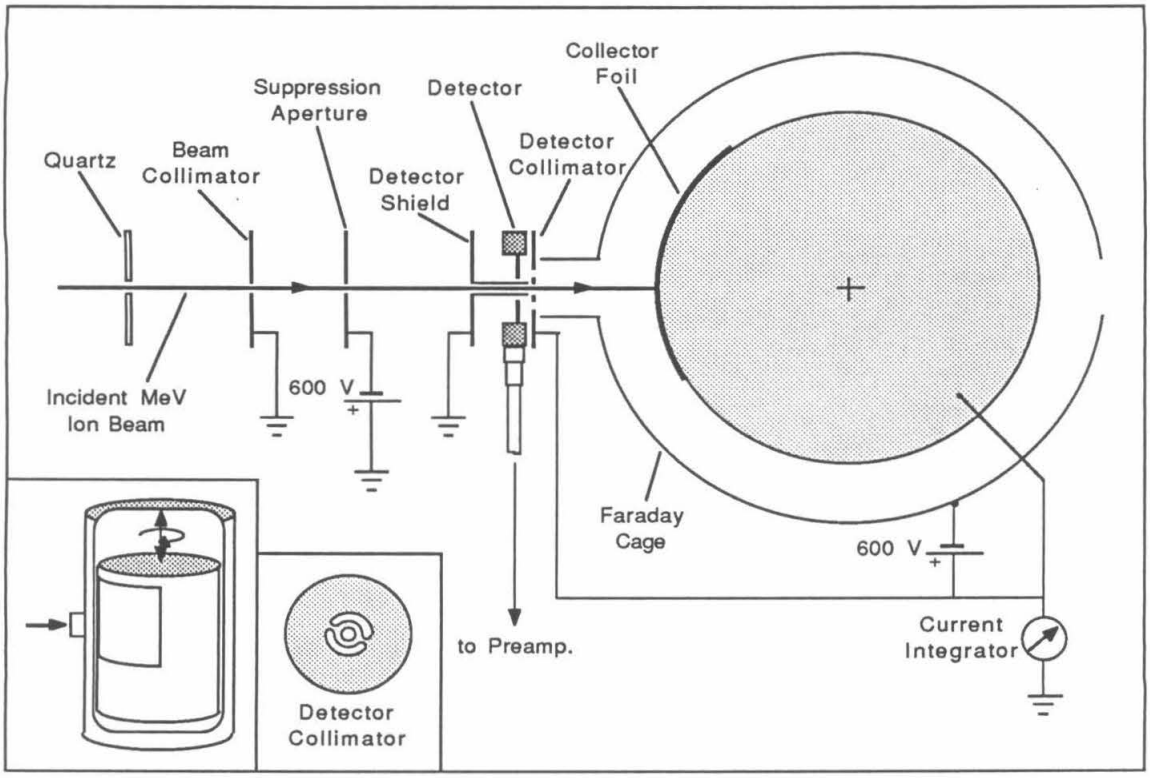

Figure 3.4 Schematic of the HIRBS apparatus used for analysis of the collector foils. See Appendix B for further details.

$\sim 3.5 \times 10^{16}\,\mathrm{cm}^{-2}$ for the CsI target, $\sim 6 \times 10^{16}\,\mathrm{cm}^{-2}$ for the $LiNbO_3$ target, and $\sim 1 \times 10^{16}\,\mathrm{cm}^{-2}$ for the Au target.

After the sputtering of each target was completed, the collector foils were removed from the UHV chamber and transported in air to another chamber for the HIRBS analysis. Figure 3.4 shows a schematic of the setup. The foils were mounted, collection side out, on a cylinder that could be rotated and translated to position the foils as desired in front of the collimated analyzing beam. A 10 MeV $^{16}O^{2+}$ beam generated by the California Institute of Technology's 6 MV Tandem Van de Graaff accelerator was used for the backscattering analysis of the collector foils for the CsI and Au targets; a typical HIRBS spectrum from the analysis of the latter is shown in Figure 3.5. A 16 MeV $^{35}Cl^{4+}$ beam was used to analyze the collector foils for the $LiNbO_3$ target. (Note that Nb was the only component sputtered from the

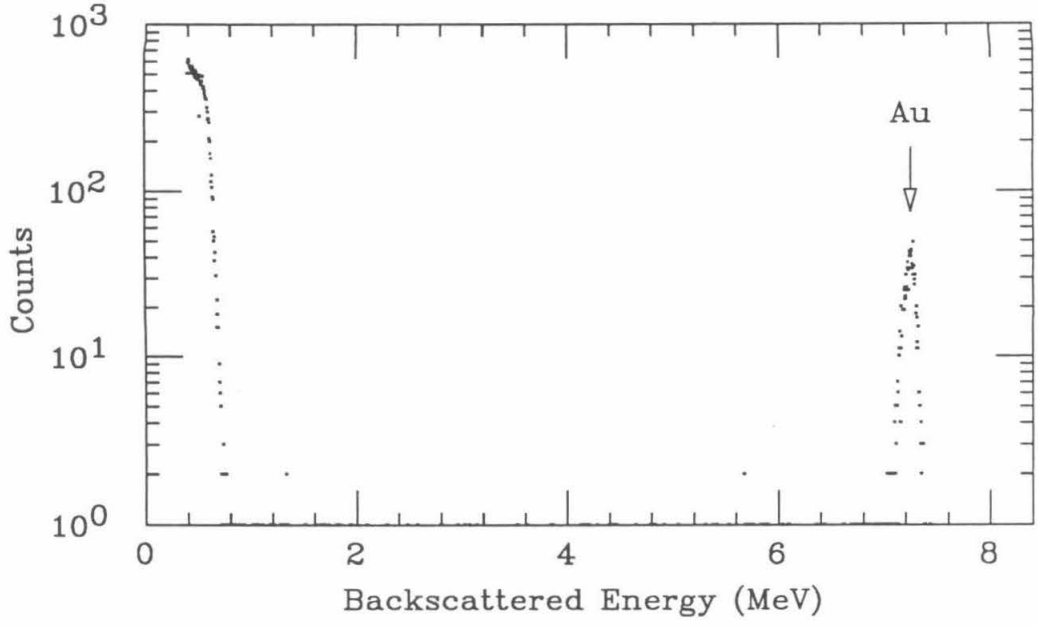

Figure 3.5 A representative spectrum from the HIRBS analysis of the collector foils for the Au target. The large signal at the low-energy end of the spectrum is from the Al foil itself. Note that the vertical scale is logarithmic.

$LiNbO_3$ target heavy enough to be measured.) Typical analyzing fluences for the HIRBS measurements were $\sim 1 \times 10^{14}\,cm^{-2}$, which should have been small enough to minimize errors associated with resputtering the collected material. Atomic coverages on the foils ranged downward from $6 \times 10^{17}\,cm^{-2}$ for the sputtered Cs and I (combined—the two elements could not be resolved in the analysis), $2 \times 10^{15}\,cm^{-2}$ for the sputtered Au , and $6 \times 10^{14}\,cm^{-2}$ for the sputtered Nb. Uncertainty in the determination of surface density, including uncertainty in current integration, dead time correction, scattering cross section, and typical statistical uncertainty in the yields, is estimated to be ~3%. Further details of the HIRBS analysis technique are discussed in Appendix B.

A concern with using hot filaments as the source of neutralizing electrons for the insulating targets during sputtering was the possibility of contaminating the sample surfaces with tungsten. No tungsten was observed on the collector foils during analysis, however, indicating that this was not a problem.

One final experimental detail involved the $LiNbO_3$ target. During the sputter-cleaning of this material, the neutralizing current drawn from the filament loop was observed to drop significantly, which indicated a change in the insulating nature of the target. As an explicit check on the electrical character of the sample's surface, its sheet resistivity was later measured with a four-point probe. The sheet resistivity in the pristine region was beyond registration on the instrument used ($> 10^{10}\,\Omega$); in the sputtered region it was $\sim 10^{8}\,\Omega$.

3.3 Analysis and Results

After the density of sputtered material was determined as a function of position on the exposed regions of the collector foils, and hence as a function of polar angle in the sputtering geometry, the resulting angular distributions were each fit with a function of the form

$$N(\theta) = \frac{N_0 A \cos^B \theta}{r^2}. \tag{3.1}$$

Here N is the areal density of the collected material; θ is the angle from the target normal; N_0 is the number of incident Ar ions; r is the radius of the collector foil; and A and B are fitting parameters. (Note that for the Nb distributions, N is actually a partial density of collected material.) The fitting procedure also took into account the various possible offsets and misalignments in the sputtering geometry. These included the known target offset from the collector center in the direction normal to the target, offset of the beam spot from the collector center in the plane of the target, and angular offset from the orientation of normal beam incidence. Details of these corrections in the fitting procedure are described in Appendix C.

Figure 3.6(a) shows a typical angular distribution of collected material, and its fitted function. (Uncertainties shown in this and subsequent figures in Chapter 3 are $\pm 1\sigma$.) Shown in Figure 3.6(b) are the corresponding distribution and fit after removing the effects of the various offsets mentioned above and multiplying by r^2/N_0 to give the desired normalization. As was the case for all the Nb and CsI distributions, the largest source of asymmetry in this example was beam offset in the plane of the target. This was not so for the distributions from the Au foil,

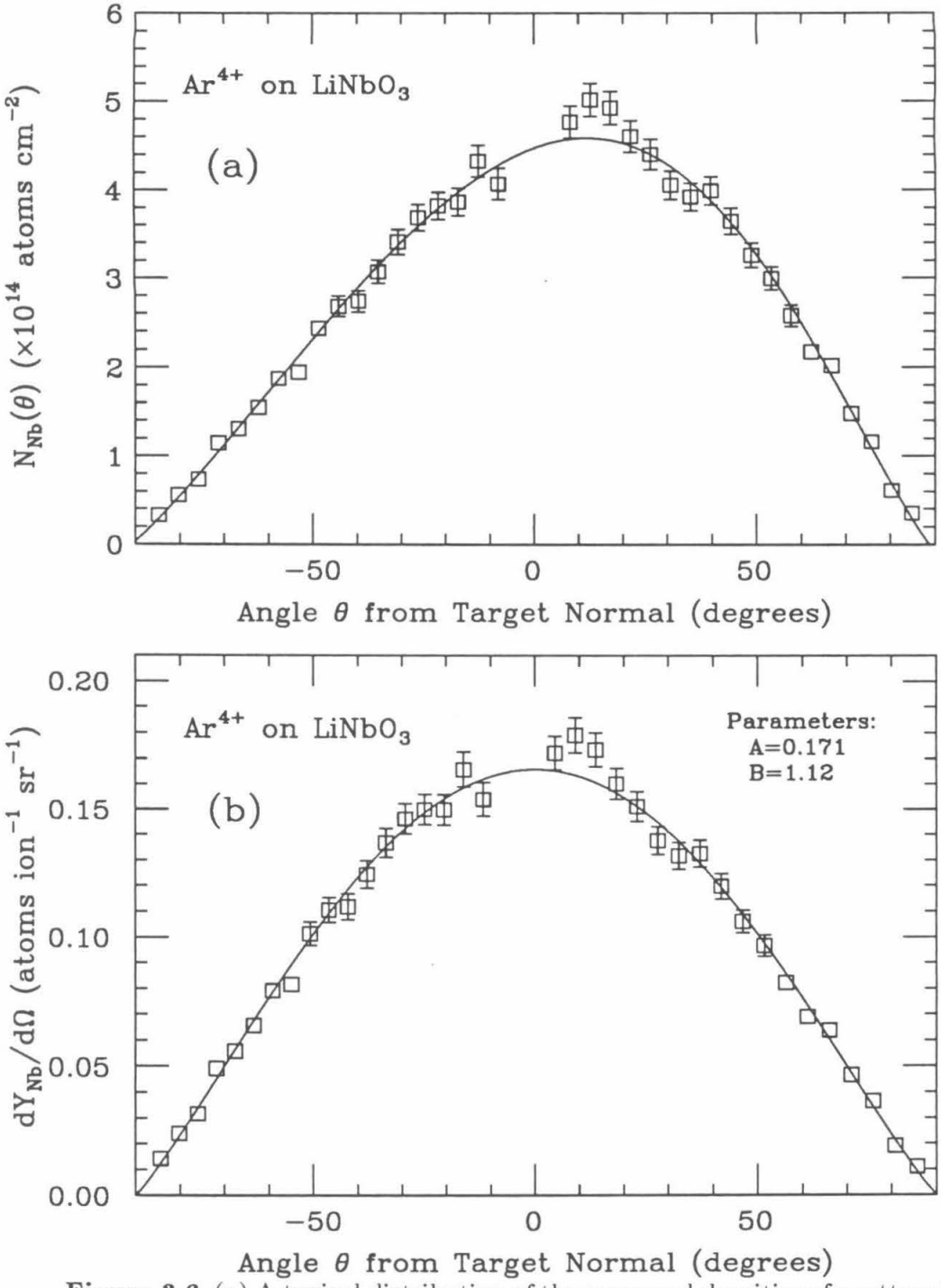

Figure 3.6 (a) A typical distribution of the measured densities of sputtered material and the corresponding least-squares fit, uncorrected for misalignments in the sputtering geometry. Only random errors are included in the indicated uncertainties. (b) The normalized differential angular sputtering yield and fit for the Nb component sputtered from the $LiNbO_3$ target by 48 keV Ar^{4+} [obtained from the distribution shown in (a)].

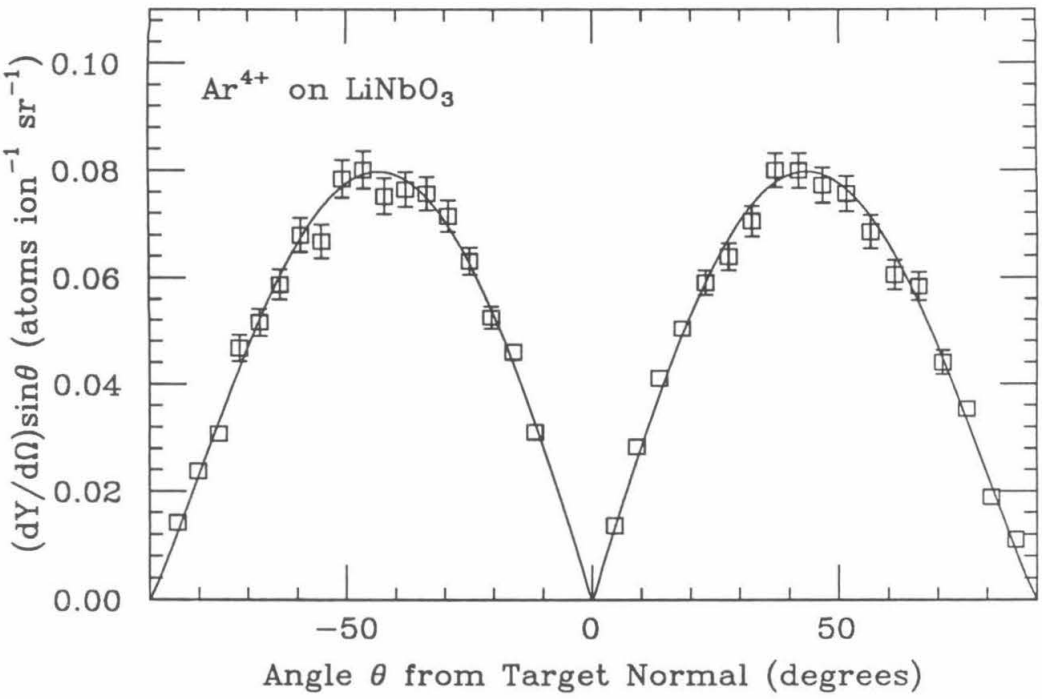

Figure 3.7 The differential angular sputtering yield and fit of Figure 3.6(b), weighted by the solid angle factor $\sin\theta$, to illustrate the relative importance of different regions of the normalized distribution to the total sputtering yield.

where other asymmetries appeared, apparently due to the development of uneven topography or texturing at the surface of this polycrystalline target [32,49]. Because of these asymmetries, uncertainties in the quantities obtained from the angular distributions of Au are larger than for the other materials.

The normalized differential sputtering yield, $dY/d\Omega = A\cos^B\theta$, determined from each angular distribution, gives the number of atoms sputtered per unit solid angle in the direction θ per incident ion. To calculate the corresponding total sputtering yield, Y, this quantity was integrated over the 2π steradians of the hemisphere in front of the target:

$$Y = \int_0^{2\pi} d\phi \int_0^{\pi/2} A\cos^B\theta\sin\theta\, d\theta = \frac{2\pi A}{B+1}. \tag{3.2}$$

Figure 3.7 is a plot of the same distribution and fit shown in Figure 3.6(b), this time weighted by the solid angle factor $\sin\theta$ to show the relative importance of the

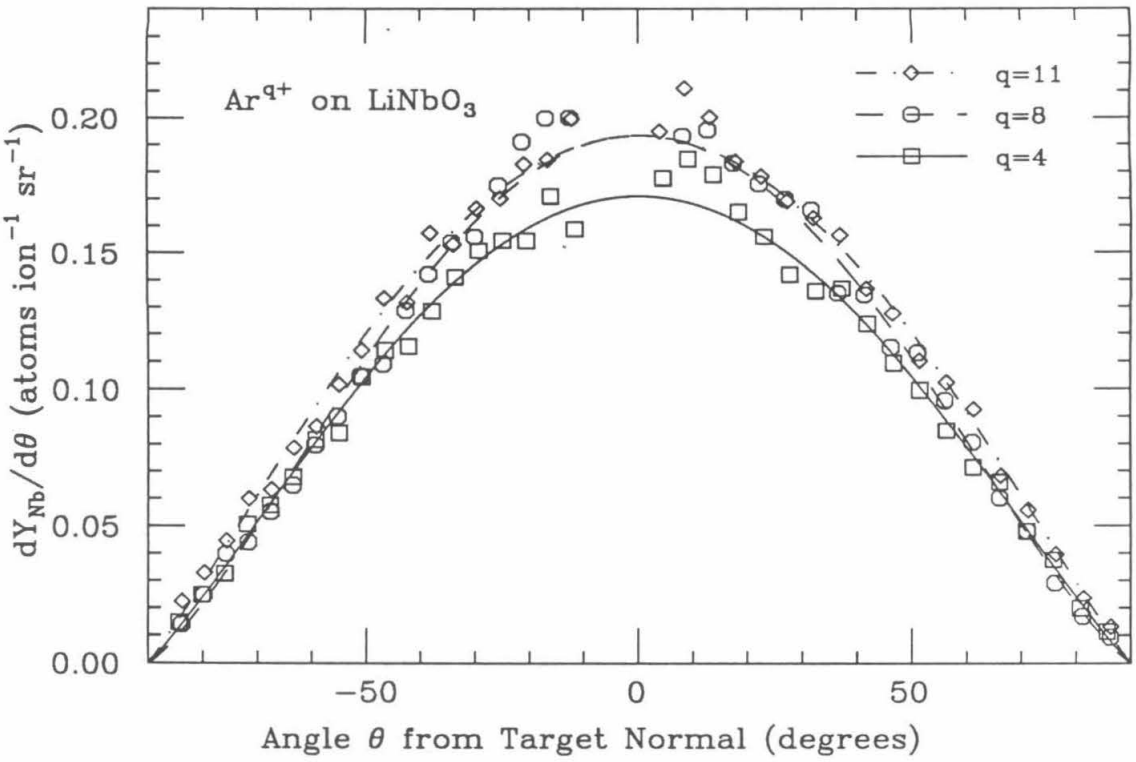

Figure 3.8 Superposition of the differential angular sputtering yields of the Nb component from the $LiNbO_3$ target for all three charge states of Ar. Fitting parameters are, for Ar^{4+}, $A = 0.171$, $B = 1.12$; for Ar^{8+}, $A = 0.193$, $B = 1.25$; and for Ar^{11+}, $A = 0.193$, $B = 1.07$.

various regions of the distribution to the total yield; in particular, this shows the insensitivity of the calculated total yield to the fit in the region closest to the target normal (where it generally was poorest).

The normalized differential angular distributions and fits from the Ar^{4+} bombardments of the $LiNbO_3$ and CsI targets are plotted in Figures 3.6(b) and 3.9, respectively, to show clearly the shapes of the distributions for the two targets and the uncertainty in the data. Figures 3.8 and 3.10 show the superposed distributions for all three charge states of Ar on the $LiNbO_3$ and CsI targets, respectively, to emphasize the differences between the different distributions. Table 3.1 presents the fitting parameter B as an indication of the shape of the differential angular sputtering yield for each of the charge-state/target combinations, as well as the integrated

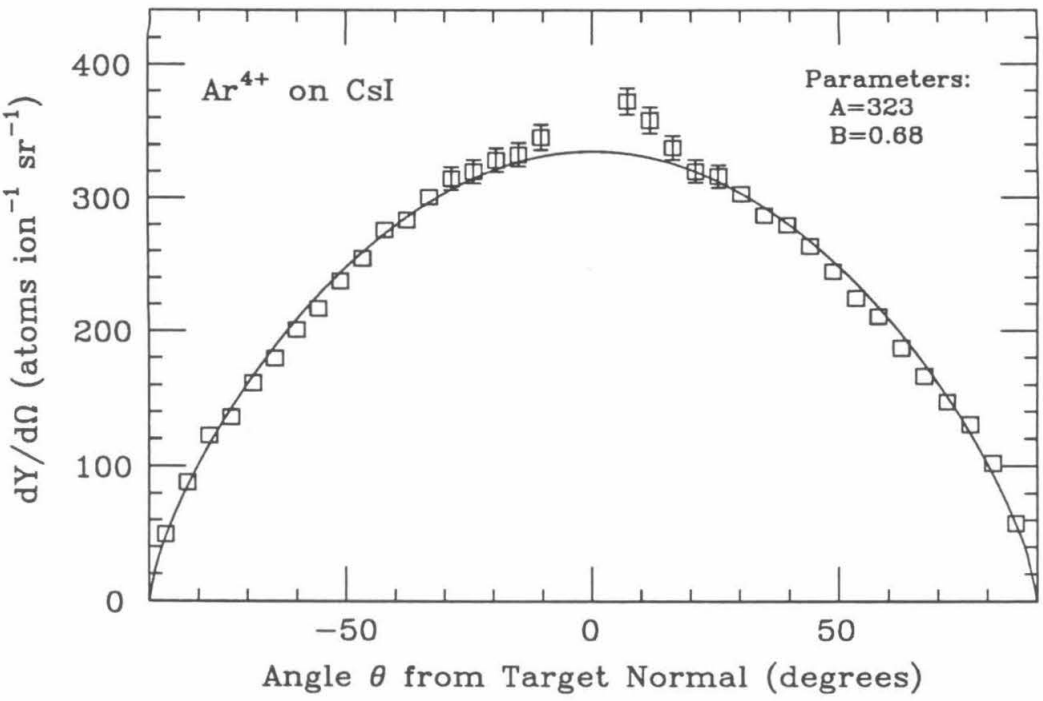

Figure 3.9 The combined differential angular sputtering yields of Cs and I sputtered from the CsI target by 48 keV Ar^{4+}.

sputtering yield Y from each bombardment. These total yields, normalized to the yield from the appropriate Ar^{4+} bombardment (or the average of the Ar^{4+} bombardments, in the case of the Nb data), are also plotted as a function of projectile charge state q for each target in Figure 3.11. The two points for Ar^{4+} on the $LiNbO_3$ target indicate the reproducibility of the data for each charge-state/target combination.

Absolute uncertainties for the total sputtering yields in Table 3.1 are somewhat larger than the uncertainties given there, which do not include errors common to the different bombardments. In addition to possible systematic errors in sputtering dose estimation or in the HIRBS measurements, there are uncertainties associated with the sticking probabilities for the various sputtered atomic species incident on the collector foils. These uncertainties may also be treated as systematic because collection conditions were nearly identical for the different bombardments of each of the targets. The sticking probability for Ar-sputtered Au incident on a native

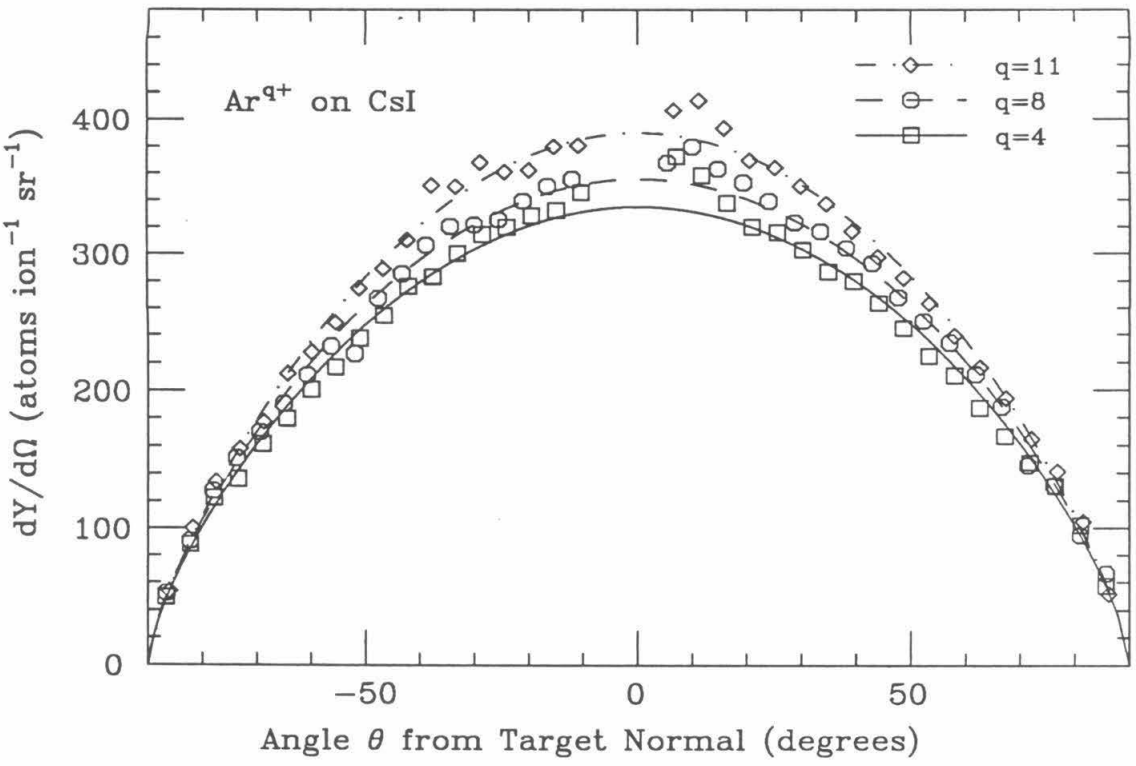

Figure 3.10 Superposition of the differential angular sputtering yields of CsI for all three charge states of Ar. Fitting parameters are, for Ar^{4+}, $A = 323$, $B = 0.68$; for Ar^{8+}, $A = 358$, $B = 0.69$; and for Ar^{11+}, $A = 390$, $B = 0.73$.

aluminum oxide is $0.92^{+.08}_{-.10}$ for coverages less than $\sim 10^{16}\,\mathrm{cm}^{-2}$ [50]; the corresponding probability for Ar-sputtered Nb is $0.97^{+.03}_{-.08}$ [51]. (See Appendix A for a description of the measurement of the Au sticking probability.) These factors—but not the uncertainties—have been included in the total yields presented in the table, and (for Nb) in Figures 3.6(b), 3.7, and 3.8. For Au in particular, the small fraction of atoms that did not stick on first impact resulted in a low "background" level of material on the foils: densities did not go completely to zero at 90° from the target normal. For Cs and I, the sticking probability has been assumed to be unity, and hence absolute values for the total sputtering yield of CsI may be underestimated. However, absence of significant "background" densities in this case tends to support this assumption.

Table 3.1 Differential angular sputtering yield shapes and total sputtering yields.

Target	q	B^a	Y (atoms/ion)
$LiNbO_3^b$	4	$1.12 \pm .02$	$0.51 \pm .01^c$
	4^d	$1.08 \pm .03$	$0.54 \pm .01$
	8	$1.25 \pm .03$	$0.54 \pm .01$
	11	$1.07 \pm .02$	$0.58 \pm .02$
CsI	4	$0.68 \pm .01$	1250 ± 30
	8	$0.69 \pm .01$	1320 ± 30
	11	$0.73 \pm .01$	1420 ± 60
Au foil[e]	4	$1.97 \pm .11$	$9.7 \pm .3$
	8	$2.03 \pm .14$	$9.1 \pm .3$
	11	$2.20 \pm .13$	$9.3 \pm .6$

a. Fitting parameter indicating shape of distribution. See text.

b. Values presented pertain to Nb component only.

c. Uncertainties in Y don't include errors systematic to all charge states.

d. Particle flux was reduced to match the Ar^{11+} bombardment.

e. 60 keV Ar ions were used for these three bombardments.

3.4 Discussion

It is apparent from Figures 3.11 and Table 1 that no particularly dramatic variation in the sputtering yields was observed as the Ar charge state increased—none of the quantities determined varied by more than $\sim$ 15%. Within experimental uncertainty, Au exhibited no changes, whereas CsI and $LiNbO_3$ both showed slight enhancements of 10–15% in overall sputtering yield with increasing projectile charge state. From these results alone it is difficult to make any quantitative statements about the underlying processes, but one is able to make several qualitative observations.

At the velocities in question, a projectile's equilibrium charge state inside a solid is essentially that of a neutral atom; consequently, ions will undergo neutralization by intense electron capture from the target, beginning even before they actually reach the surface. This neutralization proceeds via a series of resonant-capture

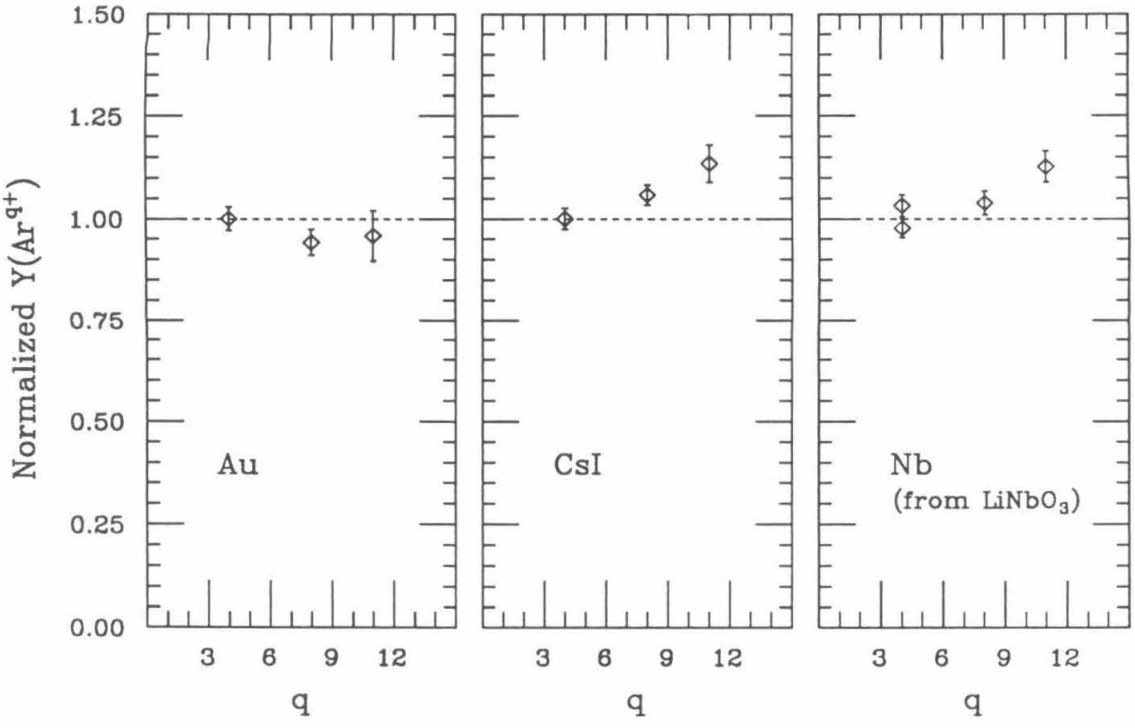

Figure 3.11 The total sputtering yield, scaled such that the Ar^{4+} yield is equal to unity, plotted as a function of projectile charge state q for all three targets. (The Nb yield is actually a partial sputtering yield; also, here the scaling factor was determined from the average of the Ar^{4+} bombardments.) Note that only for the data from the Au target can one determine a constant value for the yield that does not lie well outside the standard error of at least one of the data points.

and Auger transitions, each requiring 10^{-14}–10^{-15} s to complete and (in the latter case) covering a most probable energy step of $\sim 20\,\mathrm{eV}$ [52]. The number of steps to neutralization can thus be quite large for projectiles with very large ionization potential energies, and because this process commences only when the wavefunctions of the involved electronic states start to overlap appreciably (beginning when the ion is at most some tens of ångströms from the surface), the ion's velocity critically determines whether it is completely neutralized by the time it reaches the surface.

If an ion is traveling slowly enough to be neutralized before penetrating the solid, then its subsequent behavior in the bulk of the target will not differ from that of an initially neutral projectile. These situations *will* differ at the target's

surface because of the potential energy transferred from the incident ion to the surface as the ion is neutralized. Some of the ion's potential energy will be carried away by the low-energy electrons emitted in the Auger processes, but by virtue of these same electrons, the net charge deposited at the surface can be more than that initially carried by the projectile (not including the contribution of true secondary electrons).

If, on the other hand, an ion is traveling fast enough to still retain some of its charge when it reaches the surface, then the target region contributing to the neutralization will extend beneath the surface, and the density of deposited charge will be reduced. At the same time, however, the projectile's scattering cross section may differ from that of a neutral atom as it traverses the near-surface region, changing the rate of kinetic energy loss. The nuclear cross section may be slightly larger because the projectile's nuclear charge is not as well screened, and, as is true at higher energies, the electronic stopping power for the ion will be enhanced with charge. (Although electronic stopping isn't the predominant means of energy loss at keV energies, it is not entirely negligible—for 48 keV Ar in $LiNbO_3$, it is $\sim 30\,\mathrm{eV\,\AA^{-1}}$, or $\sim 40\%$ as large as the average energy loss due to nuclear stopping [53].)

Thus, the precise role of charge state in the ion-target interaction, and hence in any possible ejection mechanisms, will depend upon the projectile's velocity. In this experiment, the Ar beams had velocities of $\sim 5 \times 10^5\,\mathrm{m\,s^{-1}}$, and based on secondary electron emission data from metals [52], it is improbable that the Ar^{8+} or Ar^{11+} ions were completely neutralized before impact. Consequently, one cannot distinguish on the basis of these measurements between enhancements in the sputtering yield that are due solely to the potential energy carried by the projectile, or to the same dynamic mechanisms seen in the MeV regime associated with electronic stopping.

Also, in the above arguments it has been tacitly assumed that the incident ion is in its ground state. If the ion is initially in a highly excited state, it will deexcite during the neutralization process; this combined neutralization and deexcitation will occur via the same types of processes as the neutralization of a ground-state

ion, although the number, sequence, and rate of steps involved may differ. The additional potential energy associated with the excitation will be dissipated in the same ways as the ionization potential energy, and will contribute to the creation of excited electronic states in the target.

ECR ion sources such as the one used in this work are known to produce ions in metastable excited states [54]; these states live long enough to have reached the targets in our experiments. If one assumes that in an ion beam such excited states are populated approximately according to their statistical weight, then for all three charge states of Ar used in these experiments, the majority of ions reaching the targets would have been in excited states. For Ar^{4+} and Ar^{11+}, these excitations are not expected to have made any appreciable difference in the observed sputtering behavior because the energies of the excitations are quite small compared to the ground-state ionization potential energies. For Ar^{8+}, however, this statistical argument predicts that nearly 85% of the ions would have been in excited states with energies almost half as large as the ionization potential energy. It is unlikely that the percentage of ions in these excited states was actually this large, although certainly a non-negligible fraction of the ions in the beam would have been excited. The implication is that for Ar^{8+} it is not possible to completely distinguish between excitational and charge-related effects.

The ionized and excited electronic states produced in a solid through either the neutralization (and deexcitation) or kinetic energy loss of an ion can relax via a number of potential mechanisms. These include the diffusion of electrons and holes (possibly preceded by the decay of bound electron-hole pairs into free pairs), phonon and plasmon production, radiative deexcitation, and atomic displacement, the last of which can generate a variety of defects in the target and is the only one that might lead to sputtering. The actual means of deexcitation will depend upon the properties of the target; only if other (faster) routes are unavailable can atomic motion and sputtering result. In Au, as in other conductors, electronic relaxation is governed by the response time of the "electron gas," which varies as the inverse of the surface plasmon frequency, ω_s^{-1}, and is $\sim 10^{-16}$ s for Au. The

time scale required for nuclear motion to occur is $\sim 10^{-13}$ s. Hence, for Au and for metals in general, there is no opportunity for electronic excitation to lead to sputtering, and the only possible charge-related effect would have to arise from a changed nuclear scattering cross section of the projectile (which would contribute directly to the number of target atoms set in motion). The absence of any effect in these measurements indicates that nothing of this nature is taking place. This null result for Au is in accord with the reports of others [41,44]; also, the overall yields measured are in good agreement with those in the literature [16].

For the insulating materials, it is known from high energy measurements that excited electronic states can live long enough to lead to nuclear motion and sputtering [17,18]. The results for CsI and $LiNbO_3$ do show slight increases in sputtering yield with increasing projectile charge state, but it is apparent that there are no dominant ejection mechanisms operating here that are strongly coupled to charge-related excitations.

The CsI sample exhibited a very large overall sputtering yield, which is consistent with the yields observed for other alkali halides under similar conditions [36]. The magnitude of the yields is attributed to a mechanism of electronic origin operating in the bulk—energy lost by the slowing projectiles produces electron-hole pairs which subsequently relax to form one of several types of relatively stable defects characteristic of alkali halides [25]. These defects can diffuse through the material, and if they reach the surface, eject a neutral halogen atom. If the sputtering is of prolonged duration, the surface will eventually become enriched in the alkali metal unless this species vaporizes at a rate sufficient to maintain stoichiometry. In this experiment, the elevated temperature of the CsI target thus had two effects: first, it greatly enhanced the thermally activated diffusion of these defects, leading to the extremely large yield; second, it raised the vapor pressure of Cs well beyond that necessary to prevent surface enrichment [55]. The "under-cosine" shapes of the angular distributions are due at least in part to this thermal release of one of the sputtered constituents. (Note also that the thermally released material certainly had azimuthal symmetry; this cannot generally be said of the ejected halides, al-

though the large yields indicate that the target surface was probably disordered enough for the same to be true in this experiment.)

Such a sputtering mechanism represents an obvious path by which projectile charge could contribute to the overall sputtering yield in this material. Either the neutralization process or a varying electronic cross section could lead to the production of additional defects and thus enhanced sputtering. Another suggested mechanism for direct ejection in alkali halides, known as the Knotek-Feibelman mechanism, has been shown not to work in simulations [24]. This process would involve the transformation of a halogen anion at a surface lattice site into a cation (I^+ in this case) that would subsequently be ejected from the surface by Coulombic repulsion from its neighbors. Instead of being ejected in the simulation, the ion was trapped and the energy dissipated in distortion of the surrounding lattice. This result casts doubt upon the possibility of Coulomb-explosion mechanisms in alkali halides, and supports the idea that any enhanced sputtering is due to augmentation of the already existing process outlined above.

Because keV ions are neutralized before or soon after they penetrate a solid, any charge-related contribution to the sputtering yield will necessarily arise at or near the surface. In alkali halides, the entire region of the target penetrated by the projectiles can contribute to the overall sputtering yield to some degree, but by reducing the target temperature (inhibiting diffusion of defects from deep within the target) or the projectile kinetic energy (increasing the ionization potential's fraction of the total energy), the relative size of any charge-related effect should be enhanced. This could explain why Radzhabov *et al.* observed a larger relative charge-state dependence in the alkali halide KCl than was seen here in CsI.

$LiNbO_3$ differed considerably from CsI in its sputtering behavior in this experiment. Although the relative variations in yield with projectile charge state were comparable for the two materials, the absolute magnitudes were very different. The size of the overall yield for $LiNbO_3$ (which was ~ 2.7 atoms ion^{-1} if the Li and O components are included) is consistent with that expected from a purely collisional process. Also, the shapes of the angular distributions of Nb very nearly match the

ideal $\cos\theta$ shape predicted by linear cascade theory. Whereas the evidence is not quite so compelling for CsI, here it is apparent that whatever mechanism is responsible for the small charge-related contribution is different from that associated with the biggest part of the yield. It is difficult to make any specific conjectures about the nature of the contribution—this material is not so well understood as the alkali halides. Note that the dramatic change in conductivity observed during the sputtering of this material is consistent with the reports of others [56], and is a consequence of the rapid formation of a heavily damaged surface layer during bombardment. (The randomization accompanying this damage also assured that the angular distribution of sputtered would have azimuthal symmetry.) Finally, the shape of the angular distribution of Nb from the Ar^{8+} bombardment is sharper than for the other charge states. Ar^{8+} differed from the other two projectile species in that it was likely to have been in a highly excited state, although whether this is related to the shape of the angular distribution is unclear. The difference may be an experimental artifact.

3.5 Summary and Outlook

KeV beams of Ar ions with charge states 4+, 8+, and 11+ have been used to sputter several different target materials. No change was seen in the sputtering yield of Au with increasing projectile charge state, and enhancements of 10-15% were observed in the yields of the insulating materials CsI and $LiNbO_3$. Under the experimental conditions, it is probable that the more highly ionized projectiles used were not fully neutralized before penetrating the insulating targets, so that it cannot be determine whether the small effects observed were due to the actual deposition of the charge carried by the projectiles or to modified projectile cross sections near the surface. In CsI, it is likely that any addition to the sputtering yield with charge is through the already predominant mechanism involving electronic production of defects. In all cases, the role of projectile charge state in the overall sputtering process was minor under the conditions of this investigation.

It would be interesting to repeat the measurements for the insulating materials

using projectiles with considerably smaller kinetic energies, so that the relative size of the potential energy carried by each ion is increased with respect to its total energy. This would presumably enhance the charge-related contributions to the sputtering yield with respect to the total, and might permit the relationship between projectile charge state and yield to be better quantified. Such an experiment would also help to remove ambiguity about whether the projectiles are completely neutralized by the time they penetrate the surface, a question that represents a very interesting and relatively untouched subject in its own right for insulating materials.

Chapter 4

Preferential Sputtering of Isotopic Mixtures

4.1 Introduction

Collisional sputtering processes in single-component targets have been widely studied and are relatively well understood, particularly in the linear cascade regime. For multicomponent targets, on the other hand, quantitative understanding of the corresponding sputtering behavior is much more limited, and even some qualitative aspects of such processes have not yet been resolved. In general, the different species in a multicomponent material will not be sputtered in proportion to their relative abundances in the bulk; the nature and extent of such *nonstoichiometric* or *preferential* sputtering will be determined by kinetic and chemical interactions among the different species involved in the process.

In the sputtering of alloys and compounds, the variety of contributing factors greatly complicates any analysis of preferential sputtering. One can eliminate much of the complexity by sputtering targets containing several isotopes of a single element; this effectively isolates preferential effects associated with mass differences and the kinetics of the collision cascade, and removes effects due to component-specific interaction cross sections and chemistry. In addition to the insight it can offer into the sputtering of multicomponent materials in general, understanding the nonstoichiometric sputtering of multi-isotopic targets is of interest for several other reasons as well: such processes probably played a role in altering the isotopic composition of the lunar surface and the surfaces of other planetary satellites [7,57-63], and sputtering may have contributed to the anomalous isotopic composition of some meteoritic materials [9,64]; sputter-induced isotopic fractionation is a concern with any quantitative surface analysis technique such as SIMS that relies on sputtering to remove sample material [65-68]; finally, preferential sputtering might be applied constructively in isotope separation under favorable circumstances [69].

Unless a sputtered target happens to be liquid, preferential sputtering will induce changes in the composition of the target's surface over time. The surface layer will ultimately become enriched in the component(s) with the smaller sputtering yield(s), and the composition of the sputtered flux will necessarily become identical to that of the target bulk under steady-state conditions. Other processes that occur during sputtering may also contribute to the modification of the surface layer's composition, and hence the sputtering yield; these include recoil implantation, collisional mixing, and radiation-enhanced diffusion and segregation [70]. Such transport processes will determine the depth of the altered surface layer, for example. The compositional alteration of the target by any or all of the above processes is usually regarded as a secondary effect of sputtering. To study the primary preferential sputtering effects for a multicomponent target, then, it is desirable to limit the projectile fluence as much as possible—to much less than 10^{15} ions cm^{-2}, ideally—to avoid interference from these secondary effects.

There have been several experimental investigations into the sputtering behavior of multi-isotopic targets. These studies may be grouped into three different categories according to the measurement techniques employed. The categories include collector experiments in which the predominant neutral sputtered flux was measured, often as a function of emission angle in the sputtering geometry; measurements in which the sputtered target rather than the ejected material was analyzed; and secondary ion measurements in which the isotope ratio of the sputtered ion flux was monitored as a function of bombarding fluence.

Before reviewing these various experiments, it is appropriate to introduce the following standard notation for describing the measured ratio R_{ij}^{M} of two isotopes i and j in relation to their ratio R_{ij}^{STD} in a standard sample. The relative enrichment or depletion of isotope i with respect to j is given by

$$\delta_{ij} = \left(\frac{R_{ij}^{M}}{R_{ij}^{STD}} - 1\right) \times 1000, \tag{4.1}$$

where δ_{ij} is expressed in parts per thousand (permil, or ‰). In sputtering experiments, R_{ij}^{STD} is often obtained from an unsputtered portion of the target, or from

the steady-state ratio of isotopes i and j in the sputtered flux.

The first experiment designed to look for isotopic effects in sputtering was performed by Fluit *et al.* [71], in which they bombarded lithium metal targets with beams of Ar^+ to fluences of $5.3 \times 10^{16} cm^{-2}$. The sputtered material was captured on quartz collectors and was transferred to a surface-ionization mass spectrometer for analysis. They reported light-isotope enrichments $\delta(^6Li/^7Li)$ of ~17‰ and ~19‰ for bombardment with 5 keV and 20 keV Ar^+, respectively.

In another important collector experiment, Russell *et al.* made a careful study of the sputtering of Ca isotopes from several calcium-bearing minerals [72]. They bombarded targets of fluorite (CaF_2), fluorapatite [$Ca_5(PO_4)_3F$], and plagioclase ($CaAl_2Si_2O_8$) with beams of N^+ and N_2^+, and captured the sputtered material on stainless steel collectors; the sputtered material was rinsed from these collectors and analyzed using thermal ionization mass spectrometry to determine the $^{40}Ca/^{44}Ca$ ratio with a precision of ~0.3‰. They found that the material sputtered with the lowest bombarding fluences was enriched in the lighter isotope, but that this enrichment disappeared quickly with increasing fluence. For the plagioclase target, which was bombarded with 130 keV N_2^+, $\delta(^{40}Ca/^{44}Ca)$ was 21.2‰ for the lowest fluence of 5.8×10^{17} ions cm^{-2}; the corresponding value for the fluorapatite target, which was bombarded with 100 keV N^+, was 11.5‰ for a fluence of 1.2×10^{17} ions cm^{-2}; the fluorite target, also bombarded with 100 keV N^+, exhibited enrichments of 11.1–12.7‰ for low-fluence bombardments of $1.3–2.4 \times 10^{17}$ ions cm^{-2}. The yields from the fluorite target were also examined for angular variation in $\delta(^{40}Ca/^{44}Ca)$; at the lowest fluence, δ values of 13.3‰, 17.3‰, and 8.0‰ were measured for the polar-angular ranges 5–25°, 25–41°, and 41–72°, respectively. At higher fluences, as the absolute enrichment of the light isotope decreased, the relative enrichment came to decrease monotonically with increasing polar angle and became even more pronounced.

Other collector-type experiments have been performed, but at much higher bombarding fluences. Wehner [69] and Olson *et al.* [73] sputtered metal targets of Cu, Mo, W, and U with 60-300 eV Hg^+ from a low-pressure Hg plasma to fluences

$\gtrsim 10^{21}$ ions cm^{-2}. Using SIMS to analyze most of the collectors, they found in all cases that the lighter isotopes were enriched in directions close the the target normal and depleted at oblique angles, a result consistent with the observations of Russell *et al.* The magnitude of this enrichment was found to decrease with increasing ion energy; for Mo, for example, the ratio of the relative abundance of ^{92}Mo in the normal direction to its relative abundance in oblique directions changed from 1.044 to 1.019 when the ion energy was increased from 100 to 200 eV. In other work, Wang *et al.* sputtered Cu with 50 keV Ar^+ to fluences of 1.2×10^{19} ions cm^{-2}, and reported an absolute enrichment of the *heavy* isotope in the sputtered material at all polar angles [74]. The apparent absence of isotope conservation and the large ($\sim$10%) scatter in the data from the SIMS analysis of the collectors in this experiment cast some doubt on the validity of the results, however.

An experiment that falls into the second category outlined above was performed by Arai *et al.*, in which they sputtered thin films of Mg with 2 keV He^+ to fluences between $\sim 10^{17}$ and 10^{18} ions cm^{-2} [75]. The films, which ranged in thickness from 270 to 1700 Å, were evaporated onto glass substrates, bombarded, and then (partially) dissolved and loaded onto the filament of a mass spectrometer for analysis. This material was found to be depleted in the lighter isotopes, which indicates a corresponding light-isotope enrichment in the sputtered material . $\delta(^{24}\mathrm{Mg}/^{25}\mathrm{Mg})$ was observed to be as negative as $-10.3‰$ in the target, but quantitative information about the true size of the effect is difficult to extract from the data because the portions of film that were dissolved for analysis most probably contained some material of unaltered composition—this would tend to have diluted the the actual surface enrichment.

Several investigators have made isotope measurements of the third type above, in which the flux of sputtered ions at a fixed angle in the sputtering geometry was monitored as a function of bombarding fluence using SIMS. The first of these measurements was made by Shimizu *et al.* as part of a broader study of isotopic fractionation effects in secondary ion mass spectrometers [65]. They sputtered gold-coated targets of both Cu and Mo with 13.2 keV O^-, and examined the $^{63}Cu^+/^{65}Cu^+$

and $^{92}Mo^+/^{100}Mo^+$ ratios, respectively, for variation during the initial stages of sputtering. No significant change was observed for the Mo target, but the ratio for Cu decayed exponentially until a steady-state value was reached; $\delta_0(^{63}Cu^+/^{65}Cu^+)$ (the estimated enrichment at zero fluence with respect to the steady-state ratio) was found to be ~8‰. Insufficient information is provided to be able to ascertain actual bombarding fluences, however.

In contrast with this result for Cu, Okano *et al.* made similar measurements using 9–17 keV O^{2+} to sputter targets of Cu and also Ni, and found the $^{63}Cu^+/^{65}Cu^+$ and $^{58}Ni^+/^{60}Ni^+$ ratios to *increase* initially by ~13‰until steady-state conditions were reached [76]. The lowest fluences for which data were obtained were $> 10^{18}$ ions cm^{-2}, however, and there is some question about whether adequate measures were taken to avoid interference from other sources of instrumental fractionation. Thus, it may not be appropriate to compare these findings with those of Shimizu *et al.*

Two other quite recent investigations of the same type support this appraisal. In both of these experiments, incremental beam fluences as small as $\sim 10^{15}$ ions cm^{-2} were used to sputter various target materials, and in all cases surprisingly large light-isotope enrichments were observed initially in the sputtered-ion flux; the enhancements dropped to steady-state values after typical fluences of $\sim 10^{17}$ ions cm^{-2}. Gnaser *et al.* bombarded targets of $LiAlSi_2O_6$, LiF, TiO_2 (rutile), GaAs, and Mo with 14.5 keV O^- [77]. They found $\delta_0(^6Li^+/^7Li^+)$ to be ~53‰for both lithium-bearing targets; $\delta_0(^{92}Mo^+/^{100}Mo^+)$ to be 49‰(in contrast with the null observation of Shimizu *et al.*); $\delta_0(^{48}Ti^+/^{50}Ti^+)$ to be 37‰and $\delta_0(^{46}Ti^+/^{50}Ti^+)$ 63‰for the rutile target; and $\delta_0(^{69}Ga^+/^{71}Ga^+)$ to be 12‰for the GaAs target. Baumel *et al.* sputtered boron targets with 100 keV Ar^+ and Ne^+, and measured $\delta_0(^{10}B^+/^{11}B^+)$ values of 46‰and 52‰for the neon and argon bombardments, respectively [78].

This represents the extent of experimental measurements of isotopic effects in sputtering that have been reported to date. Although there is undoubtedly considerable variation in the quality of the existing data, along with a few possibly conflicting results, several general trends are apparent. The majority of the data

indicate that the lighter isotopes are ejected preferentially both as neutrals and ions in the very early stages of sputtering. This initial enrichment in the sputtered flux is seen to be diluted by secondary compositional changes in the target as bombardment continues, and is no longer apparent at bombarding fluences appreciably greater than 10^{17} ions cm^{-2}. The magnitude of the observed fractionation varies a great deal from experiment to experiment, even for similar targets (although this is not surprising in view of the variety of experimental conditions and techniques); in particular, fractionation observed in the recent secondary-ion experiments is much larger than any observed fractionation of sputtered neutrals. It is not apparent from these data whether such large enrichments should be observed for neutrals at correspondingly low bombarding fluences where the effect is still relatively undiluted, or whether the large ion fractionations are due in part to ionization processes and do not accurately reflect the size of the effect in the total sputtered flux. Another point is that, in the data of Russell *et al.* and Gnaser *et al.*, the magnitude of the fractionation does not appear to be strongly dependent on the matrix from which the isotopes are sputtered. Finally, definite angular variations have been observed in the enrichment of the sputtered flux; the lighter isotopes are found to be sputtered preferentially in directions close to the target normal, and this behavior persists even at very high bombarding fluences. Because none of the angular data were measured at very low fluences, it is not clear whether these variations are a primary consequence of the preferential ejection process, or arise instead from the secondary changes occurring in the target.

Resolution of the questions regarding the origin of the angular effects and the differences between the neutral and secondary-ion data is important to developing further our physical understanding of preferential sputtering. Existing analytic theories, notably those developed by Sigmund [26,70,79] and by Haff and coworkers [80-82], address only primary sputtering effects and should be compared with low-fluence data if possible. Both of these theories were developed from the linear cascade theory of sputtering, but make significantly different predictions about the origin and size of preferential effects. Sigmund's model predicts a light-isotope

enhancement in the sputtered flux that depends on the ratio of the isotope masses and the nature of the interatomic scattering cross sections in the collision cascade. The 'surface flux' model of Watson *et al.* [81] and Haff *et al.* [82], on the other hand, predicts isotopic enrichments that depend strongly on the matrix from which the isotopes are sputtered; in a two-isotope elemental target, the more abundant isotope should be preferentially sputtered. Whereas both of these theories predict preferential effects comparable in magnitude to those observed by Russell *et al.*, for example, neither can account for the size of the effects in the secondary-ion data of Gnaser *et al.* or Baumel *et al.* Also, because both of the theories rely on the assumption of an isotropic velocity distribution in the cascade, neither predicts any projectile dependence or angular dependence for preferential sputtering in the limit of zero fluence.

In contrast with this are the predictions of recent computer simulations of the sputtering of two-isotope elemental targets. Using a multiple-interaction code, Shapiro *et al.* simulated the sputtering of crystalline Cu targets bombarded by 5 keV Ar^+ ions [27,28]. The targets employed in the simulations included both natural Cu and pseudo-Cu, in which the isotopic mass difference was artificially large. In all cases, the light isotope was found to be sputtered preferentially with a strong angular dependence peaked in the direction of the target normal; furthermore, the magnitudes of the isotopic enrichments in the sputtered flux were comparable to those observed by Gnaser *et al.* and Baumel *et al.* In another set of simulations, Eckstein *et al.* used a binary-interaction computer code to model the sputtering of boron [83]. A simulation with 100 eV ^{4}He projectiles demonstrated enhanced sputtering of the light isotope with an angular dependence similar to that seen by Shapiro *et al.*, although less pronounced. Furthermore, simulations with projectiles of different masses and energies showed the overall isotopic enrichment to be dependent on these quantities. Projectiles of all masses with energies $\gtrsim$500 eV preferentially ejected the lighter isotope to a varying extent—at 2 keV, for example, Xe^+ produced a light-isotope enrichment of $\sim$30‰, half that produced by 2 keV He^+. At energies $\lesssim$500 eV, however, very heavy projectiles (Kr^+ and Xe^+) were

found to eject the *heavy* isotope preferentially.

In view of the discrepancies between the predictions of existing theories, results of computer simulations, and experimental data for the sputtering of isotopic mixtures, there is clearly a need for further investigation of this aspect of sputtering. The work described in what follows was intended to address some of the outstanding questions raised above. Experiments have been conducted to measure the neutral sputtering yield from a multi-isotopic target at significantly lower bombarding fluences than have previously been used, in order to resolve better the size of preferential effects in the limit of zero fluence and to look for the presence of angular effects at these low fluences. Artificial two-isotope targets of molybdenum have been bombarded with different projectiles to fluences as low as 10^{15} ions cm^{-2}; the resulting light-isotope enrichments have been found to be comparable for both sputtered neutrals and ions, and are considerably larger than predicted by theory.

4.2 Experimental Methods

The sputtering experiments were performed in an ion-pumped UHV chamber at the California Institute of Technology's 6 MV Tandem Van de Graaff accelerator facility. The chamber was located at the end of one of the main accelerator's beam lines; also situated near the end of this beam line was a small kV accelerator of in-house construction. Low-energy ion beams from the small accelerator could be injected into the primary beam line and hence into the chamber—these ions were used to induce the sputtering.

The configuration of kV accelerator, beam line, and chamber is shown schematically in Figure 4.1. The accelerator, which utilized a radio-frequency (RF) ion source, was mounted with its axis at right angles to the primary beam line; a doubly-focusing 90° sector magnet deflected beams from the accelerator towards the chamber, and at the same time momentum-analyzed the ions. Located between the magnet and the chamber were a pair of steering magnets and an Einzel lens for deflecting and focusing the ion beam on the target. The power supplies to the steering magnets were rastered during each bombardment to sweep the beam and

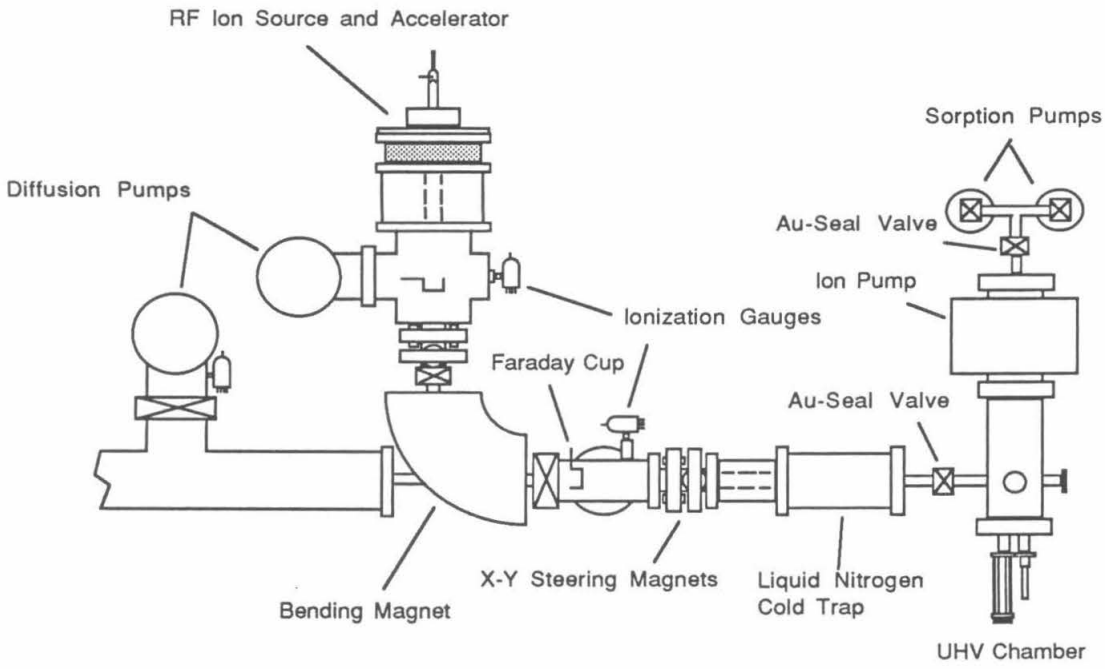

Figure 4.1 Configuration of the keV accelerator, vacuum system, ion optics, and target chamber used for these sputtering experiments.

ensure uniform irradiation of the sputtered area.

To provide differential pumping between the target chamber and the body of the accelerator, where the pressure was typically 2×10^{-6} Torr when the accelerator was operating, a diffusion pump was installed immediately downstream from the analyzing magnet; the pressure here was at most two or three times 10^{-7} Torr during operation. A horizontal in-line liquid-nitrogen-filled cold trap was located between this volume and the chamber to provide further isolation; this was sufficiently good that when the gold-seal valve to the chamber was opened (with no ion beam), the pressure in the chamber did not change.

Two different species of ions, argon and xenon, were used to sputter the targets in these experiments. For the reasons mentioned in Chapter 2, noble gas ions were used; these two particular species were selected to bracket the mass of the

molybdenum being sputtered. In addition to using projectiles with different masses, the projectile energy was varied as well. Although the accelerator was capable of producing up to 20 keV singly-ionized atoms, the analyzing magnet power supply could only produce current sufficient to bend 10 keV Xe^+. For this reason, beams of 5 and 10 keV Ar^+ and Xe^+ were used for most of the bombardments.

The apparatus used to hold the targets and collector foils was very similar to that used in the MCI experiments, and essentially the same equipment was used in the initial experiment of this investigation. Based on the results from this first trial, however, the apparatus was redesigned to optimize the measurements. The principal change made was to reduce the radius of the collector foil holder from 3.81 cm to 1.58 cm, the goal being to minimize the sputtering dose necessary to deposit a measurable amount of material on the collectors. Note that the material used for the collectors in these experiments was 0.13-mm-thick ultra-pure graphite sheet, which was both easier to handle than the Al foil used in the MCI experiments and offered the advantage of not contributing to the backscattering yield during the HIRBS analysis.

The semicircular vanes that permitted isolation of one collection region at a time (*cf.* Fig. 2.1) were incorporated into the clamps used to mount the targets in these experiments, so that each target had its own pair of vanes. This configuration was mechanically simpler than free-standing vanes, especially in the more confined geometry of the redesigned apparatus, and also reduced the possibility of problems associated with the resputtering of material initially deposited on these vanes, although this was not anticipated to be a significant factor in any of the measurements (*cf.* Appendix A).

Three collimators were mounted upstream from the collector foil holder in this setup. The first two defined the beam envelope, which was 5.77 mm in diameter at the target, as ascertained by examining a sputtered target with an optical comparator. These collimators were at ground potential; the third was biased at -600 V to suppress secondary electrons in the ion beam and coming from the target. Currents from the first pair and the third could be monitored when tuning the beam and

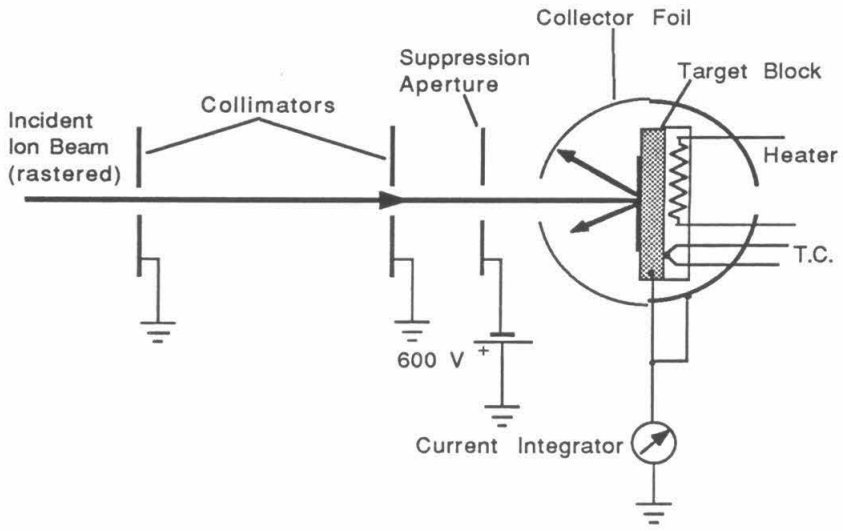

Figure 4.2 Schematic diagram of the sputtering apparatus, showing beam collimation and electron suppression.

while sputtering.

The targets sputtered were isotopically enriched, self-supporting, rolled polycrystalline molybdenum metal foils, approximately 5 mg cm^{-2} thick. The foils were manufactured by Oak Ridge National Laboratory from 98.27%-pure ^{92}Mo stock and 97.27%-pure ^{100}Mo stock; targets consisting of the ^{92}Mo stock, the ^{100}Mo stock, and a mixture of 50 atomic percent of each were used. Mo was selected as the target material because it is a relatively massive element (to facilitate HIRBS analysis) with a large range of stable isotopes, and is a common material that is not prohibitively expensive in isotopically-enriched form. The reason for using a target material containing two isotopes with a large relative mass different was two-fold: the size of any mass-related sputtering effects was expected to scale with the ratio of the two masses, and a large mass separation simplified analysis of the collector foils.

Except for the targets used in the initial measurement of sputtered neutrals and for the secondary ion measurement described below, all the target foils were etched

to remove any accumulated oxide layer before being loaded into the sputtering chamber. The etchant used was a 1:1 mixture of H_2O_2 and HCl, diluted with deionized water; a 1-2 min ultrasonic bath in this solution was followed by rinses in deionized water and isopropanol, and drying in warm air. The time elapsed between completion of this procedure and evacuation of the loaded vacuum chamber was typically ~ 30 min, during which period the targets were exposed to air.

After being evacuated, the chamber was baked for at least one day at $\sim 300°C$ to bring the base pressure at room temperature down to 1×10^{-9} Torr. Pressure was measured indirectly by means of the ion pump current, which is proportional to total pressure in the pump and for which standard calibration curves are available. After the chamber had cooled off, the target block heater was turned on and the targets were brought up to 150°C, where they were held for the duration of the experiment. In the setup used for this investigation, the thermocouple voltage was fed back to the heater controller to stabilize dynamically the target temperature.

During sputtering, the chamber pressure rose to between one and five times 10^{-8} Torr, depending on the intensity of the incident ion beam. Projectile fluxes ranged from $\sim 2.4 \times 10^{12}$ cm^{-2} s^{-1} for the 5 keV Xe^+ beam to $\sim 4.3 \times 10^{13}$ cm^{-2} s^{-1} for the 10 keV Ar^+ beam; at these intensities, Relation (2.1) was easily satisfied in all instances if one assumes the relevant pressure for calculating surface coverage to be closer to the base pressure than the actual pressure, following the arguments of §2.3. The only real concern about target cleanliness had to do with the surface contaminants present at the inception of sputtering.

With the exception of the initial experiment, the procedure followed in sputtering the various targets was to begin collecting sputtered material from the outset of bombardment, because the most interesting effects were anticipated to occur at low sputtering fluences. Each initially pristine target was sputtered in a series of consecutive bombardments of progressively larger doses, with a different collector region positioned in front of the target during each bombardment; the ion beam was interrupted for typically 15 to 20 s to make this change between irradiations. The sputtering doses were calculated to remove approximately one, two, three, and

10 monolayers of material in the bombardment progression, respectively. For the 10 keV Ar^+ irradiations, for example, incident fluences of 1.2×10^{15}, 2.4×10^{15}, 3.6×10^{15}, and 1.2×10^{16} ions cm^{-2} were used. These values were adjusted somewhat for the other ion beams in anticipation of different sputtering yields, and an additional low-fluence bombardment was carried out in each of the 5 keV irradiations. The uncertainty in current integration is estimated to be ~2%; this convolved with the uncertainty in bombarded area puts the uncertainty in average fluence estimation at ~3%.

Targets of the two-isotope material were sputtered in the above manner with 5 and 10 keV Ar^+ and Xe^+; the collector foils from these bombardments were analyzed using SIMS. The 10 keV Ar^+ irradiations of the two-isotope material actually were conducted twice; the second set of foils was analyzed using HIRBS. Additionally, the sequence of 10 keV Ar^+ irradiations was repeated with targets of both single-isotope materials; these foils were also analyzed using HIRBS and served as a check on the Mo sputtering behavior in the absence of mass effects. Several steady-state bombardments (*i.e.*, where collection was begun only after the target had already been sputtered with relatively large doses) were carried out on the single-isotope targets to test for possible variation in collection efficiency as a function of the density of collected material. The measurements made in the initial experiment (in which 20 keV Ar^+ projectiles were used) were also essentially steady-state measurements: the targets were sputter-cleaned before collection was begun, and typical bombarding fluences were 1.0×10^{17} ions cm^{-2}.

The HIRBS analysis of the various collector foils was performed using 6 MeV $^{16}O^{2+}$ ions and the same apparatus employed in the MCI experiments (*cf.* Figure 3.4 and Appendix B). The original intent was to analyze all of the collectors with HIRBS, but this was not realized because of complications associated with the distribution of the sputtered material at the collector surfaces. The backscattering spectra obtained from the graphite foils were found to exhibit very large tails on the low-energy side of the molybdenum peaks; these tails were much larger than those usually seen from metal collector foils. Figure 4.3 shows typical HIRBS spectra

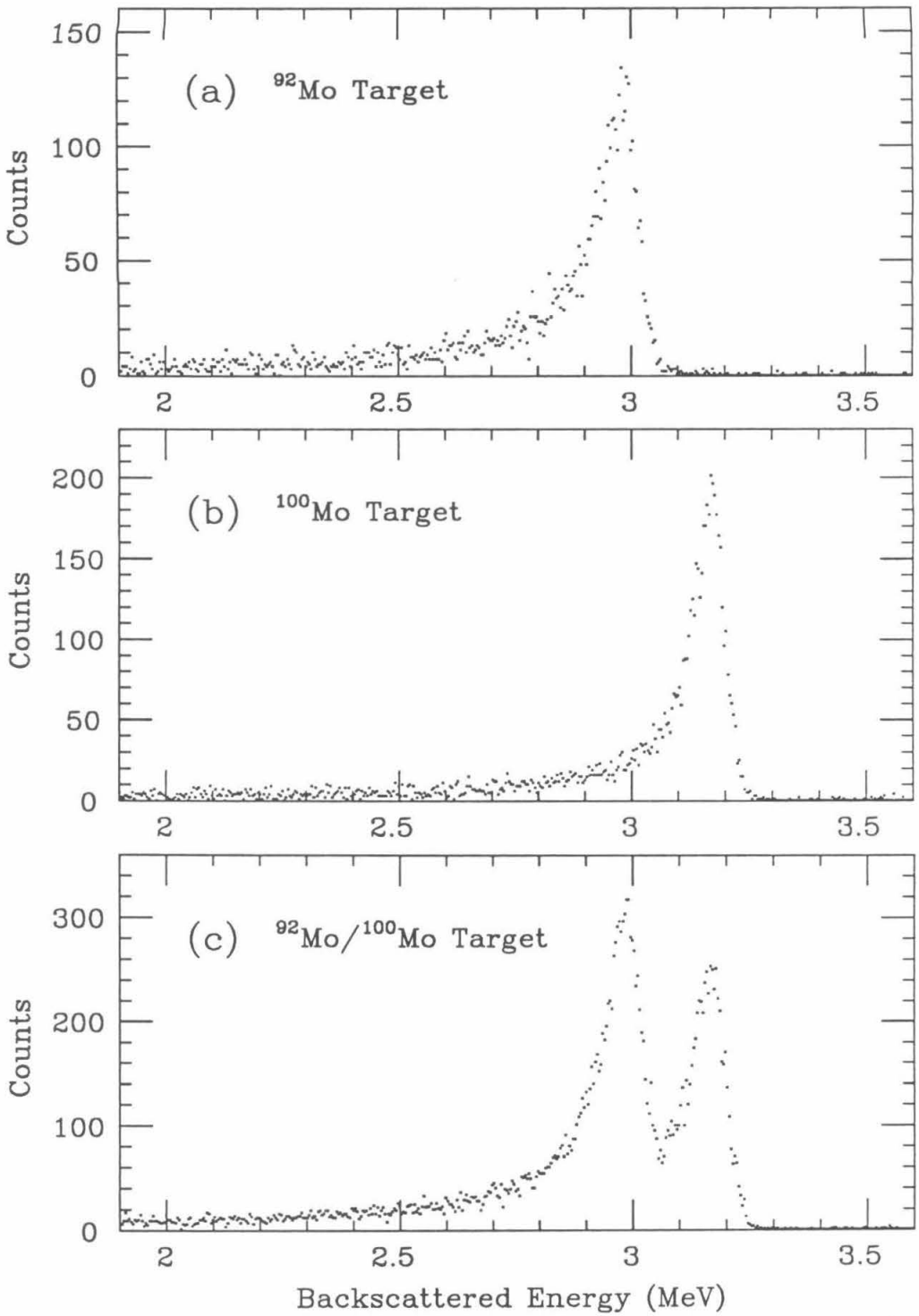

Figure 4.3 Representative spectra from the HIRBS analysis of the carbon collector foils. The spectrum in (a) is of material sputtered from a ^{92}Mo target; (b) is from a ^{100}Mo target; and (c) is from a ^{92}Mo/^{100}Mo target. Note the large tails on the low-energy sides of the peaks.

for the different targets sputtered. The tails were probably due to the molybdenum atoms either diffusing into the bulk carbon or migrating into deep pores or crevices and along grain boundaries at the foil surface. (The foils were comprised of micron-sized grains.) A third possibility, that the deposited molybdenum was agglomerating into droplets, was rejected because of the low densities of collected material at the foil surface: maximum coverages ranged from 2×10^{13} cm^{-2} for the low-dose sputtering bombardments to 5×10^{14} cm^{-2} for the highest-dose bombardments. [For a discussion of similar phenomena observed elsewhere, see Ref. 84.]

The presence of these large tails in the HIRBS spectra made it difficult to determine accurately the relative abundances of the two molybdenum isotopes on the collectors, and even the single-isotope HIRBS measurements were compromised to some extent. Rather than abandon the graphite collectors altogether, the foils were analyzed using SIMS, where it was found that relative changes in the isotopic abundances on the foils could be ascertained to a higher degree of accuracy ($\lesssim$0.3% standard deviation in most instances) than would have been possible even under the most favorable of circumstances with HIRBS (for which accuracies of less than 1% would have been difficult to achieve). The HIRBS analysis was still useful, however, for determining total absolute sputtering yields and the general shapes of the angular distributions of sputtered material. Analyzing doses for the HIRBS measurements ranged from 1.2×10^{16} to 1.2×10^{17} ions cm^{-2}.

The SIMS analysis was performed with the California Institute of Technology's PANURGE ion microprobe (a modified Cameca IMS-3f) [85], the layout of which is depicted schematically in Figure 4.4. In preparation for analysis, the collector foils were cut into segments small enough to be mounted on the microprobe's translatable sample stage; only half of each (presumably symmetric) collection region was prepared. Each segment to be analyzed was then loaded into the microprobe's target chamber, where it was sputtered with a beam of 14.5 keV O^- ions incident along a direction $\sim 30°$ from the sample normal. Positive secondary ions sputtered from the foil were accelerated through a 4.5 kV potential drop, focused, energy- and mass-analyzed, and counted by an electron multiplier device. Count rates were low

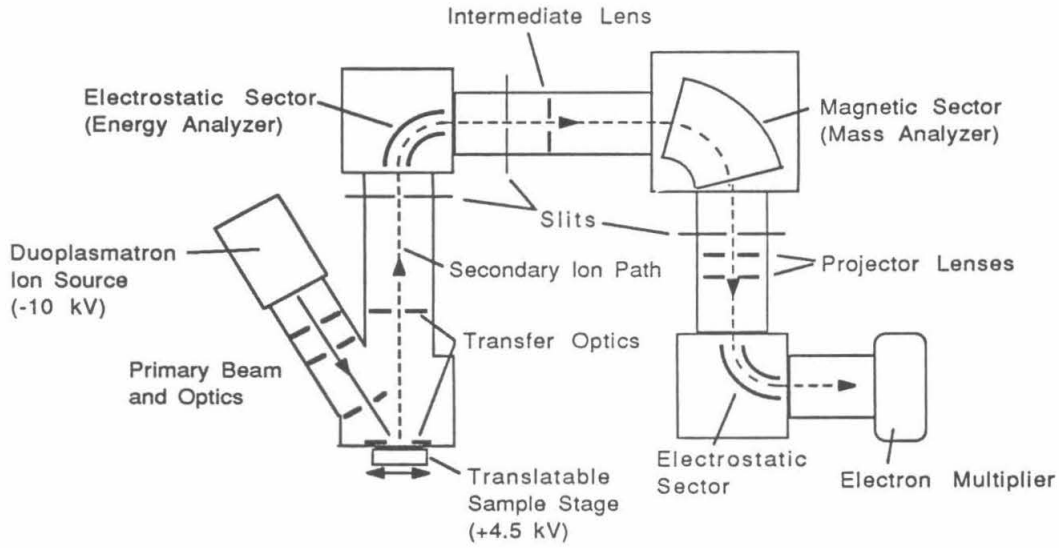

Figure 4.4 Schematic diagram of the PANURGE ion microprobe used for the SIMS analysis of the collector foils.

enough here that no dead-time correction was necessary for the acquired data.

The primary beam was focused to a diameter of several microns and rastered over an area of $\sim (100\,\mu\mathrm{m})^2$ on the foil, and secondary ions were accepted from a circular region $60\,\mu$m in diameter at the center of this bombarded area. Primary beam currents of 5–10 nA were used for the foil analysis.

The mass resolving power ($M/\Delta M$) of the instrument was set at ~ 500 for these measurements. This low resolution was acceptable for the analysis of the ^{92}Mo and ^{100}Mo isotopes because of the absence of any significant isobaric interferences; it was desirable because of the larger instrument acceptance and hence shorter analysis time than at higher resolving powers.

To measure the ^{92}Mo/^{100}Mo ratios on the foils, the mass analyzer was shifted rapidly back and forth between the two isotopes under automated field control, measuring half-heights as well as centroid height for each peak and recentering on the peaks as necessary every cycle. The ion signal was measured for 2 s at each

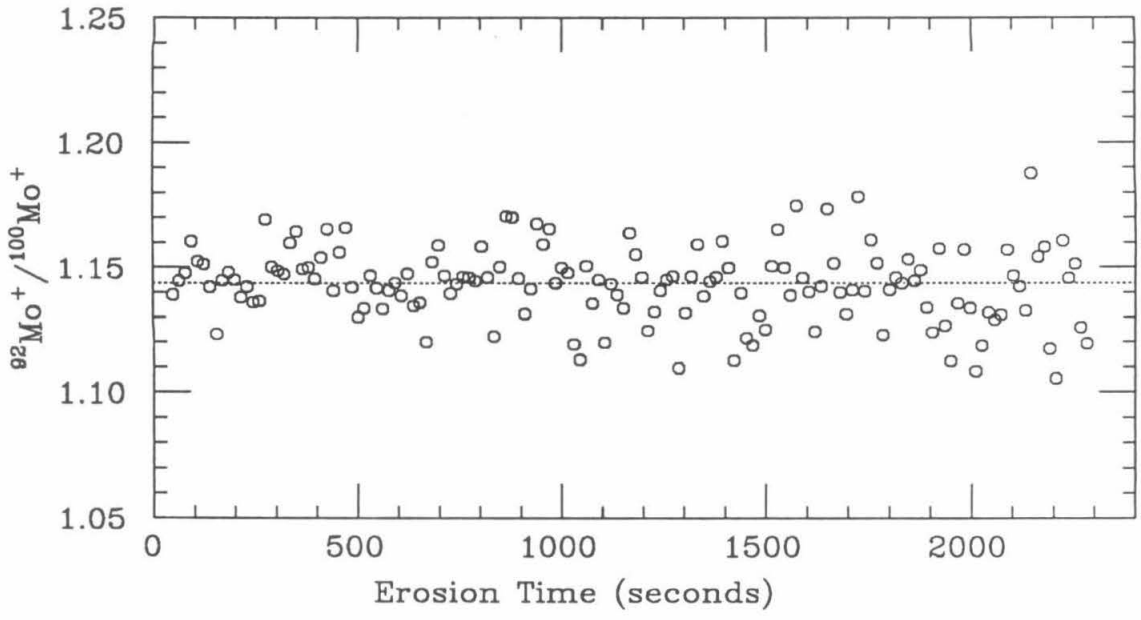

Figure 4.5 A typical set of interpolated isotope ratios obtained from the SIMS analysis at a single spot on the collector foil. The dotted line represents the weighted average of the points. The scatter in the data is consistent with their statistical uncertainty.

peak, and each cycle lasted for $\sim$ 15 s; 150 of these cycles were made in a typical measurement. Signal amplitude usually decayed by a factor of 2–3 over the course of such a measurement.

The ^{100}Mo signals obtained for all the cycles in a measurement were then linearly interpolated to determine the isotope ratio at the time each ^{92}Mo peak was recorded. Figure 4.5 shows a representative set of ratios calculated by this procedure. Each set of ratios was averaged, usually after discarding the first few points (where the the signal was changing most rapidly and the interpolation was poorest) to obtain a value for the isotope ratio at the corresponding location on the foil. In regions where the density of collected material was very low, several points at the same polar angle in the sputtering geometry were analyzed and the isotope ratios averaged to improve statistical certainty.

There were several concerns about the proper interpretation of the isotope ratios obtained in the above manner. First, isotopic fractionation is a phenomenon

inherent to SIMS that arises not only from the types of kinetic sputtering effects being studied in this investigation, but also from the ionization process itself [65-68]. Thus, the absolute values obtained for the $^{92}Mo/^{100}Mo$ isotope ratios on the collector foils certainly differed from the true values; however, such offsets are not a problem so long as only relative comparisons are made between measurements obtained under identical conditions, for which any fractionation effects are presumably systematic. A possible source of error in these measurements was associated with the reproducibility of sample positioning in the surface normal direction; because the primary beam was obliquely incident, variation in this position could change the relation between the primary beam and the secondary-ion optical axis, which is known to affect instrument fractionation [65]. As a check on this, the same region on one foil was reanalyzed several times during the course of the measurements. The corresponding isotope ratio was found to be reproducible with a standard deviation of $\sim 0.2\%$; this uncertainty was folded in with the statistical uncertainty for all the ratios.

Preferential sputtering of the lighter isotope during the SIMS analysis was not anticipated to be a problem because of the low density of collected material on the foils—coverages were less than half a monolayer in all cases, so interaction between the two isotopes during analysis should have been minimal. Another concern was that, if the large tails in the HIRBS spectra were due to diffusion of the molybdenum atoms into the bulk carbon, the isotope ratio might not be constant as a function of depth beneath the foil surface because of the mass dependence of the diffusion rate constants. However, no systematic trends were observed in the isotope ratio as a function of analysis time during the measurements.

The microprobe was used to perform one other measurement in addition to the foil analysis. A target of the two-isotope molybdenum material was bombarded directly with the microprobe to determine the ratio of secondary ions sputtered as a function of projectile dose. To make the measurement, the same 14.5 keV $^{16}O^+$ primary ion beam was used to sputter the sample, but at a reduced current of ~ 0.2 nA. (Note that this bombardment differed from the other sputtering bombardments

as discussed in §2.4 in several respects: a reactive atomic species was used for the projectile; the ion beam was not momentum-analyzed; and it was not normally incident on the target.) At the instrument settings used, most secondary ions sputtered into directions within $\sim 15°$ of the target normal were accepted into the spectrometer. The time to cycle between the two isotopes was reduced to 4.1 s, which was equivalent to a sputtering fluence of $\sim 5 \times 10^{13}$ ions cm^{-2} per cycle; the first cycle was started after the target had been bombarded with $\sim 6 \times 10^{14}$ ions cm^{-2}. Note that the primary ion beam current could not be measured directly on the target, but was determined by deflecting the beam into an unsuppressed Faraday cup; the above fluence estimates are therefore accurate to ~15%. Also, the pressure in the sample chamber during the bombardment was $\sim 5 \times 10^{-8}$ Torr.

4.3 Results

For the majority of the two-isotope collector foils, SIMS was used to determine the ^{92}Mo/^{100}Mo ratio at positions corresponding to only one or two different angles in the sputtering geometry. All of the foils were analyzed at an angle close to the target normal, and a select few were also analyzed at an angle far from the target normal. This approach was taken to determine the variation of the isotope ratio in the normal direction as a function of bombarding fluence, and simply to bracket the variation of the ratio with respect to sputtering angle.

The results from the SIMS analysis have been compiled in Table 4.1. Enhancements in the sputtered ^{92}Mo/^{100}Mo ratio were calculated according to Equation (4.1), where an isotope ratio measured for steady-state sputtering conditions was used for R_{ij}^{STD}. As alluded to in the preceding section, it was necessary to use a measured value for R_{ij}^{STD} rather than the true target isotope ratio because of instrumental fractionation introduced in the SIMS analysis. For the neutral data, the steady-state value was taken to be the smallest ratio (1.133) measured in the normal direction on any of the foils—this happened to be from the high-fluence 5 keV Xe^+ bombardment, which also represented the collection made after the greatest amount of material had been sputtered away from any of the targets. For

Table 4.1 Measured enhancement of the sputtered $^{92}Mo/^{100}Mo$ ratio.

Projectile	Fluence Range ($\times 10^{15}$ ions cm^{-2})	Angle[a] (degrees)	$\delta(^{92}Mo/^{100}Mo)$[b] (permil)
10 keV Ar^+	0–1.21	17	63.7 ± 5.6
	1.21–3.65	17	27.4 ± 3.6
	3.65–7.31	17	14.1 ± 3.6
	7.31–19.45	17	2.0 ± 3.2
	"	74	-8.9 ± 3.4
5 keV Ar^+	0–1.22	17	70.7 ± 6.4
	2.43–4.86	17	21.0 ± 3.7
	"	74	15.6 ± 5.2
	4.86–8.50	17	9.4 ± 3.6
	8.50–20.63	17	1.3 ± 3.1
	"	74	-14.1 ± 3.5
10 keV Xe^+	0–0.61	17	46.7 ± 4.9
	0.61–1.82	17	30.2 ± 3.7
	1.82–3.66	17	24.0 ± 3.7
	3.66–9.74	17	16.3 ± 3.0
	"	74	-9.2 ± 3.7
5 keV Xe^+	0–0.61	17	70.9 ± 6.5
	0.61–1.82	17	40.4 ± 3.7
	"	74	19.1 ± 6.3
	1.82–4.29	17	32.3 ± 3.7
	"	74	10.9 ± 4.7
	4.29–7.93	17	18.6 ± 3.4
	7.93–20.05	17	0.0 ± 3.0
	"	74	-28.9 ± 3.4
14.5 keV O^-	$\gtrsim 1$	$\lesssim 15$[c]	$\lesssim 51 \pm 5$[d]

a. Polar angle in the sputtering geometry, measured from the target normal.

b. Average enhancement over the indicated fluence range, calculated with respect to the steady-state isotope ratio at angles close to the target normal. Data are for sputtered neutrals unless otherwise indicated. Errors shown are $\pm 2\sigma$, and do not include the uncertainty in the normalization factor.

c. This represents the acceptance half-angle of the secondary ion mass spectrometer.

d. Enhancement in the ratio of sputtered secondary ions, $\delta(^{92}Mo^+/^{100}Mo^+)$.

the secondary ion data, the steady-state value used was the isotope ratio (1.143) measured after a fluence of $\sim 2 \times 10^{16}$ O^- ions cm^{-2}, by which point the ratio had ceased to change significantly. Two comments should be made about these choices for R_{ij}^{STD}. First, it is possible that the isotope ratios had not yet completely stabilized at the bombarding fluences for which the above values were determined, so that they are actually larger than the true values; this would mean that the calculated light-isotope enrichments in Table 4.1 are underestimated, a conservative error. Second, the steady-state isotope ratio for material sputtered into normal directions in these experiments was larger than the ratio for the total sputtered flux because of the observed angular variations; hence, the enrichments quoted in the table are again smaller (or more negative, in the case of some of the oblique points) than they would be if strictly correct values were used for R_{ij}^{STD}—this should be kept in mind when comparing these data with the results from other experiments and computer simulations.

Also listed in Table 4.1 are the fluence ranges over which the targets were bombarded for the various collections; the corresponding enhancements are actually averages over these ranges. To facilitate comparisons among the data for the different projectiles, the results from the HIRBS analysis were used to convert these fluence ranges into eroded depths (actually, numbers of Mo atoms sputtered per unit area); the details of the conversion are discussed later in this section. The converted data for neutrals sputtered into normal directions are plotted in Figures 4.6(a) and (b). The secondary ion data are plotted in Figure 4.7. Note that the error bars shown in these and all subsequent plots in this section are $\pm 2\sigma$.

Examination of the data in Table 4.1 and Figures 4.6 and 4.7 reveals qualitatively similar behavior of the isotope ratio as a function of bombarding fluence (or eroded depth) for all the projectiles. The sputtered flux was strongly enriched (by up to 70‰in normal ejection directions) in the initial stages of sputtering for both neutrals and secondary ions, and decayed approximately exponentially to a steady-state composition; the characteristic 'decay length' was typically a few times 10^{15} sputtered atoms. Within the experimental uncertainty, the data for both energies

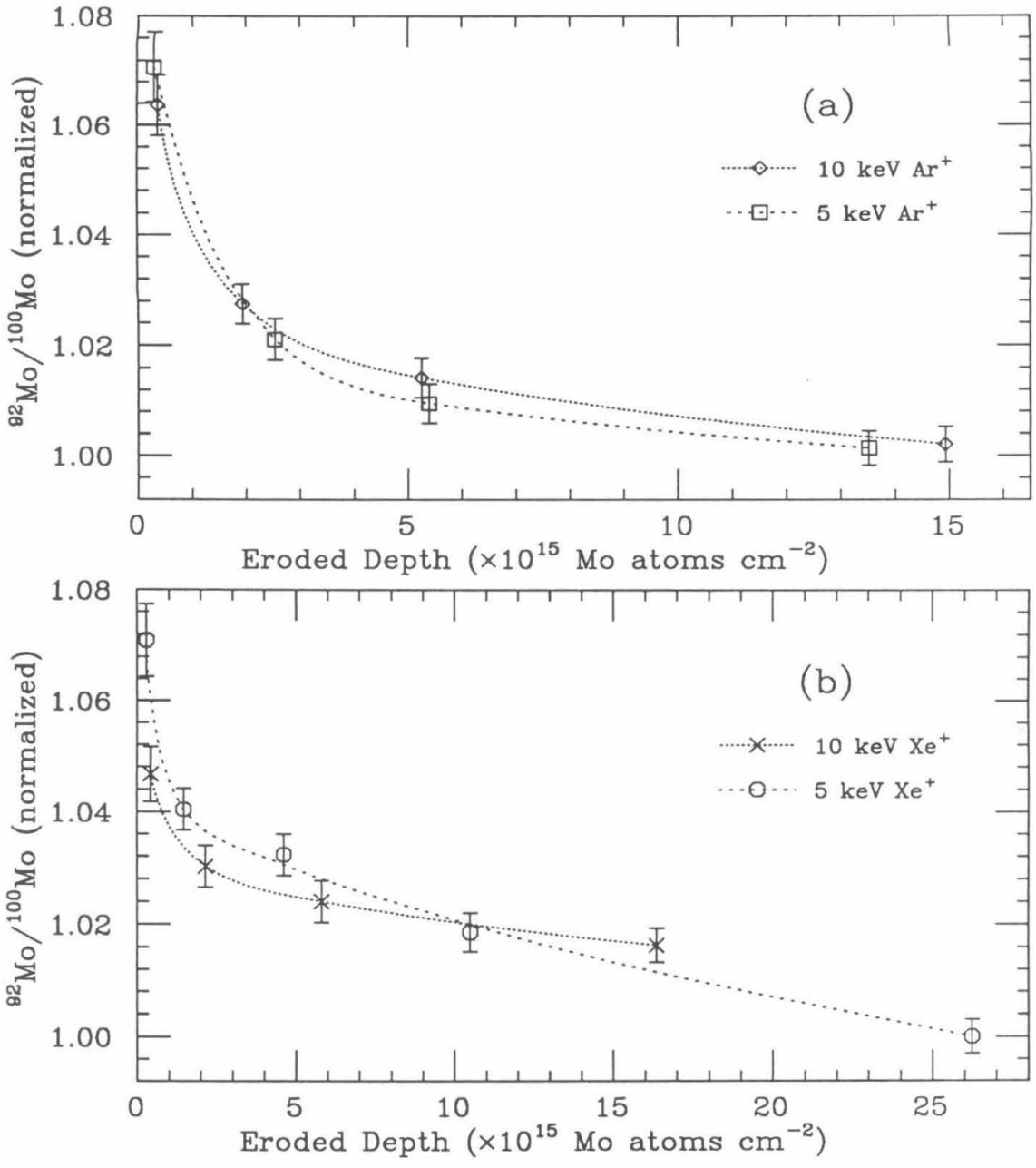

Figure 4.6 The normalized $^{92}Mo/^{100}Mo$ ratio for neutrals sputtered into directions close to the target normal, plotted as a function of the amount of Mo eroded from the target for (a) 5 and 10 keV Ar^+ projectiles, and (b) 5 and 10 keV Xe^+ projectiles. Each data point represents an average ratio over a sputtered range; for convenience of presentation, the points have been plotted at the centers of the corresponding ranges. The dotted lines joining the data points are to guide the eye. Note that the error bar on the point in the lower right corner of (b) represents the uncertainty ($\pm 2\sigma$) in the normalization factor.

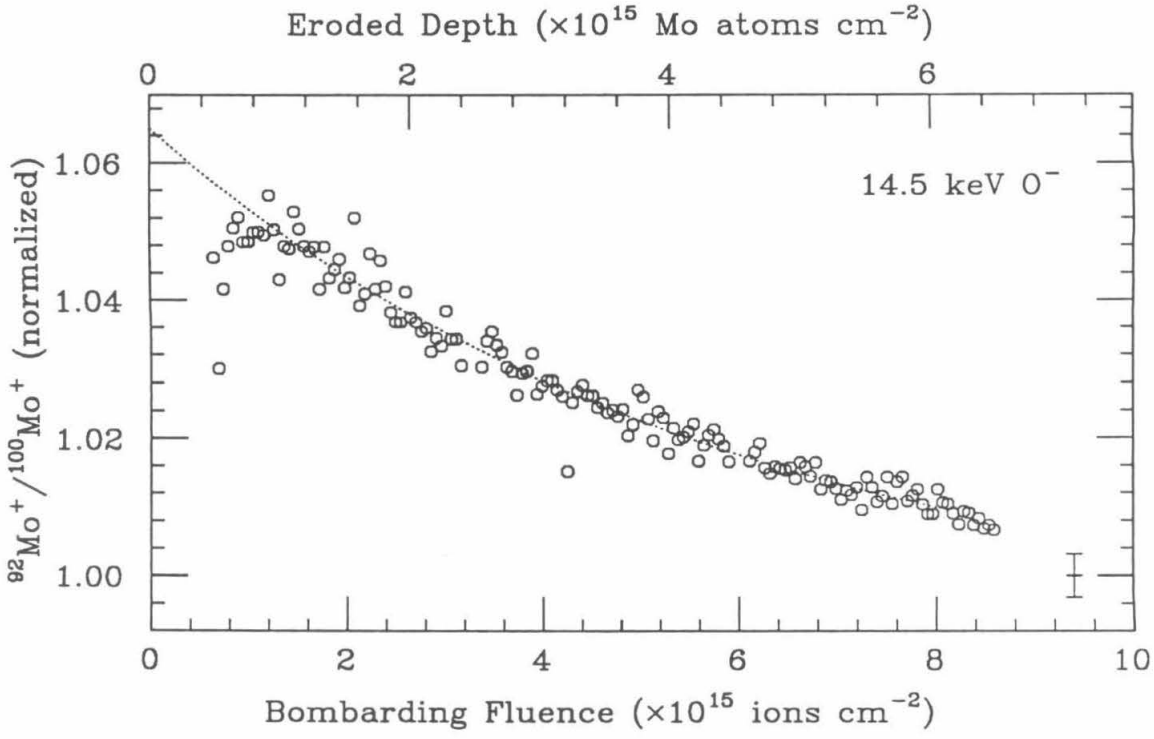

Figure 4.7 The normalized $^{92}Mo^+/^{100}Mo^+$ ratio for secondary ions sputtered from a Mo target into directions within $\sim 15°$ of the target normal, plotted versus the bombarding fluence of 14.5 keV O^- ions. The upper scale is based on a calculated value for the sputtering yield of 0.76. The dotted line is a least-squares fit (excluding the first few points) to a function of the form $y(x) = 1 + A\exp(-Bx)$. The error bar in the lower right corner represents the uncertainty in the normalization factor.

of Ar^+ fall along identical curves; these data and the secondary ion data for O^- most closely exhibit the exponential decay. The Xe^+ data do not fit this description quite so well, initially falling off quite rapidly with bombarding fluence, and then changing to a more gradual, almost linear descent towards steady-state with increasing fluence. The initial enrichment for 10 keV Xe^+ is noticeably smaller than for the other cases; also, the subsequent approach towards steady state appears to be considerably slower here than for the other bombardments.

Of principal interest was the magnitude of the light-isotope enhancement in the limit of zero bombarding fluence. To estimate this quantity δ_0 from the neutral data, the first two points from each data set were used to extrapolate linearly back

Table 4.2 Estimated enhancement of the sputtered $^{92}Mo/^{100}Mo$ ratio in the limit of zero fluence.

Projectile	$\delta_0(^{92}Mo/^{100}Mo)^a$ (permil)	m^b
10 keV Ar^+	72.6 ± 7.9	0.42 ± 0.04
5 keV Ar^+	77.6 ± 8.1	0.45 ± 0.04
10 keV Xe^+	50.8 ± 7.0	0.30 ± 0.04
5 keV Xe^+	78.5 ± 8.9	0.45 ± 0.05
14.5 keV O^-	65.0 ± 8.3	0.38 ± 0.05

a. Calculated by extrapolating the measured enhancements to zero fluence. See text. Errors shown are $\pm 2\sigma$.

b. Calculated from Equation (4.3). Errors shown are $\pm 2\sigma$.

to zero fluence (actually, back to zero sputtered depth, although this is essentially the same thing—see below); the results are presented in Table 4.2. Note that this method of estimating δ_0 is relatively conservative because it ignores the apparent nonlinearity in the data as a function of bombarding fluence. For the secondary ion data, a different approach was taken: the enrichment data were fit quite well with a function of the form

$$\delta(x) = \delta_0 \exp(-Bx), \tag{4.2}$$

where x is the bombarding fluence; δ_0 was determined from the fit in this case. For reasons to be discussed in §4.4, Table 4.2 also gives the exponent m calculated for each value of δ_0 from the relation

$$\delta_0 = \left[(M_2/M_1)^{2m} - 1\right] \times 1000, \tag{4.3}$$

where M_1 and M_2 are the masses of ^{92}Mo and ^{100}Mo, respectively.

The SIMS data are presented as a function of emission angle in the sputtering geometry in Figures 4.8(a) and (b) and Figure 4.9. All the data pairs plotted in Figure 4.8 indicate a light-isotope enrichment in emission directions close to the target normal as compared to directions far from the normal, but for the lowest-fluence 5 keV Ar^+ data this difference is not statistically significant. The 5 keV Xe^+ data,

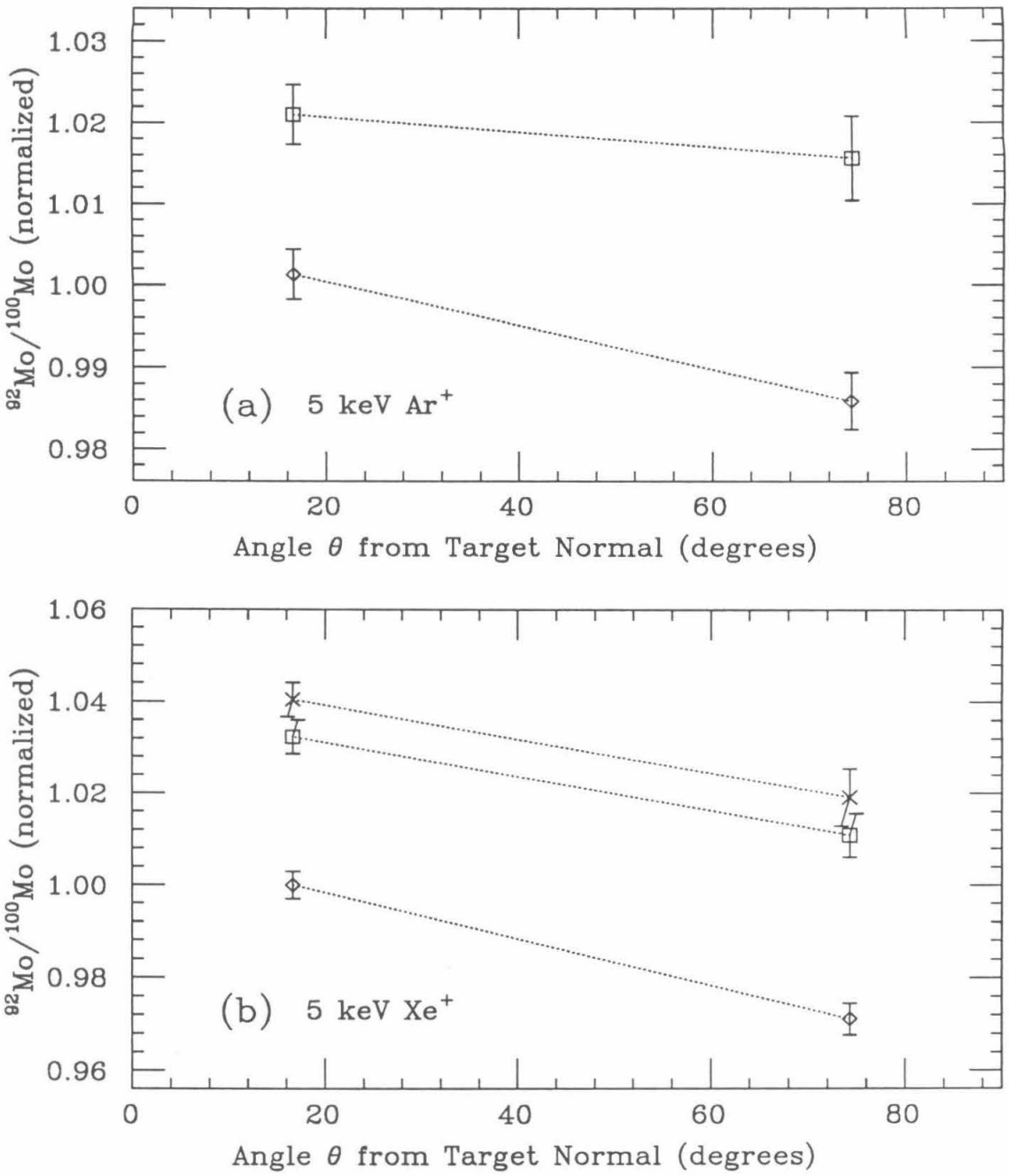

Figure 4.8 The isotope ratio of sputtered material (normalized to the steady-state value in the normal direction) plotted versus angle of emission (a) for 5 keV Ar^+ after eroding $\sim 2.5\times10^{15}$ (□) and $\sim 1.4\times10^{16}$ (◇) Mo atoms cm^{-2}; and (b) for 5 keV Xe^+ after eroding $\sim 1.5\times10^{15}$ (×), $\sim 4.6\times10^{15}$ (□), and $\sim 2.6\times10^{16}$ (◇) Mo atoms cm^{-2}. The eroded depths quoted are median values for the sputtered ranges corresponding to the different collections.

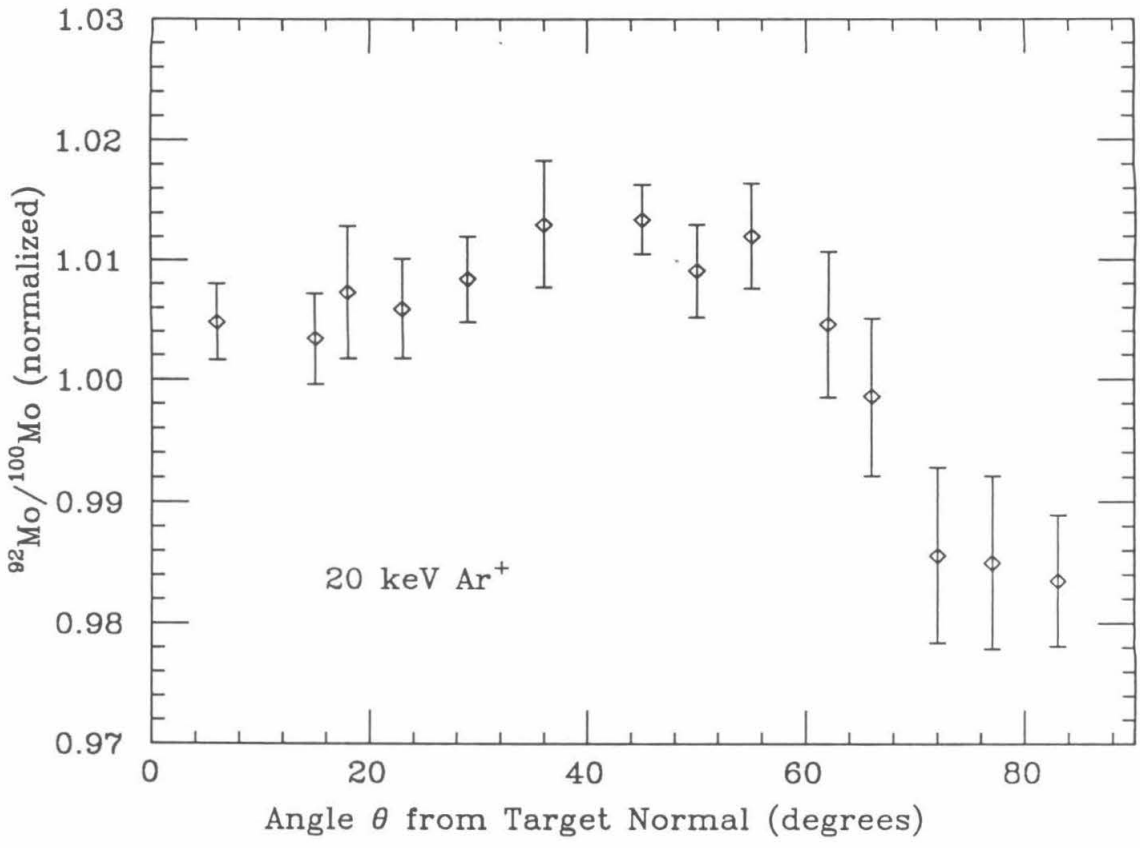

Figure 4.9 The isotope ratio of the sputtered flux plotted as a function of emission angle for steady-state conditions. These data were from a 20 keV Ar^+ bombardment over a fluence range of 2×10^{16} to 1.2×10^{17} ions cm^{-2}. Note that these data are normalized differently than the data in the preceding figures: the normalization factor was calculated assuming zero net enrichment in the total sputtered flux, and that the isotope ratio in the target was 1:1.

however, *do* exhibit a statistically significant relative enrichment ($\sim 20‰$) at the lowest bombarding fluence (which extended from 0 to 6×10^{14} ions cm^{-2}). The development of secondary effects in the angular dependence of the isotope ratio is also readily apparent in Figure 4.8; the relative difference between enrichments at normal and oblique angles is seen to increase with increasing sputtering fluence. Figure 4.9 shows a more complete set of angular data obtained from the high-fluence 20 keV Ar^+ bombardment in the initial experiment. The light-isotope enrichment here is actually higher at intermediate emission angles (30°–60°) than at angles closer to

the target normal; this may be due in part to bombardment-induced texturing of the surface, or to the development of surface topography during sputtering and the corresponding mixing of angles in the collection geometry,(*cf.* below and Appendix C).

The data from the HIRBS analysis of the collector foils were used primarily to determine total molybdenum sputtering yields, which in turn were used as mentioned above to calculate the eroded depths corresponding to the various isotope ratios measured with SIMS. The analysis of the collectors for the two single-isotope targets revealed nearly identical sputtering behavior—the shapes of the differential angular sputtering yields and the total yields were very similar. The angular distributions for the progression of 10 keV Ar^+ bombardments of ^{92}Mo are shown in Figure 4.10; these are also representative of the corresponding distributions obtained for the ^{100}Mo target. The distributions from the three low-fluence bombardments of both targets all exhibited relatively smooth "under-cosine" shapes; when fit with functions of the form $dY/d\Omega = A\cos^B\theta$, B was generally found to be 0.8–0.85. As can be seen for example in Figure 4.10, however, the distributions from the high-fluence bombardments deviated significantly from a smooth $\cos^B\theta$ shape, and the same was seen to be true for the high-fluence distribution from the two-isotope target. This is presumed to be a consequence of the development of microtopography or texturing at the surfaces of the polycrystalline metal targets [32,49], and is probably correlated with the angular dependence of the isotope ratio shown in Figure 4.9.

The most interesting information gained from the HIRBS analysis concerned the dependence of the total molybdenum sputtering yield on the bombarding fluence. (Total yields were calculated from the low-fluence angular distributions in the same manner as described in §3.3, but in the high-fluence cases where the distributions were not fit well with a power of $\cos\theta$, yields were calculated by simply taking a weighted sum over the angular data.) For the lowest-fluence bombardments, the total yield was found to be about half its steady-state value Y_{ss}, and was seen to grow along a decaying exponential curve towards Y_{ss} with increasing fluence.

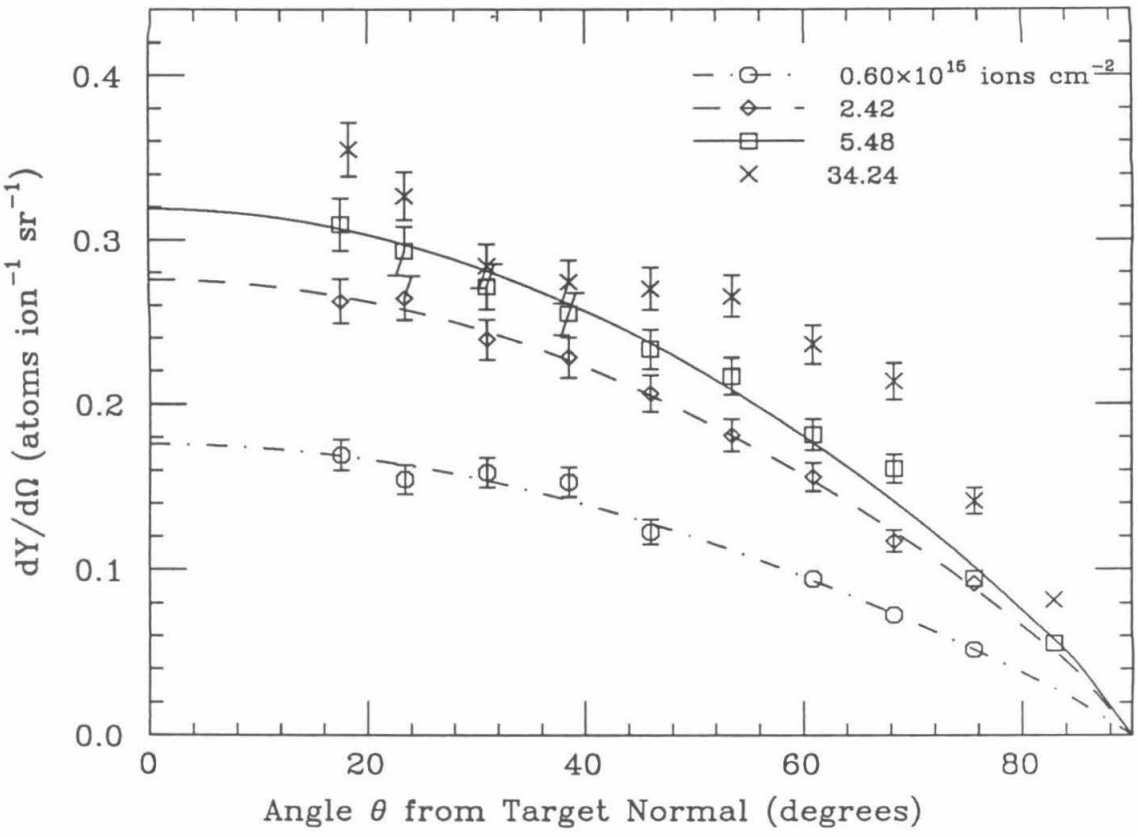

Figure 4.10 The differential angular sputtering yield from a ^{92}Mo target sputtered by 10 keV Ar^+, plotted for several different bombarding fluences. The values in the upper right of the figure are the median fluences for the various bombardments; the actual fluence ranges were 0–1.2, 1.2–3.6, 3.6–7.3, and 31.2–37.3×10^{15} ions cm^{-2}. The three lower-fluence distributions are shown with fitted functions of the form $A\cos^B\theta$; B is 0.88 for the lowest-fluence data, and 0.82 for the other curves. The deviation of the high-fluence distribution from this general shape is probably due to the development of surface topography or texturing.

This behavior was strikingly similar to that of the light-isotope enrichment in the sputtered flux as it dropped to its steady-state value with increasing fluence. The correlation between the two phenomena is illustrated in Figure 4.11; implications of this observation are discussed in the next section.

Rather than simply using the steady-state sputtering yields determined with HIRBS to convert bombarding fluences into the corresponding eroded depths for the SIMS data, the fluence dependence of the sputtering yield was also taken into ac-

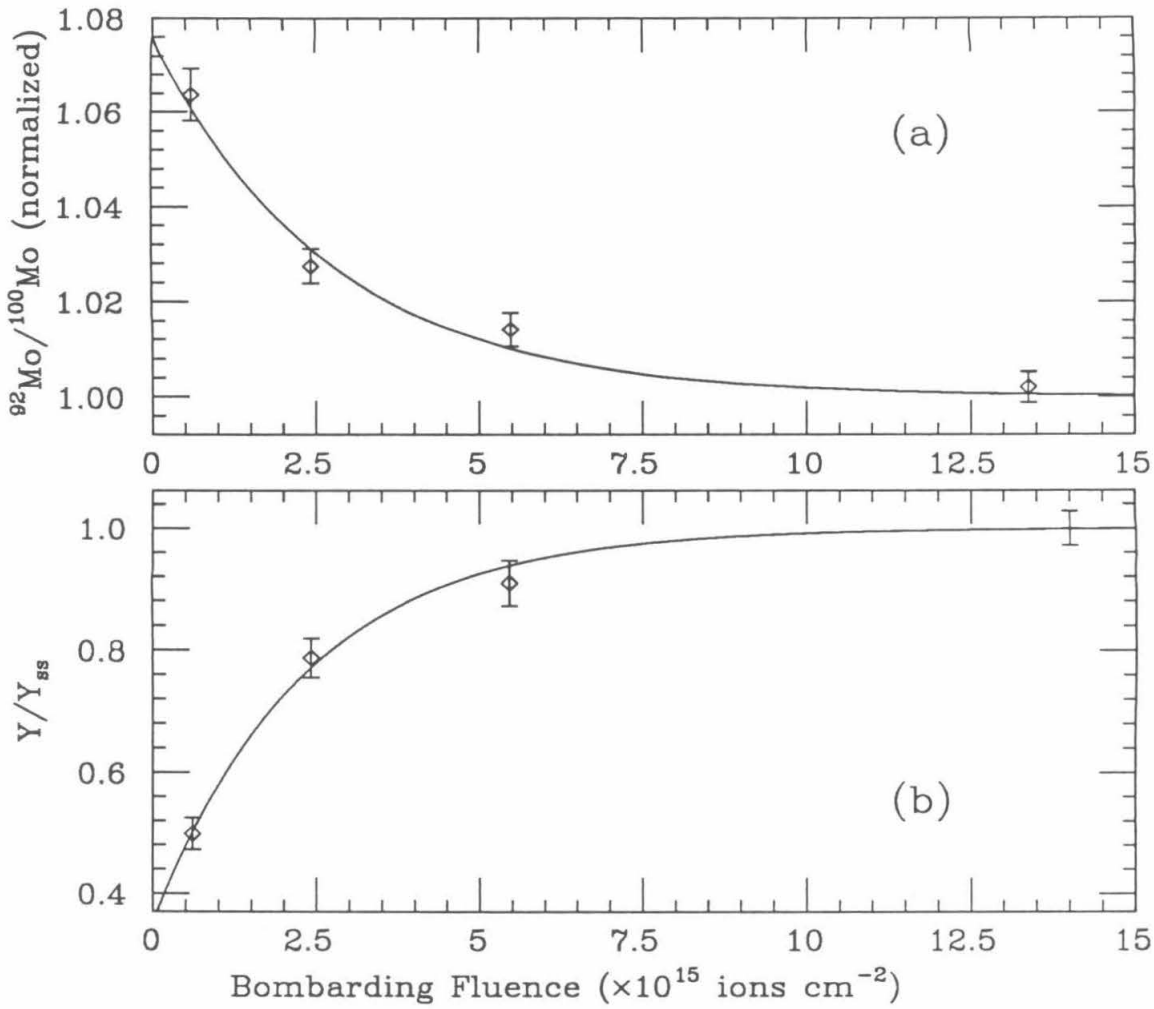

Figure 4.11 A comparison of (a) the fluence dependence of the sputtered isotope ratio determined with SIMS and (b) the fluence dependence of the total molybdenum sputtering yield (normalized to the steady-state value Y_{ss}) determined with HIRBS. Both sets of data are for 10 keV Ar^+ projectiles (although the HIRBS data are actually averages of the data obtained from the two single-isotope targets), and are scaled to demonstrate the correlation between the two quantities. The solid lines are least-square fits to decaying exponentials; 'decay lengths' determined from the from the fits were nearly identical.

count in this conversion. The conversion was based on the HIRBS data from the 10 keV Ar^+ bombardments of the single-isotope targets, for which the most extensive and accurate analyses were performed—these two sets of yields were averaged to approximate the corresponding yields from a two-isotope target. (As pointed out

above, the data were very similar.) Because measurements were only made for 10 keV Ar^+ bombardment, it was necessary to make the following assumption about the observed sputtering behavior in order to be able to extrapolate to the other bombardments. The initially low yield was presumed to be associated with the presence of a modified layer at the surface of the targets; as this layer was sputtered away, the yield increased to its steady-state value. Based on this presumption, it was assumed that the rate at which the yield approached steady-state would depend on how quickly the surface layer was removed, and hence on the sputtering yield itself. This assumption was incorporated into the function to which the yield data were fit, given by

$$Y(x) = Y_{ss}\left[1 + A\exp(-BY_{ss}x)\right] \tag{4.4}$$

where x is the bombarding fluence, Y_{ss} is the steady-state yield, and A and B are fit parameters. The data and fitted function are shown in Figure 4.11(b). Once A and B were determined, Equation (4.4) could be integrated after inserting an appropriate value for Y_{ss} to convert cumulative bombarding fluences into cumulative sputtering yields of molybdenum for each of the projectiles. Y_{ss} was determined from the HIRBS analysis for the 10 keV Ar^+ and Xe^+ projectiles (for which values of 1.25 and 2.71 were measured, respectively); these values were used in conjunction with linear cascade theory (to determine to appropriate energy scaling factors) to estimate Y_{ss} for the 5 keV projectiles.

The conversion procedure is not particularly precise in view of the various uncertainties in the HIRBS data, the fitted function, and the values used for Y_{ss}, and may have introduced absolute uncertainties as large as ~10% (mainly due to the last factor) into the converted values for the various projectiles. However, the *relative* uncertainty introduced for points in the same projectile data set should be no more than a few percent. In practice, the conversion was found not to alter appreciably the relative positioning of the data within each set plotted in Figures 48(a) and (b), and the estimated values for δ_0 were not significantly affected.

One final result from the HIRBS analysis regards the check made on the relative

sticking probabilities for the two molybdenum isotopes on the carbon collectors. This was a very simple test, in which the measured densities of material collected from a single-isotope target were compared for two steady-state bombardments, one twice as long as the other. If the densities failed to scale uniformly at all angles with the bombarding fluence, significant variations in the sticking probability as a function of surface coverage might be indicated. This type of behavior could account for part, if not all, of the fractionation effects observed on the foils because of the varying coverages involved. Within experimental uncertainty, however, no variation was apparent for either isotope in the test. Because of the somewhat limited accuracy of the measurements, this does not by itself prove that there are no variations on the order of a few percent in the sticking probabilities. However, the general consistency of the data, including those from the secondary ion measurement, indicate that the observed isotopic fractionations are most probably real and are not artifacts of the collector method employed.

4.4 Discussion

A recapitulation of the principal features of the sputtering behavior observed in these experiments is appropriate at this point. The light ^{92}Mo isotope was seen to be sputtered preferentially from the two-isotope targets in the early stages of bombardment, to an extent nearly as large as the inverse mass ratio M_2/M_1 (M_2 and M_1 being the masses of ^{100}Mo and ^{92}Mo, respectively); this was true for both the ejected neutral atoms and the much smaller fraction of secondary ions. There is some evidence for an angular dependence in the fractionation even from the outset of sputtering, at least for that induced by Xe^+ projectiles, with the light-isotope enrichment being strongest in ejection directions close to the target normal. All of these effects were observed to change with increasing projectile fluence: the light-isotope enhancement decayed approximately exponentially to a steady-state value; and the relative difference between the enrichments at angles close to and far from the target normal increased at the same time. In conjunction with these changes, the total sputtering yield of Mo atoms was seen to increase to a steady-state value

in approximately the same manner, indicating that the above effects may have been related in some way to the presence of a modified target surface layer at the inception of sputtering. At large projectile fluences, evidence for the development of surface structural modification (*e.g.*, increasing roughness) was seen in the angular distributions of sputtered material.

Before discussing any other aspect of the various results, it is necessary to address the implications of the correlation between the total sputtering yield and the fractionation behavior. The initially low sputtering yield was presumably due to the presence of atomic species other than Mo at the target surface, either as an adsorbed layer of gas molecules on top of the Mo or as atoms chemically incorporated into the Mo matrix at the surface, or perhaps some combination of both. One cannot readily distinguish the two possibilities on the basis of the fluence dependence of the total Mo sputtering yield alone; interpretation of the yield-versus-fluence as a depth profile of the undisturbed surface could be complicated by the recoil implantation of impurities, particularly in the first case above. The angular distribution of sputtered Mo was seen not to change significantly with increasing fluence in the early stages of bombardment (*cf.* Figure 4.10), however, which is more consistent with the second possibility of an impurity integrated with the Mo at the surface. If the contaminant(s) responsible for the reduced yield were in a segregated layer covering the Mo initially, one would expect to see a significantly sharper angular distribution for the lowest-fluence bombardment (because a larger fraction of Mo atoms would have come from beneath the surface monolayer) than for subsequent collections.

The tentative conclusion that the surface contamination was probably incorporated into the Mo matrix rather than lying on top of it is consistent with the anticipation of a surface oxide layer. As mentioned in §2.3, oxygen binds strongly enough to Mo to displace other adsorbed gas molecules; furthermore, O_2 will dissociate on adsorption. Oxygen atoms in this chemisorbed phase can subsequently undergo a chemical change of state to become incorporated in a surface oxide structure that is considered to be distinct from the chemisorbed state. It has been observed that at room temperature this oxide structure does not exceed thicknesses

much greater than a single monolayer even after exposures to 1000 L of pure oxygen [86]. (1 L = 1 Langmuir = 10^{-6} Torr · s.) A survey of the literature does not reveal much information about the room-temperature oxidation rate of Mo in air, however, except under very humid conditions. At higher temperatures, in-depth oxidation of Mo surfaces will occur; this has been found to start at $\sim 200°C$, and proceeds via diffusion of the oxygen into the surface [87]. The stable oxides formed are MoO_2 and MoO_3.

Based on the above information, it is virtually certain that some sort of oxide layer was present at the target surfaces. The thickness of the layer is less easily ascertained; even if in-depth oxidation did not begin while the targets were exposed to air prior to being loaded into the vacuum chamber, it is possible that oxygen could have diffused into the target surfaces during the 300°C bakeout, although the exposure during this time would have been relatively small. In view of the sputtering yield data, it seems that the surface oxide could not have been much more than a couple of monolayers thick.

A question of fundamental importance to the interpretation of the results of these experiments is whether the target surfaces could have become enriched in the lighter isotope either through the formation of the (presumed) oxide layer or by some other mechanism that is not readily apparent; if such were the case, the observed fractionation effects could have much less to do with preferential sputtering than with some very unusual and interesting surface chemistry. Several arguments can be made against this possibility. First, as noted above, oxygen is thought to be the mobile agent in the oxidation of Mo, which suggests that the different diffusion rates for the two Mo isotopes could not cause the existing isotopic composition of a layer to change as it oxidizes because the Mo atoms would not move much with respect to each other. Even if the opposite were true and the Mo atoms were the mobile species during oxide growth, the diffusion constants D differ by only ~4% (because $D_1/D_2 \cong \sqrt{M_2/M_1}$); it seems unlikely that such a difference could account for a light-isotope enrichment nearly twice as large across a layer only a few ångströms thick. The etching and heating processes that the targets went through before

bombardment do not appear to be probable sources of isotopic segregation in the surface layers, either. The behavior of the secondary ion yield was very similar to that of the neutral sputtering yield, and yet the target used for this measurement was neither etched nor heated before bombardment. (This may also offer a clue to the true role of the oxide layer, which was presumably somewhat thicker in this instance.) Of course, the oxygen exposure would have been much higher for the SIMS target because of the O^- ion beam used for the analysis, so it may not be appropriate to make such a simple interpretation. One final observation concerns the measurements of the light-isotope enhancement as a function of ejection angle. The enrichment in normal directions was always found to be larger than (or at least approximately equal to) the enrichment at oblique angles, and the difference became more pronounced with increasing fluence; this is consistent with the idea that the target surface was becoming depleted in the light isotope with respect to the bulk composition because of preferential sputtering. It is less consistent with the idea that the target surface was initially enriched in the light isotope and was approaching a stoichiometric composition as sputtering progressed, without any preferential mechanisms operating; if this were the case, one would expect the light-isotope enrichment to be larger at oblique angles than in the normal direction initially, and for the enrichments in the two directions to be approximately equal under steady-state conditions.

While these various arguments do not prove that the observed fractionation effects were not caused by intrinsic isotopic enrichments in the target surface, they point out some of the difficulties with such an explanation. If one accepts for the moment that these arguments are correct and that the isotopic differences arose from the sputtering process itself, one must still consider the role of the modified surface layer in the phenomenon. Assuming that, as suggested above, the surface included an oxide layer several ångströms thick, two alternate possibilities exist. One is that the oxygen present in the matrix somehow mediated the collisional process in a manner that caused the preferential ejection of the light Mo isotope, and that this effect disappeared as soon as the oxygen-containing layer was removed. The other

is that the preferential ejection of the light Mo isotope was essentially unaffected by the presence of another much lighter atomic species in the surface layer, but that the depth of origin of the sputtered atoms happened to coincide with the initial thickness of the altered layer; as soon as the volume contributing to the sputtered flux became depleted in the light isotope, the effect disappeared, independent of the fact that in the same period the volume containing the impurities was removed.

This second possibility may not be so improbable as it seems at first glance. It has been observed that the vast majority of sputtered atoms originate from the outer two monolayers of a target surface [29,30], and in the absence of significant transport processes in the bulk, compositional changes induced by sputtering will remain concentrated in these outermost layers. This is consistent with the above suggestion. One may also point to other measurements in which comparable transient effects were observed for targets consisting *entirely* of oxide, such as that made by Gnaser *et al.* for TiO_2. These points are only suggestive, however; further investigation is obviously necessary to establish the true situation.

Even with this ambiguity, it is instructive to compare the results with the predictions of the various theories and computer simulations. Consider first Sigmund's model for the sputtering of isotopic mixtures [26,70,79], which is an extension of his original treatment of linear cascade sputtering [20]. To reiterate very briefly, the original theory was based on the solution of a classical Boltzmann transport equation describing the velocity distribution of the atoms participating in the collision cascade. To simplify the problem, this distribution was assumed to be isotropic on the grounds that it should be dominated by the large number of low-energy recoil atoms set into motion after several generations of randomizing collisions. Another simplifying assumption was that the sputtered surface could be treated as an imaginary plane in an infinite, random medium, and that surface-specific features such as the binding energy could be included after obtaining the infinite-medium solution. Collisions between atoms in the cascade were assumed to be binary, and were represented by a standard power-law scattering cross section. The form of this cross section is germane to the extension of the theory to include atoms of different

masses in the cascade; it is given by

$$d\sigma_{ij}(E,T) = \begin{cases} C_{ij}E^{-m}T^{-1-m}, & 0 < T \leq \gamma_{ij}E, \\ 0, & \text{otherwise}, \end{cases} \tag{4.5}$$

where $d\sigma_{ij}(E,T)$ is the differential cross section for an atom i with energy E to transfer an energy between T and $T+dT$ to a stationary atom j in a collision. C_{ij} is a constant that depends on the masses and atomic numbers of the atoms involved—the mass dependence is of the form $(M_i/M_j)^m$; m is a parameter ($0 \leq m \leq 1$) that characterizes the screened-Coulomb interaction potential between the colliding atoms, with m=1 for high-energy (Rutherford) scattering and $m \cong 0$ for low-energy (highly-screened) scattering. The maximum energy that can be transferred in a collision is $\gamma_{ij}E$ where

$$\gamma_{ij} = \frac{4M_iM_j}{(M_i + M_j)^2}. \tag{4.6}$$

To include isotope effects in the original theory, Sigmund expressed the mass of each isotopic species as

$$M_i = M + \Delta M_i, \tag{4.7}$$

where M is the mean atomic mass, so that all quantities of interest could be expanded up to first order in the mass difference ΔM, assuming that

$$\Delta M \ll M. \tag{4.8}$$

Upon carrying out this expansion, one finds that the yield ratio for two isotopes i and j is given by

$$\frac{Y_i}{Y_j} = \frac{n_i}{n_j}\left(\frac{M_j}{M_i}\right)^{2m}, \tag{4.9}$$

where n_i and n_j are the fractional abundances of the two isotopes in the medium. This can be expressed in the standard form of Equation (4.1) for the enrichment of isotope i with respect to isotope j in the sputtered flux:

$$\delta_{ij} = \left[(M_j/M_i)^{2m} - 1\right] \times 1000. \tag{4.3}$$

This prediction of a light-isotope enhancement is seen to arise from the the mass-dependence of the constant factor C_{ij} in the differential scattering cross section

shown in Equation (4.5); simply stated, lighter isotopes are more easily set in motion than heavy isotopes, and, once moving, are not as easily slowed down, resulting in a larger number of light isotopes reaching the surface and escaping. Central to the size of the effects predicted by this theory is the value of the parameter m; at the low energies characteristic of the late-generation atoms in a collision cascade, m should not be much larger than zero, presumably. A frequent choice on the basis of theoretical grounds [20,26] has been the value m_{BM}=0.055 corresponding to a Born-Mayer interaction potential.

Comparing this with the values of m presented in Table 4.2 that were calculated by substituting the extrapolated zero-fluence enrichments from these measurements into Equation (4.3), the discrepancy is quite apparent; the experimentally-determined values of m, which range from 0.3 to 0.45, are nearly an order of magnitude larger than m_{BM}. Such large values correspond to atomic collisions at energies of several hundred eV or even several keV, and do not represent physically realistic choices for the value of the parameter m in the theory. In fairness, it may not be appropriate to make a direct comparison between the results of these experiments and the theoretical prediction of Equation (4.8) because of the uncertain composition of the Mo target surfaces. Assuming that the surfaces were oxidized, Relation (4.8) would not have been satisfied because the mean atomic mass would have been reduced significantly by the presence of oxygen; thus, conditions under which the above theory is applicable would not have been met. There are two reasons for retaining the comparison, however. The first is that although the majority of sputtered atoms originate from the surface monolayers, the cascade extends much deeper into the bulk; if the surface oxide in these experiments were very thin, as it appears to have been, then Relation (4.8) would have been satisfied in most of the volume in which the kinetic processes leading to sputtering developed. The second reason is that the author of the above theory has himself compared his predictions without any sort of prefatory comment [26] to the measurements made by Russell *et al.* of Ca isotopes sputtered from CaF_2, for which Relation (4.8) is certainly not satisfied if one includes fluorine when calculating the mean atomic mass.

Before commenting further about the comparison between Sigmund's theory and the present results, the other principal theoretical treatment of isotopic effects in sputtering should be briefly reviewed. This is the 'surface flux' model of Watson *et al.* [81] and Haff *et al.* [82], which is also based on the linear cascade theory. In developing their theory, however, Watson and Haff argued that atoms in the extreme surface layer of a solid cannot participate fully in the collision cascade, as is implicitly assumed in the infinite-medium approach of linear cascade theory. To compensate for this, they treated the layer from which sputtered atoms originate as separate from the underlying bulk, and used the general solution for the flux of moving atoms in the bulk to calculate the number and type of collisions with atoms in the surface layer; the recoiling surface atoms were then considered to have been sputtered. The resulting prediction for the fractionation of isotope k with respect to isotope l in the sputtered material is given by

$$\delta_{kl} = \frac{\overline{\gamma}_k}{\overline{\gamma}_l} - 1, \tag{4.10}$$

where

$$\overline{\gamma}_k \equiv \frac{\sum_i n_i \sigma_{ik} \gamma_{ik}}{\sum_i n_i \sigma_{ik}}, \tag{4.11}$$

n_i is again the fractional abundance of species i, γ_{ik} is given by Equation (4.6), and σ_{ik} is the total collision cross section between atoms of type i and type k. (Note that although k and l in Equation (4.10) are assumed to be of the same atomic species, the sums in Equation (4.11) include all the chemical species in the target.) Hard-sphere energy-independent cross sections were assumed in the derivation, which is essentially equivalent to omitting the mass-dependent factor in Equation (4.5). Hence, this model ignores from the outset effects of the type predicted by Sigmund's treatment. (If the surface layer is treated as separate from the bulk in the latter model, the predicted isotopic enrichment depends on the mass ratio to the power m rather than $2m$ [26].) However, Equation (4.9) may be applied to complex media without any restriction on the relative mass differences of the components, so that this model does have the advantage over Sigmund's of estimating matrix effects—

i.e., those associated with the presence of atoms with masses much different from the isotopes in question.

The fractionation predicted by Equation (4.9) does not compare any more favorably with the zero-fluence enrichments estimated from these measurements than does the prediction of Equation (4.3) for realistic values of m. If one assumes that a relatively thick layer of MoO_2 was present on the target surface, Equation (4.9) predicts a light-isotope enrichment of $\sim 25‰$, which is almost a factor of three smaller than the observed values; if, on the other hand, one assumes that the modified surface layer was too thin for its atoms to participate significantly in the cascade development, the model fails to predict any enrichment at all because the Mo isotopes were equally abundant in the bulk material.

Both of the above theories predict no angular or projectile dependence in the fractionation because of the underlying assumption of an isotropic velocity distribution in the collision cascade. The fractionation data measured here, however, exhibit an angular dependence even at the lowest bombarding fluence, at least for the 5 keV Xe^+ projectiles; as pointed out earlier, the light-isotope enrichment in this instance was $\sim 20‰$larger for normally-ejected material than for obliquely-ejected material. In view of the rapid intrusion of secondary effects into both the angular and overall fractionation measurements, it is difficult to say with certainty whether this angular dependence is actually a primary sputtering effect. However, the very similar relative angular enrichments for the two lowest-fluence measurements in this case [*cf.* Figure 4.8(b)] indicate that the effect was not changing rapidly during these bombardments, and thus may have been present from the outset. A corresponding low-fluence angular dependence could not be resolved in the 5 keV Ar^+ data.

Thus, the experimental evidence suggests that there may be angular effects accompanying preferential sputtering, although these appear to depend to some extent upon the projectile. This behavior, along with the magnitude of the light-isotope enrichments observed in the sputtered flux, is in serious disagreement with the predictions of the above two theoretical treatments. The data *are* consistent, however, with other relatively low-fluence measurements, notably the secondary-ion

measurements of Gnaser *et al.* and Baumel *et al.*, and the collector measurements of Russell *et al.* (In the last instance, bombarding fluences were large enough that the primary effects were somewhat diluted and hence were not as pronounced; it is interesting to note that the angular dependence observed for the Ca isotopes sputtered from fluorite in that experiment was similar to the high-fluence angular distribution shown in Figure 4.9, where the light-isotope enrichment was actually largest in the mid-range of polar angles.) Furthermore, the observed behavior compares reasonably well with the results of computer simulations. For example, in one of their simulations of the sputtering of pseudo-Cu, Shapiro *et al.* [27,28] chose the relative mass difference between the isotopes in their target to match that of a $^{92}Mo/^{100}Mo$ target. For 5 keV Ar^+ bombardment, they found a total light-isotope enrichment in the sputtered flux of 62‰; for material sputtered within 35° of the target normal, the enrichment was 74‰(compared to 78‰in this experiment), and outside this range it was 50‰. Of course, the statistical certainty of the simulation result is relatively poor, and the extraordinarily good agreement for normal ejection between the simulation and experiment must be considered largely coincidental; even so, there is certainly qualitative agreement. The question of the angular dependence for Ar^+ is still open, although the dependence for Xe^+ is qualitatively similar.

The emerging consensus that includes all of the above elements is that primary preferential sputtering effects are are both larger and more complex than predicted by existing analytic theory. Although parts of the two theories outlined above are undoubtedly correct, such as the mass-dependent collision cross sections of Sigmund's treatment, and the importance of both the surface layer and other atoms in the sputtered matrix as dealt with by Haff and Watson, the largest single failing of both theories is probably the assumption of an isotropic velocity distribution in the collision cascade. This is strongly suggested by the results of Shapiro *et al.*, which showed a very large momentum asymmetry in the cascade, with a disproportionately large fraction of the lighter isotopes acquiring a component of momentum directed back towards the surface. The net momentum carried into the target by a projectile must necessarily be conserved, but not that of different components of cascade.

One can argue from an intuitive standpoint that light isotopes are able to turn around more efficiently in the target than heavy isotopes, because they can do so in a single collision with a heavy isotope, whereas the converse is not true. This asymmetry may couple with the proximity of the surface to give rise to the large effects observed. Another way of stating this is that the portion of the collision cascade developing near the surface does not have time to randomize fully before some of the participating atoms reach the surface and escape.

By virtue of the same sort of argument, one can understand the origin of projectile- or matrix-dependent effects. The efficiency of energy and momentum transfer in a collision as expressed by Equation (4.6) depends on the relative masses of the colliding particles; the closer the masses, the more efficient the coupling. Hence, a projectile will share more of its energy with the isotopic species having a mass closest to its own. Similarly, if the target contains a large fraction of atoms of another chemical species not of direct interest, these atoms will share the energy they acquire with the closest-matched isotope more efficiently. If a component of the collision cascade intersects the surface before its energy has been fully shared among all the participants, the sputtering yield can be affected. (The model of Watson and Haff takes into account this effect in the surface layer.) Thus, for example, the yield for a projectile lighter than the sputtered atoms should be relatively more enriched in the light isotope than the corresponding yield for a heavy projectile. It is apparent from the various experiments, including these measurements, that such effects are not as large as the above-mentioned momentum asymmetry under most conditions (although the simulations of Eckstein *et al.* showed that this effect could predominate at very low energies [83]).

The present results for Ar^+ and Xe^+ show nearly identical zero-fluence fractionations at 5 keV; at 10 keV, however, the Xe^+ yield was substantially less enriched in the light isotope than any of the other yields. This may be an indication of the type of projectile-dependent effect just outlined, but such an interpretation should be made with caution. At 10 keV, Xe^+ is on the verge of the spike regime described in §1.2 [88,89], and the smaller isotope effect may be related to this in some way.

As was pointed out in the preceding section, the light-isotope enrichments for the Xe^+ projectiles were observed to drop towards their steady-state values more slowly than those for Ar^+, which suggests that a larger volume at the target surface was contributing to the sputtered flux. This may have been due to collisional mixing or some similar transport process that did not occur to the same extent during the Ar^+ bombardments, and that may also have been associated with the denser collision cascades.

As mentioned in §4.1, preferential sputtering may have contributed to the isotopic anomalies observed in a large number of extraterrestrial samples [10]. If, for example, grains of material were sputtered by the solar wind, their surfaces would become enriched in the heavy isotopes because of the type of effects observed in these experiments. An agglomeration of such grains would then represent a material of anomalous isotopic composition. It is interesting to estimate the grain size necessary to arrive at a particular net enrichment based on the present results, although such an estimate will not have any general validity because of the target and projectile specificity. If one ignores angular effects (which will tend to underestimate the following quantity), the net excess of light-isotope atoms sputtered in taking the target from pristine condition to steady state can be estimated from the fluence- or erosion-dependence of the light-isotope enhancement measured at normal angles. For the 10 keV Ar^+ bombardment, the excess amounted to $\sim 10^{14}\,\mathrm{atoms\,cm^{-2}}$, and approximately twice that number for the 5 keV Xe^+ bombardment. If one uses the second number, the approximate grain diameter necessary to achieve a 1‰enrichment in the ^{100}Mo isotope is $\sim 0.3\,\mu$m. Thus, the size of the effect will be quite small unless the sputtered grains are also very small. Note that the efficiency of this mechanism increases if transport processes act to increase the volume at the grain's surface that contributes to the sputtered flux.

One final comment about consequences of preferential sputtering concerns spectroscopic techniques such as SIMS and SNMS that analyze material sputtered from the samples being examined. It is apparent that effects of the type observed here will always be a complication in such analyses. The primary effects can be avoided

relatively easily by sputtering long enough to reach steady-state conditions before making any measurements; the secondary effects, on the other hand, are not to be avoided. In particular, because spectrometers accept sputtered particles from a limited solid angle, usually in the direction of the sample normal, the flux of collected particles will be enriched in the light isotopes because of surface depletion of the same. Such an effect can easily exceed 10‰, and may differ with the sample material. Consequently, this represents another potential source of error in making precision isotope measurements.

4.5 Summary and Outlook

In these experiments, artificial targets of $^{92}Mo/^{100}Mo$ were sputtered with various keV ion beams, and the ejected material was examined for isotopic fractionation both as a function of bombarding fluence and as a function of emission direction. At the lowest fluences for which measurements were made ($\sim 10^{15}$ ions cm^{-2}) both the neutrals and secondary ions sputtered into the normal direction were found to be enriched in the light isotope by as much as ~70‰compared to steady state. For 5 keV Xe^+ projectiles, the light-isotope enrichment at angles far from the target normal was ~20‰less than the corresponding enrichment in the normal direction; no angular dependence could be resolved for 5 keV Ar^+ projectiles at the lowest fluence. The fractionation was observed to decrease to steady-state values after bombarding fluences of a few times 10^{16} ions cm^{-2}, with the angular dependence becoming more pronounced.

A strong correlation was found to exist between the fractionation behavior and the total sputtering yield for these bombardments, indicating that a surface layer, perhaps an oxide, was influencing the entire process. Further investigation is necessary to assure an unambiguous interpretation of the results, although arguments have been presented to suggest that preferential sputtering is the most likely explanation for the observed effects. Two experiments should be performed to establish whether this is true. First, the sticking probability of the sputtered Mo incident on the graphite collectors should be quantified as a function of coverage for both

isotopes in the same manner as described in Appendix A to verify that the measured isotopic variations are not artifacts of the collector technique used. Second, a pristine target surface should be examined to see if the extreme surface monolayers are somehow enriched in the light isotope. This represents a difficult measurement because the layer in question is only a few ångströms thick. One might be able to use ion scattering spectroscopy (ISS), although achieving the required resolution would be difficult; a second approach might be to dissolve selectively the surface layers (assuming they are oxidized) and analyze the etchant using mass spectrometry.

If these experiments produce null results, a third experiment should be carried out to determine the role of the thickness of the surface oxide layer in the observed fractionation behavior. This could be done easily by sputtering a target that had been deliberately heated in air to grow a thick oxide. It would be very interesting to see if the magnitude or fluence dependence of the light-isotope enrichment changed with the oxide thickness.

Assuming that the isotopic effects observed in these experiments *are* a consequence of preferential sputtering, the neutral data represent measurements made at fluences nearly two orders of magnitude smaller than those used in previous experiments, and allow closer comparison with theoretical predictions that apply in the limit of zero bombarding fluence. The agreement with these predictions is poor because of both the magnitude of the observed effects and the angular dependence still apparent at the lowest fluences (for the Xe^+ projectiles). The data are reasonably consistent with other low-fluence secondary-ion measurements and with molecular dynamics computer simulations, adding further support to the idea that the atoms in the collision cascades are not well described by an isotropic velocity distribution, as is assumed in the analytic theory.

Appendix A

Sticking Probability Measurement for Au on Oxidized Al

In an experiment separate from the other work described in this dissertation, a careful study was made of the average sticking probability for sputtered Au atoms incident on oxidized Al surfaces as a function of the density of deposited atoms [50]. Results from this measurement were cited in §3.3 in the discussion of corrections for collection efficiencies in the MCI investigation. The sticking measurement was made in two parts: the first determined the average sticking probability for different coverages of Au relative to the sticking probability in the limit of zero coverage, and the second determined the absolute sticking probability in this low-coverage limit, thus providing a calibration for the results of the first part.

The apparatus used for the relative sticking probability measurement was similar to that described in §2.2, with two exceptions. The collector foils (of the same type of high-purity Al foil as was used in the MCI experiments) were mounted on the *inside* of the collector cylinder, and, rather than employing semicircular vanes to isolate the collection regions, a stationary 'masking' cylinder with a semicircular slot cut at the target level to transmit the ion beam and sputtered particles was mounted so that it intervened between the target and all but a narrow strip of the collector foil. This setup was used to collect material sputtered under UHV conditions from a Au target by 200 keV Ar^+ in a series of bombardments of progressively increasing fluence. The target was initially sputtered without collecting material long enough for the yield to stabilize (*i.e.*, until a depth exceeding the range of the ions in the target had been sputtered away), and the series of bombardments was concluded with another at the initial fluence to check that the sputtering yield had remained constant throughout the experiment. This procedure was repeated twice for two different, partially overlapping fluence ranges to cover a correspondingly larger range of collected densities. The foils were then analyzed with HIRBS, where

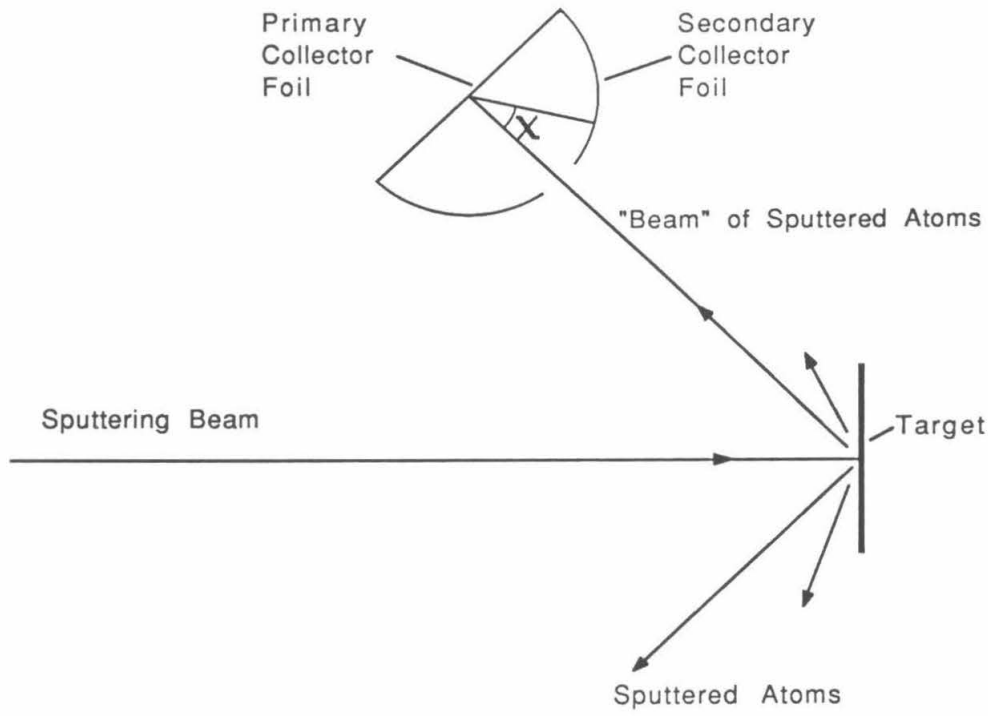

Figure A.1 Schematic of the sputtering geometry used for the absolute sticking probability measurement.

a 10 MeV $^{16}O^{2+}$ beam was used to determine the density of collected material at several fixed angles θ_j in the sputtering geometry on each collection region.

The second part of the measurement utilized the sputtering geometry depicted schematically in Figure A.1; material sputtered into a direction $\sim 45°$ from the target normal encountered a planar primary collector foil, and material that did not stick to this surface was captured by a hemispherical secondary collector foil. These foils were also analyzed using HIRBS—to determine the total number N_1 of Au atoms in the circular collection region on the primary foil, and to determine the density of collected material as a function of the angle χ on the secondary collector. The angular distribution obtained from the secondary collector is shown in Figure A.2, along with a fitted function of the form $A\cos\chi$; this distribution was integrated over the full hemisphere above the primary collector to obtain the total number N_2 of atoms that did not stick to the primary.

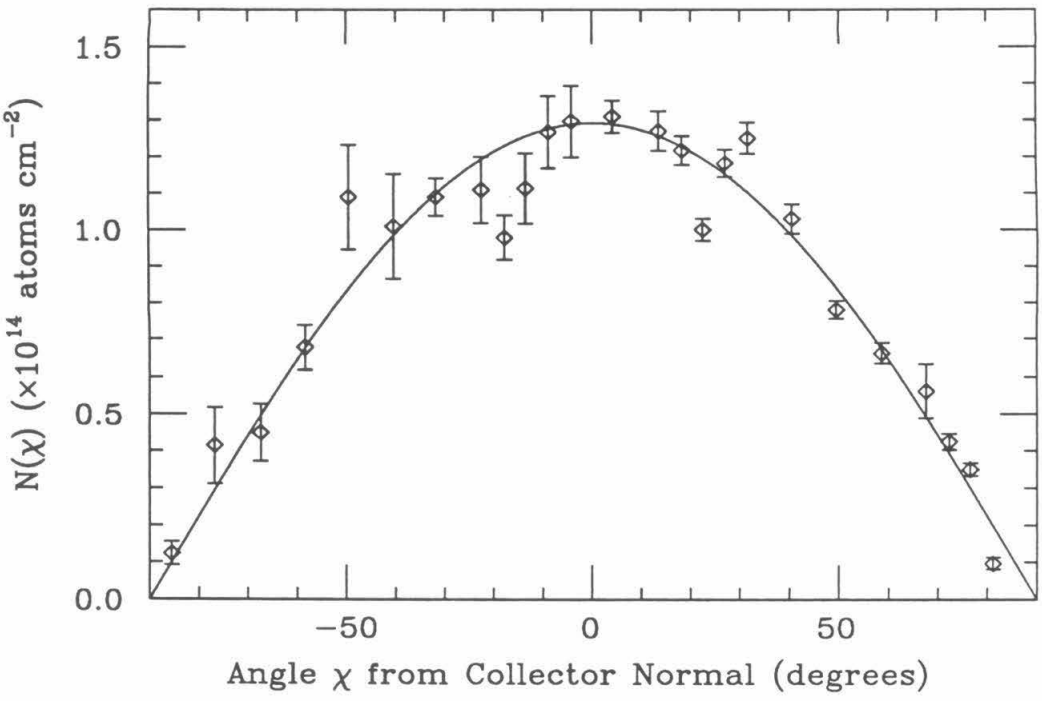

Figure A.2 Angular distribution of Au measured on the secondary collector foil. The solid line is a fitted function of the form $A\cos\chi$.

The densities of collected material determined from the first part of the measurement and the numbers of atoms N_1 and N_2 determined from the second part were then used to calculate average sticking probabilities. To describe how this was done, it is useful first to define $p(n')$ as the sticking probability for Au atoms incident on a collector surface already covered with n' Au atoms cm^{-2}. The average sticking probability $k(n)$ for n atoms cm^{-2} on the foil is then given by

$$k(n) = \left[\frac{1}{n}\int_0^n \frac{dn'}{p(n')}\right]^{-1}. \qquad (A.1)$$

This is both the experimentally accessible quantity and the useful quantity for calibrating collector-type sputtering measurements; it is simply the ratio of n, the number of atoms cm^{-2} remaining on the foil, to the total number incident up to that point. The number of Au atoms sputtered into each of the angles θ_j in the sputtering geometry was (presumably) directly proportional to the number of incident projectiles or accumulated charge Q_i for the corresponding bombardment; thus, the ratio of the average sticking probability $k(n_i(\theta_j))$ at angle θ_j for the ith

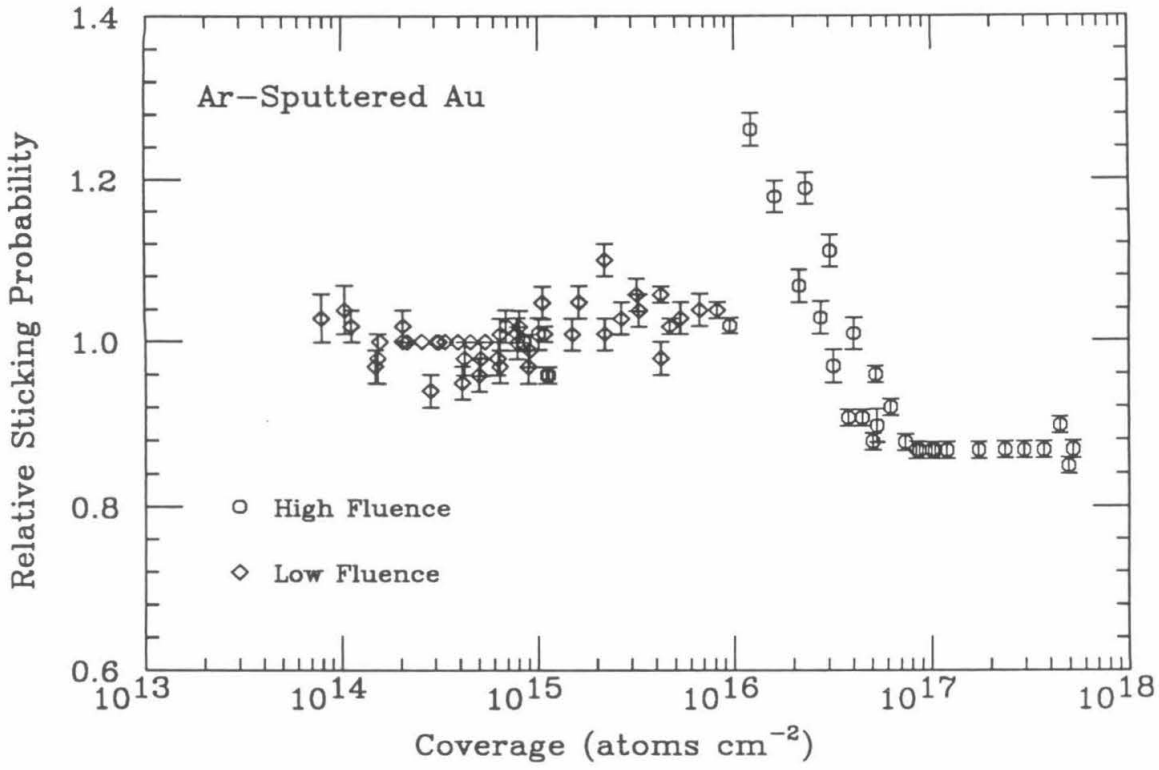

Figure A.3 Average relative sticking probability for Ar-sputtered Au incident on oxidized Al, plotted as a function of Au coverage on the surface. The points without error bars were from the lowest-fluence bombardment and were used to establish the normalization.

bombardment to the average probability $k(n_1(\theta_j))$ at the corresponding angle for the lowest-fluence bombardment is given by

$$\frac{k(n_i(\theta_j))}{k(n_1(\theta_j))} = \frac{n_i(\theta_j)}{n_1(\theta_j)} \cdot \frac{Q_1}{Q_i}. \qquad (A.2)$$

If one assumes that the sticking probability $p(n(\theta_j))$ was constant and equal to $p(0)$ for the coverages (which were all much less than a monolayer) at all angles in the lowest-fluence bombardment, then $k(n_1(\theta_j)) = k(0) = p(0)$, and Equation (A.2) represents the average sticking probability relative to the zero-coverage sticking probability. The ratios calculated from this equation are presented in Figure A.3 as a function of surface coverage.

To calculate the absolute sticking probability in the zero-coverage limit from the results of the second part of the measurement, it was necessary to determine one

other quantity from the relative sticking data, namely, the ratio R between $k(0)$ and the average sticking probability at very high coverages, $k(n > 10^{17}\ \text{atoms}\,\text{cm}^{-2})$. At very high coverages, $p(n)$ is expected to be constant because it represents the probability of Au sticking to a Au surface; Equation (A.1) shows that, because of this, $k(n)$ also approaches a constant value at very large coverages, and, consequently, so will R. This constant R could be estimated from Equation (A.2) by using the largest measured densities n, which approached 100 monolayers coverage; the value obtained was $R = 1.15 \pm 0.10$. Because the density of collected material on the primary collector used in the second part of the measurement was very high, the average sticking probability here could be characterized by $k(n > 10^{17}\ \text{atoms}\,\text{cm}^{-2})$; conversely, the coverages on the secondary collector were very low and could be characterized by $k(0)$. Thus, assuming that all (or approximately all) of the material that did not stick to the primary collector on first impact *did* stick to the secondary collector, the resulting conservation equation can be solved for the absolute sticking probability in the limit of zero coverage:

$$k(0) = R - \frac{N_2}{N_1}, \qquad A.3$$

where N_1 and N_2 are the total numbers of atoms on the primary and secondary collectors, respectively, as determined above. The value of $k(0)$ obtained was $0.92^{+0.08}_{-0.10}$. The corresponding value for $k(n > 10^{17}\ \text{atoms}\,\text{cm}^{-2})$ is 0.80 ± 0.03.

The accuracy of the above assumption about atoms sticking after no more than one "bounce" is supported by the very low background of Au measured on the primary foil away from the collection region. It is possible that material not sticking to the primary foil initially could have scattered from other surfaces in the apparatus before reaching the secondary collector, so that the measured value of N_2 is too large and the corresponding value for $k(0)$ is only a lower limit; however, $k(n)$ (which cannot exceed unity) was observed to have a maximum value of 1.08 ± 0.09 at $n \approx 10^{16}\ \text{atoms}\,\text{cm}^{-2}$, so that it seems very unlikely that the value of $k(0)$ is too small.

Two other sticking probability measurements of a similar nature were made for

Au sputtered by 200 keV Xe^+, and for Ag sputtered by 200 keV Ar^+. The results for Xe-sputtered Au were similar to those just described for Ar-sputtered Au, with $k(0) = 0.098^{+0.02}_{-0.10}$ and $k(n > 10^{17}\,\text{atoms}\,\text{cm}^{-2}) = 0.89 \pm 0.03$; for Ag, however, values (lower limits in this case) of $k(0) = 0.46 \pm 0.20$ and $k(n > 10^{17}\,\text{atoms}\,\text{cm}^{-2}) = 0.80 \pm 0.20$ were measured. In all three cases, the sticking probability changed significantly in the range of coverages between one and twenty monolayers.

These measurements were not really designed to allow one to point to specific mechanisms responsible for the sticking of the sputtered atoms on the collectors. The surfaces were not well-characterized, but this is quite typical of collector measurements in general; also, the results are averaged over the entire spectrum of incident energies of the sputtered particles. As mentioned in §2.5, the reasons for the sticking probability being less than unity are not well understood, particularly for heavy particles incident on a light substrate. Even for atoms incident on a substrate of the same material, computer simulations [90] suggest that direct reflection of the incident particles does not contribute substantially to the fraction of non-sticking atoms. Libbrecht *et al.* measured the energy dependence of the sticking probability for sputtered ^{235}U atoms on Al collectors, and found this probability to drop from unity for energies $\gtrsim$10 eV to $\sim$ 0.9 for lower energies [91]; this could indicate either a direct energy-dependence for single atoms, or perhaps a species-dependence since different species, *e.g.*, single atoms or clusters of atoms, will have different energy distributions. It is possible that the reduced sticking probabilities result from processes such as evaporation or resputtering by other incident atoms or ions reflected from the target surface. This last possibility was also investigated by Libbrecht *et al.*, and was found not to be a contributing factor for ^{235}U on Al, although it may not be appropriate to extend this conclusion to all systems in general.

In spite of the uncertainty surrounding the physical mechanisms underlying the sticking process, the experimental evidence indicates that the sticking probability is a measurable and reproducible quantity, and can consequently be compensated for in collector-type experiments such as those discussed in this dissertation.

Appendix B

Heavy-Ion Rutherford Backscattering Spectroscopy

In the HIRBS analysis of the collector foils in these experiments, a well-characterized beam of energetic particles was used to bombard the foils at different spots corresponding to different angles in the sputtering geometry, and both the number and energies of the projectiles scattered elastically by atoms at each spot were measured. In measurements such as this, the energy of each scattered projectile provides information about the mass of the target atom with which it collided, convolved with information about the depth of the atom beneath the foil's surface; and the number of scattered projectiles can be used to calculate the density of the corresponding scattering centers on the collector. The analysis was particularly straightforward in these measurements for two reasons: the species of interest were on the surfaces of the foils, so that the projectiles suffered no inelastic energy loss due to electronic stopping on the way into and out of the samples; also, the species of interest were (purposely) heavier than the substrate so that projectiles were scattered more energetically from the former, causing these projectiles to appear in an isolated peak well separated from the substrate signal (see, *e.g.*, Figure 3.5).

In the absence of inelastic energy losses, the relationship between the measured energy E of a backscattered projectile and its initial energy E_0 is determined simply by the kinematical scattering factor:

$$E = E_0 \left[\frac{x\cos\theta + \sqrt{1 - x^2\sin^2\theta}}{1 + x} \right]^2 , \qquad (B.1)$$

where E_0 is the energy of the incident projectile, E its energy after scattering, and θ the angle through which it was deflected, all measured in the laboratory reference frame; $x \equiv M_1/M_2$, where M_1 is the projectile mass and M_2 is the mass of the target atom. The differential scattering cross section at the energies in question is that for two bare nuclei and is given by the Rutherford formula, which in the

laboratory reference frame is

$$\frac{d\sigma}{d\Omega}(\theta) = \left(\frac{Z_1 Z_2 e^2}{2E_0}\right)^2 \frac{\left[\cos\theta + \sqrt{1 - x^2\sin^2\theta}\right]^2}{\sin^4\theta\sqrt{1 - x^2\sin^2\theta}}, \qquad (B.2)$$

where Z_1 and Z_2 are the atomic numbers of the projectile and target atoms, respectively, and e is the magnitude of the electronic charge. This quantity determines the intensity of the backscattered flux; it is immediately apparent that projectiles with a large atomic number and relatively low energy will offer the greatest sensitivity in a measurement. The differential cross section in Equation (B.2) is valid only for a limited range of projectile energies: if the projectile energy is too large, the nuclei will approach closely enough for nuclear resonances to alter the cross section for particular projectile-target combinations; if the projectile energy is small enough that the distance of closest approach is comparable to or larger than the radii of the inner electronic orbitals, the interaction will be screened and the cross section will be reduced from the Rutherford value. Actually, electronic screening can be important even for small distances of closest approach because it reduces the distance over which the interaction potential would otherwise act. The following factor can be included in the differential cross section to correct for moderate screening [92]:

$$\gamma = 1 - 0.049 Z_1 Z_2^{4/3}(1 + x)E_0^{-1}. \qquad (B.3)$$

The absolute densities n of sputtered atoms on the collector surfaces were determined (except for the collectors from the isotope experiment, where the Mo extended beneath the surface and a more sophisticated approach was taken) from the equation

$$n = \frac{S}{d\sigma} \cdot \frac{q}{Q}, \qquad (B.4)$$

where S is the number of counts in the backscattering spectrum corresponding to the species of interest, q is the charge carried by each incident ion, Q is the total charge collected on the target during the measurement, and $d\sigma$ is the convolution of the differential scattering cross section with the solid angle subtended by the particle detector. The solid angle was defined by the collimator between the target

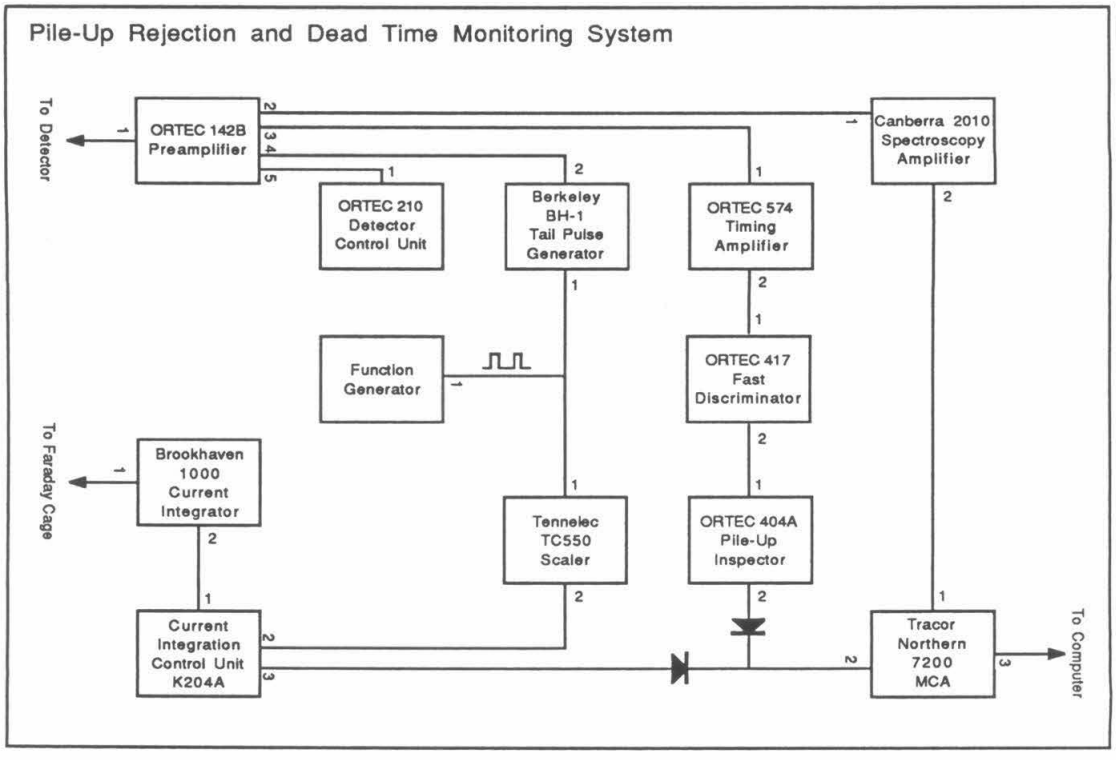

Figure B.1 Schematic of the detection electronics for the HIRBS apparatus.

and the detector, which is shown in the inset of Figure 3.4; the dimensions of this collimator were measured with an optical comparator, and the distance from the target to the collimator in the backscattering setup was also carefully measured; the solid angle subtended was ~50 millisteradians. The above convolution for the annular collimator is given by

$$d\sigma = 2\int_{r_1}^{r_2} \gamma \frac{d\sigma}{d\Omega}(\pi - \mathrm{atan}\frac{r}{D}) \cdot \frac{rD}{(r^2+D^2)^{3/2}} \cdot \left\{ \phi_0 + 2\mathrm{atan}\sqrt{\left[\frac{r(r_1+r_2)}{r^2+r_1r_2}\right]^2 - 1} \right\} dr, \tag{B.5}$$

where D is the target-collimator distance, $r_1(= 0.2771 \pm 0.0007\,\mathrm{cm})$ and $r_2(= 0.4481 \pm 0.0004\,\mathrm{cm})$ are the inner and outer radii of the collimator opening, respectively, and $\phi_0(= 135° \pm 0.5°)$ is the angle subtended by each arc of the opening.

An annular Si surface barrier detector was used to count the backscattered particles; this detector was connected to standard electronics, including a preampli-

fier, spectroscopy amplifier, and multichannel analyzer (MCA). The setup is shown schematically in Figure B.1. The system is somewhat more sophisticated than was necessary for most of the measurements, during which the count rate was low and dead time was not a problem. For several of the foils from the CsI bombardments and the Au sticking probability measurement (*cf.* Appendix A), however, count rates were quite high and compensation for dead time became important. To accomplish this, a function generator was used to trigger both a scaler and a tail pulse generator at ~50 Hz; the tail pulses were added to the pulse stream from the detector so that they appeared as counts in a peak in the MCA spectrum and were subject to the same dead-time losses as the rest of the pulses. At the end of a measurement, the data were multiplied by the ratio of the number of counts S_s registered by the scaler to the number of counts S_P in the corresponding spectrum peak. [See Ref. 93 for a detailed discussion.] Facility for pile-up rejection was also incorporated into the system. [For a general discussion of backscattering spectroscopy, see Ref. 94.]

Appendix C

Factors Influencing the Angular Sputtering Yield

For the sputtering apparatus used in the MCI investigation in particular, a number of different misalignments in the collection geometry were possible; the effects of these asymmetries on the measured angular distributions of sputtered material are apparent in Figure 3.6. As mentioned in Chapter 3, the misalignments were compensated for in the model used to fit the distributions. Figure C.1 illustrates the various possible offsets in the plane of the collection region. The collector can be translated with respect to the sputtered point on the target and rotated slightly with respect to the beam axis. By designating offsets perpendicular to the target face by rF (where r is the collector radius), offsets parallel to the target face by rC, and rotations with respect to the beam axis by D, one can relate the measured distribution to the anticipated form of the differential angular sputtering yield. Thus, assuming that the actual sputtering yield is of the form

$$Y(\theta') = A\cos^B\theta', \tag{C.1}$$

where θ' is the true polar angle with respect to the target normal, the corresponding density distribution of sputtered material on the foil measured as a function of θ (the angle from the bisector of the collection region) will be given by

$$n(\theta) = \frac{AN_0}{r^2} \cdot \frac{[\cos(\theta - D) - F]^B}{\xi^{B+2}}, \tag{C.2}$$

where N_0 is the number of incident projectiles and

$$\xi = \sqrt{1 + C^2 + F^2 - 2\,[C\sin(\theta - D) + F\cos(\theta - D)]}. \tag{C.3}$$

Equation (C.2) was fitted to the measured distributions of sputtered material in the MCI investigation to determine values for the free parameters A and B. Estimates could be inserted for the parameters C, D, and F, or, alternatively, C and D could

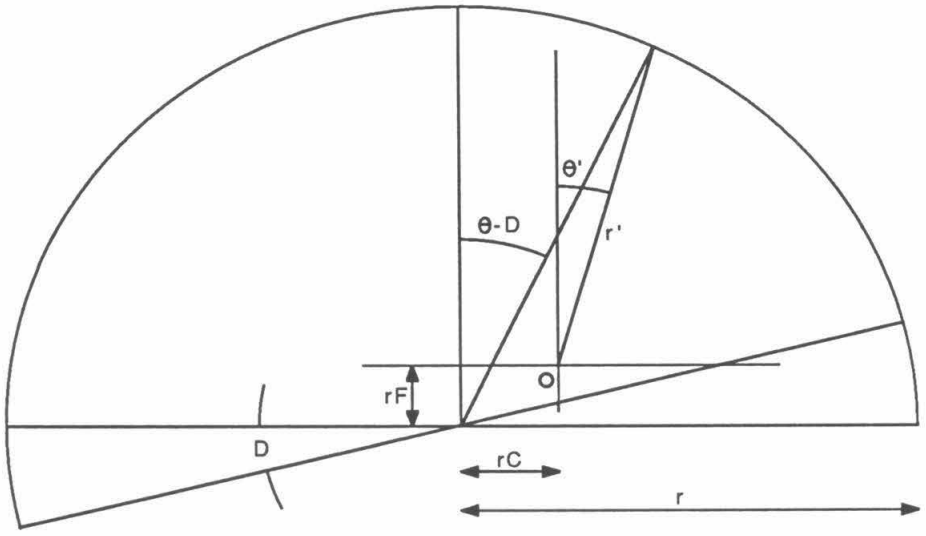

Figure C.1 Illustration of possible offsets in the sputtering geometry. The point **O** represents the location of the target, and the ion beam is assumed to be incident along the vertical line through this point. The semicircle represents the collector, which may be offset both parallel and perpendicular to the target face, and rotated with respect to the beam axis.

be treated as free parameters in the fit. When this second approach was taken, D was found to be quite close to zero in all cases, and the values of C for collection regions on the same foil were very similar.

The above treatment assumes that the sputtered atoms originate from a single point on the target's surface, but this was clearly not true for the experiments. To investigate the effect of the size of the bombarded spot relative to the collector radius on the resulting shape of the angular distribution, the following numerical test was made. Each point in a circular region of radius $0.182r$ on the target (corresponding to the relative size of the beam spot to the collector radius in the isotope experiments) was assumed to exhibit a simple $\cos\theta'$ angular yield, and the corresponding distribution on the collector was calculated as a function of θ by integrating over the contributions from the entire circular area. The results are shown in Figure C.2, where the calculated distribution is plotted along with $\cos\theta$. The influence of the finite spot was actually quite small, causing the distribution

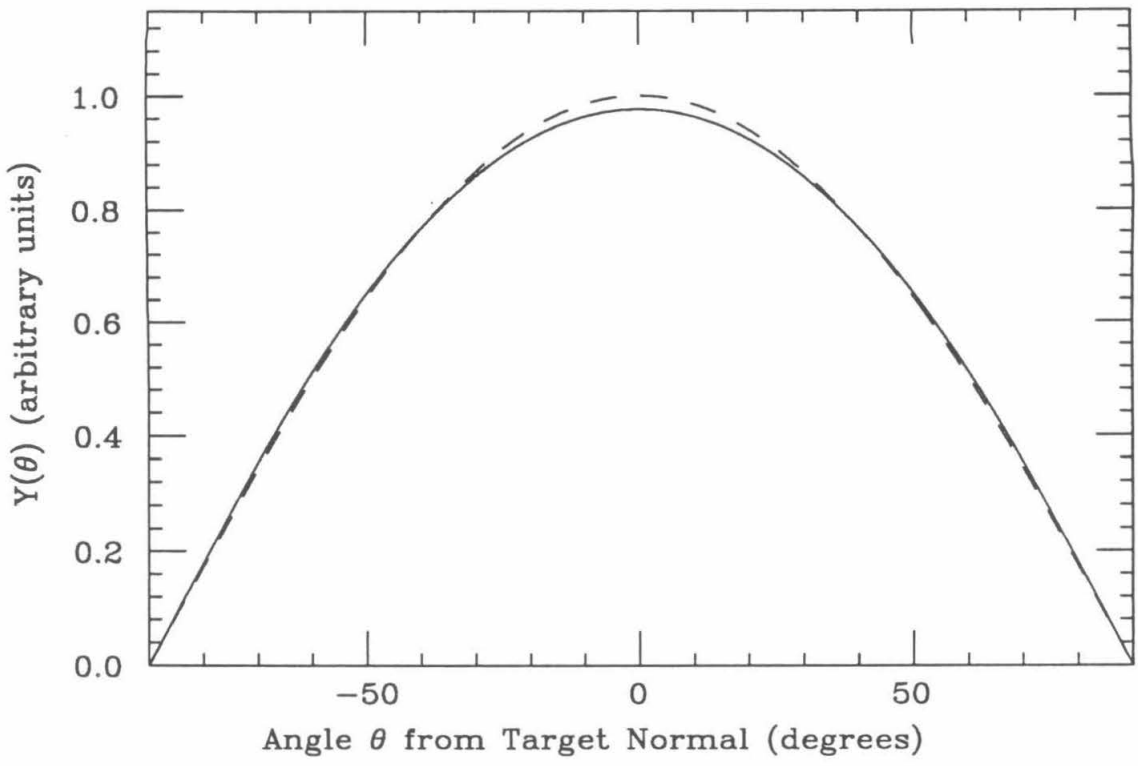

Figure C.2 Illustration of the effect of a finite beam spot on the shape of the measured angular distribution of sputtered material. The dashed line is $\cos\theta$, the form assumed for the "true" sputtering yield in this calculation, and the solid curve is the resulting distribution of material on the collector arising from a circular region with a radius 0.182 times that of the collector.

to broaden only slightly; when the resulting distribution was fit in the standard manner, a value of $B = 0.975$ was found, and the total calculated yield differed from the actual yield by $\sim 2‰$. Thus, the finite beam spots used for these measurements will have had relatively little influence on the shapes of the measured distributions or the total yields calculated from them.

Aside from the above geometrical considerations, another factor that can affect the shape of the angular distribution of sputtered material is bombardment-induced modification of the target's surface structure at high fluences. Effects of this nature were seen in both the Au target used in the MCI investigation, and in the Mo targets in the isotope study. One of two different mechanisms may be responsible for this behavior. If a surface does not sputter uniformly, it will eventually develop

topography even if it was initially quite smooth; as such surface roughness develops, the effective angle of incidence Θ changes for different faces, and the corresponding angular sputtering yields from these faces will change both in magnitude and direction with respect to the macroscopic surface normal. (As a general rule, the angular distribution will be cosine-like with respect to the local surface normal, and will increase in magnitude in proportion to $1/\cos\Theta$ except for angles of incidence close to 90°.) Eventually, material sputtered from one face can be trapped on other surrounding faces rather than escaping; such shadowing effects may give rise to macroscopic angular distributions significantly different from a power of $\cos\theta$ [49]. The second mechanism involves bombardment-induced texturing of the target surface—*i.e.*, preferential orientation of crystallites in the material, usually with open directions perpendicular to the surface. If this occurs, preferential ejection along close-packed directions in the crystallites can lead to altered angular distributions of sputtered material [32]. Which of these mechanisms may account for the behavior observed in this work is not readily discernable. It is unusual that the pronounced effects observed for the Mo targets appeared at such low bombarding fluences (a few times 10^{16} ions cm^{-2}), since behavior of this nature does not usually appear until after doses an order of magnitude larger. One possible explanation might be that the foils were textured before bombardment from the manufacturing process.

References

[1] W. R. Grove, Philos. Mag. **5** (1853) 203.

[2] *Proceedings, 3rd Symposium on the Deposition of Thin Films by Sputtering* (Bendix Corp., Rochester, NY, 1969).

[3] H. L. Garvin, E. Garmire, S. Somekh, H. Stoll and A. Yariv, Appl. Optics **12** (1973) 455.

[4] B. D. Power, *High Vacuum Pumping Equipment* (Reinhold, New York, 1966).

[5] R. Middleton and C. T. Adams, Nucl. Instr. Meth. **118** (1974) 329.

[6] L. C. Feldman and J. W. Mayer, *Fundamentals of Surface and Thin Film Analysis* (North-Holland, New York, 1986).

[7] T. A. Tombrello, Rad. Effects **65** (1982) 389.

[8] P. K. Haff and A. Eviatar, Icarus **66** (1986) 258.

[9] T. M. Esat, Geochim. Cosmochim. Acta **52** (1988) 1409.

[10] F. Begemann, Rep. Prog. Phys. **43** (1980) 1309.

[11] P. K. Haff, Appl. Phys. Lett. **29** (1976) 473.

[12] R. E. Scott, Thesis, Massachusetts Inst. Technol., Dept. Nucl. Eng. (1986) unpublished.

[13] J. Lindhard, V. Nielson and M. Scharff, K. Dan. Vidensk. Selsk. Mat. Fys. Medd. **36** (1968) No. 10.

[14] J. Lindhard, M. Scharff and H. E. Schiøtt, K. Dan. Vidensk. Selsk. Mat. Fys. Medd. **33** (1963) No. 14.

[15] F. Bloch, Z. Phys. **81** (1933) 363.

[16] N. Matsunami, Y. Yamamura, Y. Itikawa, N. Itoh, Y. Kazumata, S. Miyagawa, K. Morita, R. Shimuzu and H. Tawara, At. Data Nucl. Tables **31** (1984) 1.

[17] L. E. Seiberling, C. K. Meins, B. H. Cooper, J. E. Griffith, M. H. Mendenhall and T. A. Tombrello, Nucl. Instr. Meth. **198** (1982) 17.

[18] Y. Qiu, J. E. Griffith and T. A. Tombrello, Rad. Effects **64** (1982) 111.

[19] R. E. Johnson and R. Evatt, Rad. Effects **52** (1980) 187.

[20] P. Sigmund, Phys. Rev. **184** (1969) 383.

[21] J. P. Biersack, Nucl. Instr. Meth. B**27** (1987) 21.

[22] M. M. Jakas and D. E. Harrison Jr., Nucl. Instr. Meth. B**14** (1986) 535.

[23] R. L. Fleischer, P. B. Price and R. M. Walker, J. Appl. Phys. **36** (1965) 3645.

[24] Ph. Avouris, F. Bozso and R. E. Walkup, Nucl. Instr. Meth. B**27** (1987) 136.

[25] P. D. Townsend and F. Lama in *Desorption Induced by Electronic Transitions*, DIET I, N. H. Tolk, M. M. Traum, J. C. Tully and T. E. Madey, eds., Springer Ser. Chem. Phys., Vol. 24 (Springer, Berlin, Heidelberg, New York, 1983), p. 220.

[26] P. Sigmund, Nucl. Instr. Meth. B**18** (1987) 375.

[27] M. H. Shapire, P. K. Haff, T. A. Tombrello and D. E. Harrison Jr., Nucl. Instr. Meth. B**12** (1985) 137.

[28] M. H. Shapiro, T. A. Tombrello and D. E. Harrison Jr., Nucl. Instr. Meth. B**30** (1988) 152.

[29] M. F. Dumke, T. A. Tombrello, R. A. Weller, R. M. Housley and E. H. Cirlin, Surface Sci. **124** (1983) 307.

[30] K. M. Hubbard, R. A. Weller, D. L. Weathers and T. A. Tombrello, to be published in Nucl. Instr. Meth. B.

[31] P. Sigmund in *Sputtering by Particle Bombardment* I, R. Behrisch, ed., Topics Appl. Phys., Vol. 47 (Springer, Berlin, Heidelberg, New York, 1981), p. 9.

[32] M. Szymonski, W. Huang and J. Onsgaard, Nucl. Instr. Meth. B**14** (1986) 263.

[33] W. Espe, *Materials of High Vacuum Technology*, Vol. 1 (Pergamon, New York, 1966).

[34] P. A. Redhead, J. P. Hobson and E. V. Kornelsen, *The Physical Basis of Ultrahigh Vacuum* (Chapman and Hall, London, 1968).

[35] T. L. Hill, *An Introduction to Statistical Thermodynamics* (Addison-Wesley, Reading, MA, 1960), pp. 124-130.

[36] J. P. Biersack and E. Santner, Nucl. Instr. Meth. **132** (1976) 229.

[37] C. K. Meins, J. E. Griffith, Y. Qiu, M. H. Mendenhall, L. E. Seiberling and T. A. Tombrello, Rad. Effects **71** (1983) 13.

[38] B. H. Cooper and T. A. Tombrello, Rad. Effects **80** (1984) 203.

[39] R. L. Fleischer, P. B. Price and R. M. Walker, J. Appl. Phys. **36** (1965) 3645.

[40] T. Y. Arifov, D. D. Gruich and S. N. Morozov, Proc. 5th All-Union Conf. on the Interaction of Atomic Particles with Solids, Minsk (1978) Vol. 1, p. 200.

[41] R. K. Fitch and E. A. Mahmoud, Thin Solid Films **87** (1982) 379.

[42] A. Brown, J. A. van den Berg and J. C. Vickerman, Spectrochimica Acta **40**B (1985) 871.

[43] Sh. S. Radzhabov and R. R. Rakhimov, Izv. Akad. Nauk SSSR, Ser. Fiz. **49** (1985) 1812.

[44] A. J. Eccles, J. A. van den Berg, A. Brown and J. C. Vickerman, Appl. Phys. Lett. **49** (1986) 188.

[45] S. T. de Zwart, T. Fried, D. O. Boerma, R. Hoekstra, A. G. Drentje and A. L. Boers, Surf. Sci. **177** (1986) L939 .

[46] S. Della-Negra, J. Depauw, H. Joret, Y. Le Beyec and E. A. Schweikert, Phys. Rev. Lett. **60** (1988) 948.

[47] I. S. Bitenskii, M. N. Murakhmetov and E. S. Parilis, Sov. Phys. Tech. Phys. **24** (1979) 618.

[48] G. Götz, in *Ion Beam Modification of Insulators*, P. Mazzoldi and G. W. Arnold, eds. (Elsevier, New York, 1987), p. 412.

[49] K. Rödelsperger and A. Scharmann, Nucl. Instr. Meth. **132** (1976) 355.

[50] M. R. Weller, K. M. Hubbard, R. A. Weller, D. L. Weathers and T. A. Tombrello, to be published in Nucl. Instr. Meth. B.

[51] M. R. Weller and T. A. Tombrello, Rad. Effects **49** (1980) 239.

[52] P. Varga, Appl. Phys. A**44** (1987) 31.

[53] J. P. Biersack, in *Ion Beam Modification of Insulators*, ed. by P. Mazzoldi and G. W. Arnold (Elsevier, New York, 1987), p. 648.

[54] M. H. Prior, J. Opt. Soc. Am. B**4** (1987) 144.

[55] R. Kelly, Surf. Sci. **90** (1979) 280.

[56] E. Schreck and K. Dransfeld, Appl. Phys. A**44** (1987) 265.

[57] W. A. Russell, D. A. Papanastassiou, T. A. Tombrello and S. Epstein, Proc. Lunar Sci. Conf. 8th (1977) 3791.

[58] P. K. Haff, Z. E. Switkowski, D. S. Burnett and T. A. Tombrello, Proc. Lunar Sci. Conf. 8th (1977) 3807.

[59] Z. E. Switkowski, P. K. Haff, T. A. Tombrello and D. S. Burnett, J. Geophys. Res. **82** (1977) 3797.

[60] W. A. Russell, D. A. Papanastassiou and T. A. Tombrello, Geochim. Cosmochim. Acta **42** (1978) 1075.

[61] P. K. Haff, C. C. Watson and T. A. Tombrello, Proc. Lunar Planet. Sci. Conf. 10th (1979) 1685.

[62] P. K. Haff and C. C. Watson, J. Geophys. Res. **84** (1979) 8436.

[63] C. L. Melcher, D. J. LePoire, B. H. Cooper and T. A. Tombrello, Geophys. Res. Lett. **9** (1982) 1151.

[64] D. D. Clayton, Astrophys. J. **251** (1981) 374.

[65] N. Shimizu and S. R. Hart, J. Appl. Phys. **53** (1982) 1303.

[66] H. Gnaser and I. D. Hutcheon, Phys. Rev. B**35** (1987) 877.

[67] S. A. Schwarz, J. Vac. Sci. Technol. A**5** (1987) 308.

[68] H. Gnaser and I. D. Hutcheon, Phys. Rev. B**38** (1988) 11112.

[69] G. K. Wehner, Appl. Phys. Lett. **15** (1977) 185.

[70] P. Sigmund, J. Vac. Sci. Technol. **17** (1980) 396.

[71] J. M. Fluit, L. Friedman, A. J. H. Boerboom and J. Kistemaker, J. Chem. Phys. **35** (1961) 1143.

[72] W. A. Russell, D. A. Papanastassiou and T. A. Tombrello, Rad. Effects **52** (1980) 41.

[73] R. R. Olson, M. E. King and G. K. Wehner, J. Appl. Phys. **50** (1979) 3677.

[74] Z. Wang, F. Zhu, W. Chen, H. Zhang and A. Zhang, [Chinese] Nucl. Tech. **11** (1986) No. 2.

[75] O. Arai, Y. Tazawa, T. Shimamura and K. Kobayashi, Jpn. J. Appl. Phys. **18** (1979) 1231.

[76] J. Okano, T. Ochiai and H. Nishimura, Appl. Surface Sci. **22/23** (1985) 72.

[77] H. Gnaser and I. D. Hutcheon, Surface Sci. **195** (1988) 499.

[78] L. M. Baumel, M. R. Weller, R. A. Weller and T. A. Tombrello, Nucl. Instr. Meth. B**34** (1988) 427.

[79] N. Anderson and P. Sigmund, K. Dan. Vidensk. Selsk. Mat. Fys. Medd. **39** (1974) No. 3.

[80] P. K. Haff, Appl. Phys. Lett. **31** (1977) 259.

[81] C. C. Watson and P. K. Haff, J. Appl. Phys. **51** (1980) 691.

[82] P. K. Haff, C. C. Watson and T. A. Tombrello, J. Geophys. Res. **86** (1981) 9553.

[83] W. Eckstein and J. P. Biersack, Appl. Phys. A**37** (1985) 95.

[84] J. Ehrenberg and P. Børgesen, Nucl. Instr. Meth. B**15** (1986) 386.

[85] J. C. Huneke, J. T. Armstrong and G. J. Wasserberg, Geochim. Cosmochim. Acta **47** (1983) 1635.

[86] A. Benninghoven, O. Ganschow and L. Wiedmann, J. Vac. Sci. Technol. **15** (1978) 506.

[87] E. Best and I. Hinz, *Molybdenum*, Suppl. Vol. A3 of *Gmelin Handbook of Inorganic Chemistry*, 8th ed., P. F. Linde, J. F. Rounsaville, R. C. Sangster and K. Swars, eds. (Springer, Berlin, Heidelberg, New York, 1983), No. 53, p. 34.

[88] H. H. Anderson and H. L. Bay, J. Appl. Phys. **46** (1975) 2416.

[89] A. R. Oliva-Florio, E. V. Alonso, R. A. Baragiola, J. Ferron and M. M. Jakas, Rad. Effects Lett. **50** (1979) 3.

[90] M. H. Shapiro and T. A. Tombrello, Nucl. Instr. Meth. **B18** (1987) 355.

[91] K. G. Libbrecht, J. E. Griffith, R. A. Weller and T. A. Tombrello, Rad. Effects **49** (1980) 195.

[92] J. l'Ecuyer, J. A. Davies and N. Matsunami, Rad. Effects **47** (1980) 229.

[93] E. J. Cohen, Nucl. Instr. Meth. **121** (1974) 25.

[94] W. K. Chu, J. W. Mayer and M. A. Nicolet, *Backscattering Spectrometry* (Academic Press, New York, 1978).